ANTENNA ANALYSIS/DESIGN AND PROPAGATION CHANNEL MODELING FOR MIMO WIRELESS COMMUNICATION SYSTEMS

A THESIS

SUBMITTED TO THE DEPARTMENT OF ELECTRICAL AND

ELECTRONICS ENGINEERING

AND THE INSTITUTE OF ENGINEERING AND SCIENCES

OF BILKENT UNIVERSITY

IN PARTIAL FULFILLMENT OF THE REQUIREMENTS

FOR THE DEGREE OF

DOCTOR OF PHILOSOPHY

By

Celal Alp Tunç

February 2009

I certify that I have read this thesis and that in my opinion it is fully adequate, in scope and in quality, as a thesis for the degree of Doctor of Philosophy.

Prof. Dr. Ayhan Altıntaş (Supervisor)

I certify that I have read this thesis and that in my opinion it is fully adequate, in scope and in quality, as a thesis for the degree of Doctor of Philosophy.

Prof. Dr. Hayrettin Köymen

I certify that I have read this thesis and that in my opinion it is fully adequate, in scope and in quality, as a thesis for the degree of Doctor of Philosophy.

Assoc. Prof. Dr. Özlem Aydın Çivi

I certify that I have read this thesis and that in my opinion it is fully adequate, in scope and in quality, as a thesis for the degree of Doctor of Philosophy.

Assist. Prof. Dr. Defne Aktaş

I certify that I have read this thesis and that in my opinion it is fully adequate, in scope and in quality, as a thesis for the degree of Doctor of Philosophy.

Assist. Prof. Dr. İbrahim Körpeoğlu

Approved for the Institute of Engineering and Sciences:

Prof. Dr. Mehmet Baray
Director of Institute of Engineering and Sciences

ABSTRACT

ANTENNA ANALYSIS/DESIGN AND PROPAGATION CHANNEL MODELING FOR MIMO WIRELESS COMMUNICATION SYSTEMS

Celal Alp Tunç
Ph.D. in Electrical and Electronics Engineering
Supervisor: Prof. Dr. Ayhan Altıntaş
February 2009

Multiple-input-multiple-output (MIMO) wireless communication systems have been attracting huge interest, since a boost in the data rate was shown to be possible, using multiple antennas both at the transmitter and receiver. It is obvious that the electromagnetic effects of the multiple antennas have to be included in the wireless channel for an accurate system design, though they are often neglected by the early studies.

In this thesis, the MIMO channel is investigated from an electromagnetics point of view. A full-wave channel model based on the method of moments solution of the electric field integral equation is developed and used in order to evaluate the MIMO channel matrix accurately. The model is called the channel model with electric fields (MEF) and it calculates the exact fields via the radiation integrals, and hence, it is rigorous except the random scatterer environment. The accuracy of the model is further verified by the measurement results. Thus, it is concluded that MEF achieves the accuracy over other approaches which are incapable of analyzing antenna effects in detail.

Making use of the presented technique, MIMO performance of printed dipole arrays is analyzed. Effects of the electrical properties of printed dipoles on the MIMO capacity are explored in terms of the relative permittivity and thickness of the dielectric material. Appropriate dielectric slab configurations yielding high capacity printed dipole arrays are presented. The numerical efficiency of the technique (particularly for freestanding and printed dipoles) allows analyzing MIMO performance of arrays with large number of antennas, and high performance array design in conjunction with well-known optimization tools. Thus, MEF is combined with particle swarm optimization (PSO) to design MIMO arrays of dipole elements for superior capacity. Freestanding and printed dipole arrays are analyzed and optimized, and the adaptive performance of printed dipole arrays in the MIMO channel is investigated. Furthermore, capacity achieving input covariance matrices for different types of arrays are obtained numerically using PSO in conjunction with MEF. It is observed that, moderate capacity improvement is possible for small antenna spacing values where the correlation is relatively high, mainly utilizing nearly full or full covariance matrices. Otherwise, the selection of the diagonal covariance is almost the optimal solution.

MIMO performance of printed rectangular patch arrays is analyzed using a modified version of MEF. Various array configurations are designed, manufactured, and their MIMO performance is measured in an indoor environment. The channel properties, such as the power delay profile, mean excess delay and delay spread, are obtained via measurements and compared with MEF results. Very good agreement is achieved.

Keywords: MIMO, mutual coupling, planar printed arrays, microstrip dipole arrays, microstrip patch arrays, method of moments (MoM), particle swarm optimization (PSO), indoor MIMO measurements, optimal input covariance.

ÖZET

MIMO KABLOSUZ HABERLEŞME SISTEMLERI İÇIN ANTEN ANALIZI/TASARİMİ VE YAYİLİM KANALİ MODELLEMESI

Celal Alp Tunç
Elektrik ve Elektronik Mühendisliği Bölümü Doktora
Tez Yöneticisi: Prof. Dr. Ayhan Altıntaş
Şubat 2009

Alıcı ve vericide çok anten kullanılmasının veri hızında önemli bir artış sağlayacabileceği gösterildiğinden beri, çok-girişli-çok-çıkışlı (multiple-input-multiple-output: MIMO) kablosuz haberleşme sistemleri büyük ilgi görmektedirler. Doğru bir sistem tasarımı için çoklu antenlerin elektromanyetik etkilerinin kablosuz kanala eklenmeleri gereklidir. İlk çalışmalarda bu etkiler genelde ihmal edilmiştir.

Bu çalışmada, MIMO kanalı elektromanyetik bir bakış açısından incelenmiştir. Elektrik alan integral denkleminin momentler metodu çözümüne dayalı bir tam dalga kanal modeli geliştirilmiş ve MIMO kanal matrisinin doğru olarak elde edilmesi için kullanılmıştır. Modele elektrik alanlı kanal modeli (channel model with electric fields: MEF) adı verilmiştir. MEF ışıma integrallerinden uzak alanları tam olarak hesaplamaktadır. Modelin doğruluğu ölçümlerle doğrulanmıştır. Sonuç olarak, MEF anten etkilerini detaylıca inceleyemeyen diğer yaklaşımlardan daha doğru sonuçlar vermektedir.

MEF kullanılarak mikroşerit baskı devre dipol dizilerinin MIMO başarımları incelenmiştir. Baskı devre dipol antenlerin elektriksel özelliklerinin MIMO kapasitesine etkisi araştırılmıştır. Yüksek kapasite sağlayan dielektrik tabaka özellikleri sunulmuştur. Tekniğin nümerik etkinliği sayesinde çok sayıda antenli dizilerin MIMO başarımları incelenebilmekte ve bilinen optimizasyon algoritmaları ile birlikte yüksek başarımlı anten dizisi tasarımları yapılabilmektedir. Böylece, MEF parçacık sürü optimizasyonu (particle swarm optimization: PSO) ile birleştirilerek yüksek kapasiteli MIMO dipol dizileri tasarlanmıştır. Havada asılı ince tel ve baskı devre dipol dizileri incelenmiş ve optimize edilmiştir.

MEF biraz değiştirilerek, baskı devre dikdörtgen yama anten dizilerinin MIMO başarımları incelenmiştir. Bir çok değişik özellikte yama anten dizileri tasarlanmış, üretilmiş ve MIMO başarımları bir bina içi ortamında ölçülmüştür. güç gecikme profili, ortalama artan gecikme ve gecikme dağılımı gibi kanal özellikleri ölçümlerden elde edilmiş ve MEF sonuçları ile karşılaştırmalar yapılmıştşr. Çok iyi bir uyum gözlenmiştir.

Bu çalışma Türkiye Bilimsel ve Teknolojik Araştırma Kurumu (TÜBİTAK) tarafından EEEAG-106E081 kodlu proje kapsamında desteklenmiştir. Ayrıca Avrupa Komisyonu 6. ve 7. Çerçeve Programları (Network of Excellence in Wireless COMmunications: NEWCOM ve NEWCOM++) kapsamında kısmi destek sağlanmıştır.

Anahtar Kelimeler: MIMO, ortak bağlaşım, düzlemsel baskı devre anten dizileri, mikroşerit dipol dizileri, mikroşerit yama dizileri, momentler metodu, parçacık sürü optimizasyonu, bina içi MIMO ölçümleri, en uygun giriş kovaryansı.

ACKNOWLEDGMENTS

I gratefully thank my supervisor Prof. Ayhan Altıntaş, along with Assist. Prof. Defne Aktaş and Assoc. Prof. Vakur B. Ertürk, for their suggestions, supervision, and guidance throughout the development of this thesis.

I would also like to thank Prof. Hayrettin Köymen, Assoc. Prof. Özlem Aydın Çivi and Assist. Prof. İbrahim Körpeoğlu, the members of my jury, for reading and commenting on the thesis.

I would like to express my gratitude to Assoc. Prof. Ali Yapar of Istanbul Technical University for teaching me electromagnetics, and also to Prof. Levent Gürel for encouraging me for the graduate study on electromagnetics.

It is a pleasure to express my special thanks to my dear friends Volkan Açıkel, Yaşar Kemal Alp, Elif Aydoğdu, Onur Bakır, Dr. Ali Bozbey, Ergün "Ergün abi" Hırlakoğlu, Erdinç Ircı, Rohat Melik, Gökçe and Selim Olçum, Uğur "Çeto" Olgun, Alper Kürşat Öztürk, Niyazi Şenlik and Behçet Uğur Töreyin for their cooperation and friendship.

Finally, my deepest gratitude goes to my dearest family and the heavenly light upon me, İlknur, without whom nothing in my life would be that beautiful.

Let the celebrations begin.

This work has been supported by the Turkish Scientific and Technical Research Agency (TÜBİTAK) under the Grant EEEAG-106E081; and also in part by the European Commission in the framework of the FP6/FP7 Network of Excellence in Wireless COMmunications NEWCOM/NEWCOM++.

Contents

List of Figures

List of Tables

List of Abbreviations

2D	Two Dimensional
3D	Three Dimensional
AdaM	Adaptive MIMO
AoA	Angle of Arrival
AoD	Angle of Departure
AWGN	Additive White Gaussian Noise
BER	Bit Error Rate
CDMA	Code Division Multiple Access
c.s.g.	Circularly Symmetric Gaussian
DOA	Direction of Arrival
EFIE	Electric Field Integral Equation
EM	Electromagnetics
EMF	Electromotive Force
FDTD	Finite Difference Time Domain
FSLA	Freestanding Linear Dipole Array
FP	Feed Point
FS	Freestanding Dipole
GA	Genetic Algorithm
IFA	Inverted F-Antennas
i.i.d.	Independent and Identically Distributed
LoS	Line of Sight
MC	Mutual Coupling

MEA	Multi-Element Antenna
MEF	Channel Model with Electric Fields
MEMS	Microelectromechanical Systems
MIMO	Multiple Input Multiple Output
MoM	Method of Moments
NFS	Near Field Scatterers
OFDM	Orthogonal Frequency Division Multiplexing
PDF	Probability Density Function
PDP	Power Delay Profile
PIFA	Planar Inverted F-Antennas
PR	Printed Dipole
PSO	Particle Swarm Optimization
RMS	Root Mean Square
RX	Receiver
SIMO	Single Input Multiple Output
SIR	Signal to Interference Ratio
SISO	Single Input Single Output
SMA	Sub Miniature Version A
SNR	Signal to Noise Ratio
TTL	Transistor Transistor Logic
TX	Transmitter
UCA	Uniform Circular Array
ULA	Uniform Linear Array
VBA	Visual Basic Applications
VNA	Vector Network Analyzer

To my Nur and my Family

Chapter 1

Introduction

Multiple-input-multiple-output (MIMO) wireless communication systems have been attracting huge interest, since a boost in the data rate was shown to be possible, using multiple antennas both at the transmitter and receiver [1, 2]. It is obvious that the electromagnetic effects of the multiple antennas have to be correctly incorporated into the wireless channel for an accurate system design, though they are often neglected by the early studies.

In this thesis, the MIMO channel is investigated from an electromagnetics point of view. The accurate and efficient characterization of antenna arrays in the MIMO channel is studied. To ensure the accuracy, we seek for a model for the inclusion of the electromagnetic effects into the channel. Furthermore, the efficiency will yield the rapid analysis of arrays in the MIMO channel that allows the optimization of the system for high communication rate and design of arrays with large number of antenna elements. Moreover, since the choice of the antenna type may affect the channel behavior significantly, a proper model should have the capability to allow performance comparison of different array types.

1.1 Previous Work

Inclusion of the electromagnetic effects of antenna arrays into the MIMO channel has been generally studied from the mutual interactions point of view. Mutual coupling effects on the spatial correlation and bit error rate (BER) were firstly investigated by Luo *et al.* in [3] for a compact space time diversity receiver in a Nakagami fading channel, considering the received signal as the multiplication of the signal without mutual coupling by the array admittance matrix. It was concluded in [3] that, the mutual coupling reduces the spatial correlation and improves BER performance. The reason behind this result was explained by the pattern diversity provided by the distortion of the field pattern due to coupling.

Later, the coupling matrices of [4] were considered. These matrices are obtained via the mutual interactions matrix and termination impedances due to one of the most common circuit models for an antenna array. Svantesson and Ranheim presented results leading to the conclusion that coupling can have a decorrelating effect on the channel matrix and increase the capacity [4].

Wallace and Jensen developed a rigorous network theory framework including the effects of both mutual coupling and antenna matching [5, 6]. Realistic models for channel noise and receiver noise were introduced in [5,6] as well. The scattering parameter matrices were obtained using finite difference time domain (FDTD) method for antenna simulations in different matching network cases, in conjunction with a path-based channel model. It was also shown that, mutual coupling can provide a capacity benefit even for antenna spacings between $0.1 - 0.3$ wavelengths (λ), using appropriate transmitting schemes. Another network theory approach was presented by Waldschmidt *et al.* [7]; and different array configurations exploiting spatial, polarization and pattern diversity were compared in terms of channel capacity.

Expressions were given to compute the correlation coefficient from the far field radiation patterns including mutual coupling effects and termination impedances in [8]; and results on the correlation under different termination conditions were presented [8,9]. Rosengren *et al.* optimized the source impedances of two parallel dipoles to maximize the effective diversity gain [10]. Lau *et al.* discussed the impact of matching network on bandwidth in the wide band case [11]. Wallace and Jensen applied their rigorous network theory framework to mitigate the mutual coupling in compact antenna arrays and formulate optimal (Hermitian) match condition for coupled networks [12]. In addition, they demonstrated the potential of diversity benefit offered by different possible termination conditions. Later, Morris and Jensen expanded the work in [5,6,12] for noisy amplifiers; and showed that matching for minimum noise figure results in more capacity than matching for maximum power transfer does [13]. They further improved the framework to include the noise effects of the receiver front end in [14]. Pattern diversity via coupled two element circular patch antenna array was analyzed in [15] by the use of the network models in [6,7]. Warnick and Jensen generalized the two-port optimal noise matching condition to the multiport case in [16]. The transmission strategy with mutual coupling was discussed and optimal input covariance matrix was given in [17] using the network framework.

The ease of the use of the technique in [4], which allows to obtain the coupling included channel matrix by simply multiplicating the uncoupled one with the coupling matrices of transmitter and receiver, has created lots of different applications of the coupling matrices [18–36]. Janaswamy used them to show the effects of mutual coupling on the received signal to noise ratio (SNR) in [18]. He concluded that, mutual coupling substantially reduces the received SNR with decreasing interelement spacing, even though it can reduce the spatial correlation; and hence the capacity actually falls. He also claimed that, the slight increase in the capacity due to coupling may occur at certain interelement spacing values causing lower spatial correlation, while the received SNR remains constant [18].

Clerckx *et al.* analyzed the impact of mutual coupling on the performance of spatial multiplexing and transmit diversity [19]. With the aid of the coupling matrices, effect of mutual coupling on the interference rejection capabilities of linear and circular arrays in code division multiple access (CDMA) systems was analyzed [20]; and it was shown that, mutual coupling degrades the signal to interference ratio (SIR) improvement capability of the linear array, particularly in the broadside direction. Krusevac *et al.* estimated the MIMO channel capacity in the presence of mutual coupling and spatially correlated noise [21]. Utilizing the coupling matrices, Li and Nie obtained analytical expressions for both the mean received power and spatial correlation [22]; and stated that the decorrelation due to coupling results from the trade off between the mean direction of arrival (DOA) and the pattern diversity. In [23], the dependence of the capacity on the eigenvalues of the coupling matrices was analyzed; and it was shown that, reduced element spacing yields loss in the rank of the channel matrix, thereby decreases the capacity, whereas it can yield an increase in the transmitter and/or received power thus in the capacity, as well. MIMO performance comparison of uniform linear arrays versus circular ones were given in [24, 25]. The coupling matrices also helped in the investigation of the impact of mutual coupling on reverse link performance of a CDMA system with imperfect beam forming [26, 27]; and on the performance of spatial modulation applied to orthogonal frequency division multiplexing (OFDM) [28]. Mutual coupling effect on MIMO cube, which is a twelve element array benefiting from space, polarization and pattern diversities, was analyzed in [29]. Bialkowski *et al.* presented a MIMO channel model [30], in which both antennas and scatterers are considered as wire dipoles, and investigated the system in the strict electromagnetic sense with the aid of the coupling matrices. Antenna selection in the presence of mutual coupling was discussed in [31]; a capacity upper bound was derived and the conditions, under which mutual coupling has positive effect on the capacity were stated in [32]; the diversity order was increased using maximum ratio combining [33] and equal gain

transmission techniques [34]; mutual coupling effects on MIMO adaptive beam forming systems were investigated in [35].

1.2 Contributions of this Thesis

The major contributions of this thesis can be found in the following broad categories, along with the outline of the thesis:

1.2.1 Channel Model with Electric Fields (MEF)

Instead of using the existent channel models in the literature −great majority of which is neither accurate nor efficient and does not allow the analysis of array configurations other than uniform linear arrays of freestanding dipole elements− a full wave electromagnetic model with electric fields (MEF) is developed to evaluate the MIMO channel matrix accurately by including the electromagnetic effects.

In the full-wave channel model proposed in the second chapter of this thesis, the effects of mutual interactions among the array elements are included in the channel matrix using the method of moments (MoM) solution of the electric field integral equation on the antenna elements. Using the Green's function of the environment and evaluating the radiation integrals, the exact fields referring to the array elements are calculated. Hence, antenna effects are accurately incorporated into the wireless channel, which allows us to make comparisons among arrays of linear wire, printed dipole and rectangular patch antennas. Furthermore, the technique is computationally efficient (particularly for freestanding and printed dipoles) allowing MIMO performance analysis of arrays with large number of elements, and high performance array design in conjunction with well-known optimization tools.

1.2.2 Capacity of Printed Dipole Arrays in the MIMO Channel

Utilizing the developed full-wave channel model (MEF), the capacity performance of microstrip printed dipole arrays in the MIMO channel is investigated in this thesis. Freestanding linear arrays of uniform dipole antennas are frequently investigated by incorporating the antenna coupling effects into the MIMO channel [3–36]. However, the performance of printed dipole arrays in MIMO applications are not studied as much as the freestanding ones, though they are advantageous over other antenna types for their low cost, light weight, conformability to the mounting surface and direct integrability with other printed antennas and microwave devices.

In Chapter 3 of this thesis, MIMO capacity of printed dipole arrays is explored and comparisons with freestanding ones are given. Furthermore, we investigate the effects of geometrical and electrical properties of printed arrays (e.g., dielectric thickness and permittivity, surface waves) on the performance in the MIMO channel. Appropriate dielectric slab configurations yielding high capacity printed dipole arrays are presented.

1.2.3 Design of Dipole Arrays with Superior MIMO Capacity

In the fourth chapter of this thesis, due to its numerically efficient nature, MEF is combined with an optimization technique, in order to design dipole arrays with superior MIMO capacity. The particle swarm optimization (PSO) algorithm is chosen to aid MEF in this process. The accuracy and numerical efficiency of the combination is shown by benchmarking its results with both measurements and genetic algorithm (GA) based simulations.

Afterwards, examples of MIMO system designs of freestanding and printed dipoles are introduced. Uniform circular arrays (UCA) of freestanding dipoles are shown to be a reasonable choice for high MIMO capacity, though results for other array configurations outperforming UCAs are also given. Adaptive MIMO array performance of printed dipole arrays with loaded parasitic elements is investigated and compared with that of freestanding dipole arrays.

1.2.4 Capacity of Printed Planar Rectangular Patch Antenna Arrays in the MIMO Channel

MIMO performance of printed rectangular patch arrays is analyzed using a modified version of MEF in Chapter 5. Microstrip patch arrays with various configurations are designed, manufactured, and their MIMO performance is measured in an indoor environment. Very good agreement is achieved between the measurements and simulations by MEF. Effects of the electrical properties of printed patches on the MIMO capacity are explored in terms of the relative permittivity and thickness of the dielectric material.

1.2.5 Numerical Determination of the Optimal Input Covariance in the MIMO Channel

Telatar proved that one should transmit equal powers along each of the transmit antennas to achieve the capacity, when the channel matrix is drawn independent and identically distributed (i.i.d.) from circularly symmetric Gaussian (c.s.g.) random variables in [1]. Since then, the capacity expression derived under this channel assumption is utilized frequently in the literature, whether the channel matrices investigated have i.i.d. c.s.g. entries or not.

In the sixth chapter, considering the fact that the real life channels are correlated, we consider the problem of computing the optimal input covariance matrix that achieves the capacity for three different types of transmitter arrays of isotropic radiators, uncoupled dipoles and coupled ones. We develop a numerical algorithm, based on the particle swarm optimization (PSO) along with our channel model with electric fields (MEF), that allows us to compute the capacity of the MIMO channel and the corresponding capacity achieving input covariance matrix.

It is shown that, moderate capacity improvement is possible for small antenna spacing values where the correlation is relatively high, mainly utilizing nearly full or full covariance matrices.

Note that, an $e^{j\omega t}$ time convention is used and suppressed from the expressions throughout this thesis, where ω is the angular frequency.

1.3 Further Reading

A number of different studies on mutual coupling in MIMO channels can be listed as follows: Wyglinski *et al.* modeled the effects of mutual coupling on beam pattern synthesis using a similar technique to [3]; and they presented results of uplink CDMA cell capacity with mutual coupling [37]. It was shown experimentally in [38] that, the link capacity for an interelement spacing of 0.2λ is not much less than that of a dipole array with 0.5λ spacing, via wide band radio channel measurements at 5.2 GHz. In [39], the diversity gain of a two element array of inverted F-antennas (IFA) was presented, while the mutual coupling effects are calculated by a commercial electromagnetic field solver. Ozdemir *et al.* showed the potential of further decreasing the spatial correlation using near field scatterers (NFS) in [40]. A technique to enhance the received signals in a near field MIMO environment using transmit adaptivity, by selecting a set of

weights adapted to each receiver to be applied to each transmitting antenna, was presented in [41]. Exploiting the coupled radiation patterns in conjunction with ray tracing, it was stated in [42] that, mutual coupling includes pattern diversity into the channel and increases the capacity, when the angle spread of arriving rays at the receiver is large. Rosengren and Kildal presented simulations with the aid of mutually coupled radiation patterns, and experimentally validated them that, the coupling reduces the spatial correlation but also the radiation efficiency. The combined effect was specified to be a significant reduction in capacity [43]. Morris *et al.* introduced the superdirectivity in MIMO systems and stated that, under appropriate constraint on received power or with certain characteristics of receiver noise, superdirectivity can have a dramatic impact on the achievable MIMO performance [44]. Because of the impractical very large capacity bounds, superdirectivity behavior in MIMO arrays is limited by modeling antenna ohmic loss in [45]. The dependency of pattern correlation on mutual coupling was analyzed in [46]. An analytical evaluation of spatial correlation and capacity in the presence of mutual coupling was presented in [47], using spherical eigenmode expansion. Spatial correlation of coupled planar inverted F-antennas (PIFA) was analyzed using a commercial electromagnetic tool in [48]; and Browne *et al.* showed the better performance of PIFA arrays compared with uniform linear arrays via MIMO measurements [49]. Printed planar and conformal dipole arrays in the MIMO channel were analyzed by a method of moments (MoM)/Green's function technique in [50, 51]. Nonuniform dipole arrays were optimized for higher MIMO capacity in [52] using particle swarm intelligence. Mutual coupling compensation for uniform circular arrays was discussed in [36,53], and for PIFA arrays in [54]. Effect of line of sight (LOS) signal blocking, due to moving objects, on the capacity of an indoor MIMO system was investigated in [55]. Jensen and Wallace presented an approach to construct the capacity bound of the continuous-space electromagnetic channel [56].

In the very recent years, novel array configurations for wireless applications have been frequently encountered in the literature. Examples can be listed as follows: printed planar antennas [57] and wrapped microstrips [58] integrated with laptops for wireless local area network applications, reconfigurable antennas [59–64], PIFA [65, 66] and multiband PIFA arrays for MIMO [61, 67, 68]. Vector antennas [69,70], circular polarized microstrips [71] were presented for polarization diversity. Adaptive MIMO arrays employing loaded parasitic elements were studied to improve the channel capacity [72]. Compact microstrip antennas exploiting multiple orthogonal modes [73]; printed monopole antennas [74], microstrip Yagi antennas [75], PIFA antennas electromagnetic compatible with nearby conducting elements [76] were presented for WiMAX and WLAN applications. The use of polarization-agile antennas were advised to improve MIMO capacity [77] against rotation out of optimal polarization. A wideband adaptive MIMO array is analyzed experimentally in [78].

Chapter 2

Channel Model with Electric Fields (MEF)

Multiple-input-multiple-output (MIMO) wireless communication systems have been a focus of interest, due to their ability to increase the capacity in rich scattering environments by using multi-element antenna (MEA) arrays both at the transmitter and the receiver sides [1, 2]. The choice of MEA array type may affect the wireless channel behavior significantly. Therefore, transmitter and receiver antennas must be incorporated into the wireless channel model by including as many electromagnetic effects as possible to have a better system design.

In this chapter a full-wave electromagnetic model with electric fields (MEF) is proposed, to evaluate the MIMO channel matrix accurately by including the electromagnetic effects. Among these effects, emphasis in terms of numerical results is given to incorporation of mutual coupling, since various studies on this subject can be found in the literature [3–36].

Although effects of mutual coupling among the array elements may become significant, they were often ignored in MIMO channel models in earlier studies.

These effects were recently included in the MIMO channel matrix mainly for freestanding linear arrays of uniform side-by-side thin-wire dipole antennas by either performing a network analysis with the aid of the scattering (S-) parameter matrices [5–16], or using coupling matrices obtained from the mutual interaction matrix and terminations [17–36].

Making use of the coupling matrices is one of the most popular approaches to estimate the MIMO channel capacity in the presence of mutual interactions among the array elements. In this approach, firstly a channel matrix is determined which ignores the coupling effects. Then, this channel matrix is multiplied by the *coupling matrices* for the transmitter and receiver to acquire the channel matrix that is assumed to include the mutual coupling effects accurately. It is observed that, this technique is useful only for the inclusion of mutual coupling. However, it has nothing to accomplish more, when the initially found matrix is obtained via a MIMO channel model that is inadequate to involve other electromagnetic properties of antennas, such as the radiation and/or scattering characteristics. Therefore, performance comparisons among various array types fail using such models, since they do not utilize electromagnetic parameters to characterize different antennas.

The problem with the network model in [5] is that, the mutual coupling effects are incorporated twice in the channel model. The network block representing the channel is defined with coupled radiation patterns (active element patterns). Furthermore, S-parameter matrices of the transmitter and receiver are attached to the channel block. However, just the network blocks of the transmit and receive arrays are adequate for the inclusion of mutual coupling, since the in- and outward propagating waves related to these blocks are already coupled. Namely, the channel block should be defined with uncoupled patterns. Another issue with this technique is that, the S-parameters and coupled patterns were obtained using finite difference time domain method or commercial tools that may become

computationally cumbersome for some array configurations, especially for the ones with large number of elements.

In the full-wave channel model proposed in this thesis, the effects of mutual interactions among the array elements through space and surface waves (when printed arrays are considered) are included in the channel matrix using the method of moments (MoM) solution of the electric field integral equation on the antenna elements. Using the Green's function of the environment and evaluating the radiation integrals, the exact fields referring to the array elements are calculated. Hence, antenna effects are accurately incorporated into the wireless channel, which allows us to make comparisons among arrays of linear wire, printed dipole and rectangular patch antennas for the cases whether mutual coupling is significant or not. The stochastic nature of the model is due to randomly distributed scatterers. Consequently, the presented method is rigorous except the scatterer scenario. Furthermore, the technique is computationally efficient allowing MIMO performance analysis of arrays with large number of elements, and high performance array design in conjunction with well-known optimization tools. The model also allows examining the effect of the termination impedance on MIMO capacity.

In this chapter, the formulation of the proposed channel model with electric fields is explained. Numerical results, mainly in the form of channel capacity, correlations and received signal to noise ratio are given. First, the channel model used is benchmarked by both the simulations and measurements of [72] for adaptive freestanding dipole arrays. Assuring the accuracy of the technique, comparisons with the technique in [4] are presented.

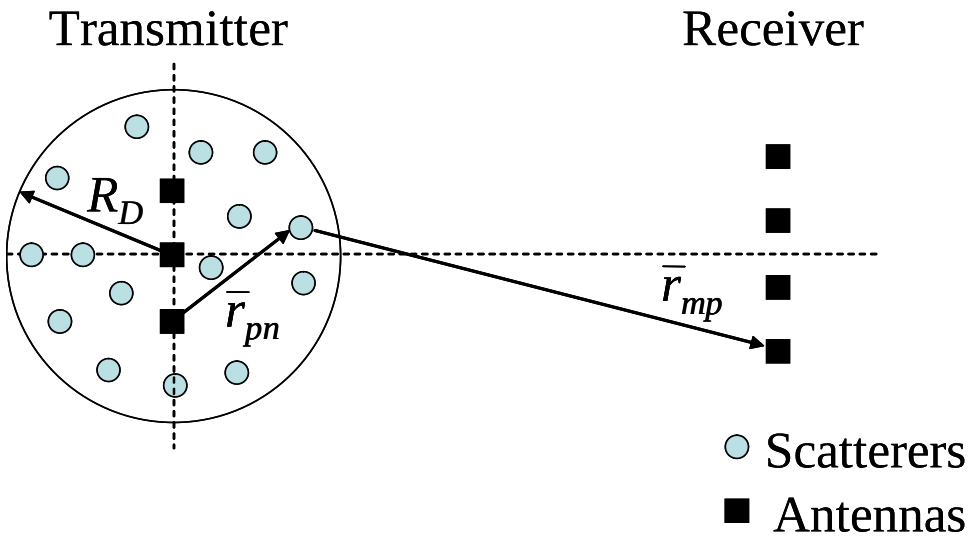

Figure 2.1: Two-dimensional, single-bounce scatterer scenario.

2.1 The MIMO Channel and Capacity

As the scattering environment, a two dimensional (2D), single-bounce geometric model is chosen similar to the one in [4], and is shown in Fig 2.1. It assumes a transmitter (TX) and a receiver (RX) array, and a local cluster of scatterers around TX. The local cluster is a disk of radius R_D including S uniformly distributed scatterers. Note that, the use of any other geometrical scatterer scenario, including multi-bounce ones, is possible but avoided in this chapter for simplicity. The examples of different geometrical multipath scenarios will be utilized in the succeeding chapters.

Assuming flat fading, the received signal vector, $\bar{V}^{rx}$, can be written in terms of the transmitted one, $\bar{V}^{tx}$, and the additive white Gaussian noise vector, $\bar{n}$, with zero mean independent identically distributed (i.i.d.) elements with unit variance as

$$\bar{V}^{rx} = \mathbf{H}\ \bar{V}^{tx} + \bar{n}. \tag{2.1}$$

In (2.1), $\mathbf{H}$ denotes the $R \times T$ channel matrix, where R and T are the number of antenna elements in receiver and transmitter arrays, respectively. Assuming channel knowledge only at the receiver side, an achievable data rate assuming

a diagonal transmission covariance matrix $\mathbf{Q} = \mathcal{E}\left[\bar{V}^{tx}(\bar{V}^{tx})^h\right] = \rho_{_T}\mathbf{I}_T/T$ can be evaluated as

$$\mathcal{C} = \mathcal{E}\left[\log_2\left(\left|\mathbf{I}_R + \frac{\rho_{_T}}{T}\mathbf{H}\mathbf{H}^h\right|\right)\right] \tag{2.2}$$

where $\mathbf{I}_{T,R}$ are the $T \times T$ and $R \times R$ identity matrices, $|.|$ is the matrix determinant, $\rho_{_T} = \mathcal{E}\left[(\bar{V}^{tx})^h\bar{V}^{tx}\right]$ is the total transmitted signal to noise ratio (SNR) with $(.)^h$ and $\mathcal{E}[.]$ denoting the conjugate transpose and expectation operations, respectively. Note that, the information theoretic capacity of this channel under total power constraint $\rho_{_T}$ is

$$\mathcal{C} = \max_{\substack{\mathbf{Q}\geq 0 \\ \mathrm{Tr}(\mathbf{Q})\leq\rho_{_T}}} \left\{\mathcal{E}\left[\log_2\left(\left|\mathbf{I}_R + \mathbf{H}\mathbf{Q}\mathbf{H}^h\right|\right)\right]\right\} \tag{2.3}$$

which is very challenging to compute when $\mathbf{H}$ is not from an i.i.d. circularly symmetric Gaussian distribution, where Tr(.) is the trace operator. As a result, in the rest of this chapter (and in Chapters 3-5), with a slight abuse of the terminology we will refer to the achievable data rate in (2.2) as the capacity of the system, as the vast majority of the literature does. Note that, in Chapter 6, the expression in (2.3) will be used to compute the capacity of various antenna array types.

2.2 Channel Model with Electric Fields (MEF)

The TX array can be modeled by a T-port network, hence by a $T \times T$ impedance matrix, $\mathbf{Z}^{tx}$, which relates the port currents, $\bar{I}^{tx}$, with the source voltages, $\bar{V}^{tx}$, via

$$\bar{I}^{tx} = \left(\mathbf{Z}^{tx} + \mathbf{Z}_M^{tx} + \mathbf{Z}_S\right)^{-1}\bar{V}^{tx} \tag{2.4}$$

due to the circuit model for the nth antenna element of the transmit array shown in Figure 2.2 (a); where $\mathbf{Z}_S$ and $\mathbf{Z}_M^{tx}$ are diagonal matrices, non-zero entries of which are the source and matching impedances, respectively, for each transmit element.

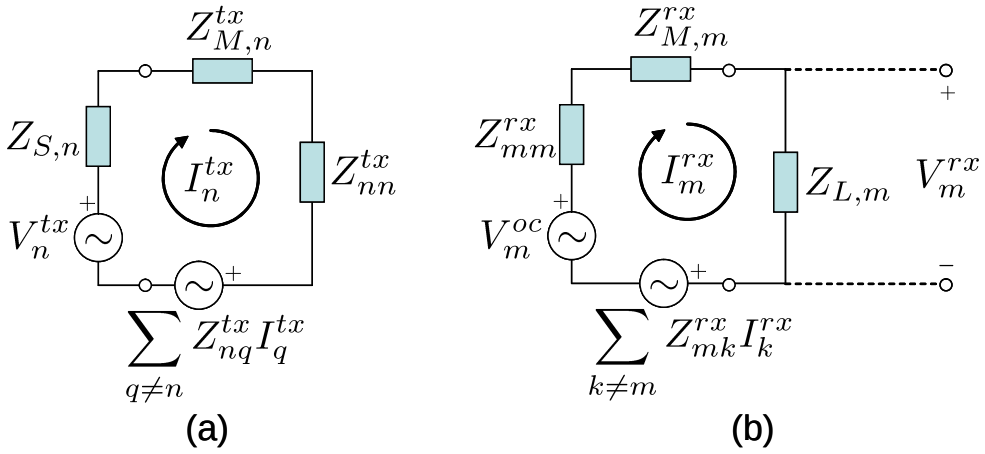

Figure 2.2: The circuit model for the (a) nth TX element (b) mth RX element.

The incident electric field on the pth scatterer in the far zone of the TX array due to the nth transmitter antenna is given by

$$\bar{E}_{np} = \frac{-j\omega\mu_0}{4\pi} \int_{S_n} \bar{J}_n(\bar{r}'_n)\ G(\bar{r}_p, \bar{r}'_n)\ dr'_n. \tag{2.5}$$

In (2.5), μ_0 is the permeability of free space, $\bar{J}_n$ is the current density on the nth TX element due to I^{tx}_n, and $\int_{S_n} dr'_n(\cdot)$ is the surface integration over the element. In addition, $G(\bar{r}_p, \bar{r}'_n)$ represents the Green's function of the environment, where $\bar{r}_p$ and $\bar{r}'_n$ are the position vectors pointing the pth scatterer and nth TX antenna, respectively. The total incident field on the pth scatterer from TX array is obtained as

$$\bar{E}_p = \sum_{n=1}^{T} \bar{E}_{np} = \hat{\theta}^p_1\ E_{p,\theta} + \hat{\phi}^p_1\ E_{p,\phi} \tag{2.6}$$

where $\hat{\theta}^p_1$ and $\hat{\phi}^p_1$ are the unit normal vectors due to elevation and azimuth angles of the pth scatterer in the spherical coordinate system, whose origin coincides with the center of the TX array.

Each scatterer is assumed to have a 2×2 scattering coefficient matrix, $\mathbf{A}_p$, whose entries are, without loss of generality, modeled as i.i.d. Gaussian random variables with zero mean and unit variance. $\mathbf{A}_p$ is given by

$$\mathbf{A}_p = \begin{bmatrix} \alpha^{\theta\theta}_p & \alpha^{\theta\phi}_p \\ \alpha^{\phi\theta}_p & \alpha^{\phi\phi}_p \end{bmatrix}. \tag{2.7}$$

Assuming each scatterer as an isotropic radiator, both θ and ϕ polarized field scattered from the pth scatterer impinging on the mth receiver antenna, $\bar{E}_{pm}$, can be expressed as follows in (2.8)-(2.10):

$$V_{p,\theta}^{0} = \alpha_p^{\theta\theta} E_{p,\theta} + \alpha_p^{\theta\phi} E_{p,\phi} \tag{2.8}$$

$$V_{p,\phi}^{0} = \alpha_p^{\phi\theta} E_{p,\theta} + \alpha_p^{\phi\phi} E_{p,\phi} \tag{2.9}$$

$$\bar{E}_{pm} = \left(\hat{\theta}_2^p \; V_{p,\theta}^{0} + \hat{\phi}_2^p \; V_{p,\phi}^{0} \right) \frac{e^{-jkr_{mp}}}{r_{mp}} \tag{2.10}$$

where k denotes the free space propagation constant and r_{mp} is the distance between the mth RX element and pth scatterer. Note that, in (2.10), the unit normal vectors ($\hat{\theta}_2^p$, $\hat{\phi}_2^p$) are chosen for a different spherical coordinate system, whose origin coincides with the center of the RX array. Total field received by the mth receiver element is given by

$$\bar{E}_m = \sum_{p=1}^{S} \bar{E}_{pm}. \tag{2.11}$$

Making use of another R-port network model for the RX array with the $R \times R$ impedance matrix ($\mathbf{Z}^{rx}$) and the circuit model of the mth receiver element depicted in Figure 2.2 (b), the received signal vector, $\bar{V}^{rx}$, is obtained from the system of linear equations given by

$$\bar{V}^{rx} = \mathbf{Z}_L \left(\mathbf{Z}^{rx} + \mathbf{Z}_M^{rx} + \mathbf{Z}_L \right)^{-1} \bar{V} \tag{2.12}$$

where $\mathbf{Z}_L$ and $\mathbf{Z}_M^{rx}$ are the load and matching impedance matrices (which are diagonal), respectively; and $\bar{V}$ is the induced voltages vector obtained from the total received fields on RX elements. The entries of $\bar{V}$ are evaluated by

$$V_m = \int_{S_m} E_m(r'_m) \; w_m(r'_m) \; dr'_m \tag{2.13}$$

where $E_m = \hat{u}_m \cdot \bar{E}_m$ and $\hat{u}_m$ is the unit normal vector denoting the polarization direction of the element [79]. Furthermore, w_m is the weighting function over the mth receiver element and taken as the current distribution on the element (i.e., mth testing function) yielding indeed a Galerkin's MoM solution.

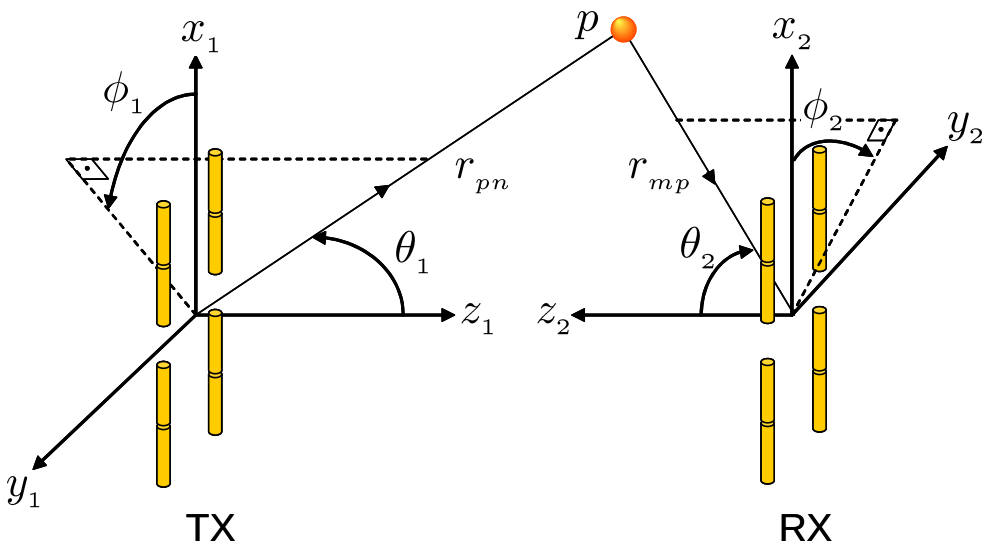

Figure 2.3: MIMO system with freestanding dipole arrays at TX and RX.

In order to find the entries of mutual coupling included $\mathbf{H}$, the following procedure of MEF is proposed:

i. Evaluate $\mathbf{Z}^{tx}$ and $\mathbf{Z}^{rx}$.

ii. Start with $n = 1$.

iii. Activate nth TX element ($V_n^{tx} = 1\text{V},\ V_{k\neq n}^{tx} = 0$).

iv. Calculate the current vector utilizing (2.4).

v. Evaluate (2.5)-(2.13); then, the nth column of the MIMO channel matrix can be simply evaluated as

$$h_{mn} = \frac{V_m^{rx}}{V_n^{tx}} = V_m^{rx}, \tag{2.14}$$

since $V_n^{tx} = 1\text{V}$ and $V_{k\neq n}^{tx} = 0$.

vi. Increase n, and go to (iii).

2.3 MEF for Freestanding Dipole Arrays

For arrays of thin-wire freestanding (FS) dipole elements, the impedance matrices ($\mathbf{Z}^{tx,rx}$) can be evaluated by using the analytical expressions obtained via the induced electromotive force (emf) method for the self (diagonal entries) [79] and mutual impedances (off-diagonal entries) [80]. As well as the induced emf method, the Method of Moments (MoM) solution of the electric field integral equation (EFIE) on the antenna elements can be utilized [79].

Following the aforementioned MEF procedure, the integral in (2.5) can be evaluated in closed form (with the far-zone approximations [79]) by using the free space Green's function given by

$$G(\bar{r}_p, \bar{r}'_n) = \frac{e^{-jk|\bar{r}_p - \bar{r}'_n|}}{|\bar{r}_p - \bar{r}'_n|} \tag{2.15}$$

and piecewise sinusoidal currents on dipole elements, such as

$$\bar{J}_n(\bar{r}'_n) = \hat{a}_x \; I_n^{tx} \; \sin(k|h_n - x'_n|), \tag{2.16}$$

where $\hat{a}_x$ denotes the unit normal vector in x-direction, k is the propagation constant in free space, h_n is the half length of the nth dipole and x'_n is defined in the interval $[-h_n, h_n]$. Thus, (2.5), namely, the incident electric field on the pth scatterer in the far zone of the TX array due to the nth transmitter antenna turns out to be

$$E_{np,\theta} = -j60 \; \cos\theta_1^p \cos\phi_1^p \; I_n^{tx} \; f_n(\theta_1^p, \phi_1^p) \; \frac{e^{-jkr_{pn}}}{r_{pn}} \tag{2.17}$$

$$E_{np,\phi} = j60 \; \sin\phi_1^p \; I_n^{tx} \; f_n(\theta_1^p, \phi_1^p) \; \frac{e^{-jkr_{pn}}}{r_{pn}} \tag{2.18}$$

where

$$f_n(\theta_1^p, \phi_1^p) = \frac{\cos(kh_n \sin\theta_1^p \cos\phi_1^p) - \cos(kh_n)}{1 - \sin^2\theta_1^p \cos^2\phi_1^p}. \tag{2.19}$$

The integral in (2.13) is in the same form with the one in (2.5) and can be evaluated similarly. As a matter of fact, the result of the expression in (2.13) is

nothing but the *induced* or *open circuit voltage* in [79] given by

$$V_m = \bar{E}_m \cdot \bar{l}_m^e \tag{2.20}$$

where $\bar{l}_m^e$ is the vector effective length of the mth receive dipole. The vector effective length of an antenna is defined in [79] as:

$$\bar{l}^e = \frac{\bar{E}_{rad}(1\text{A})}{-j30k\frac{e^{-jkR}}{R}}, \tag{2.21}$$

where $\bar{E}_{rad}(1\text{A})$ is the radiation electric field of the antenna under unit current applied at the antenna port. Then, the vector effective length of the mth free-standing thin-wire dipole is

$$\bar{l}_{m,p}^e = \frac{2}{k}\, f_m(\theta_2^p, \phi_2^p) \left(\hat{\theta}_2^p \, \cos\theta_2^p \cos\phi_2^p - \hat{\phi}_2^p \, \sin\phi_2^p \right). \tag{2.22}$$

Hence, (2.13), namely the entries of $\bar{V}$ for freestanding thin-wire dipoles are equivalent to

$$V_m = \frac{2}{k} \sum_{p=1}^{S} f_m(\theta_2^p, \phi_2^p) \left(E_{pm,\theta} \cos\theta_2^p \cos\phi_2^p - E_{pm,\phi} \sin\phi_2^p \right). \tag{2.23}$$

2.4 Numerical Results

In this section, using the presented MEF approach, performances of linear arrays of freestanding dipole elements are investigated in terms of mean channel capacity, received SNR and channel correlation, for the cases in which mutual coupling is included and ignored (represented by MC and NoMC in the figures, respectively).

First, the accuracy of the method is verified with measurement results of [72]. Then the technique with coupling matrices of [4] is compared with MEF. Freestanding dipole arrays in this chapter are considered to be formed by thin-wire elements of $\lambda/2$ length and $\lambda/200$ radius. Note that λ is the wavelength in free space.

2.4.1 Validation of the Proposed MEF

In order to check the accuracy of the channel model used, we utilize experimental measurements done in [72] under realistic test conditions. In [72], Migliore *et al.* devised an Adaptive MIMO (AdaM) system of identical transmitter and receiver arrays of freestanding (FS) dipoles with two active elements surrounded by six parasitic elements. The geometry of the AdaM system used is rather simple. Thin-wire dipole antennas were placed in a rectangular lattice of 2×4 square grids with edge length $\lambda/4$. Active elements were placed in the middle of the lattice and were $\lambda/2$ apart from each other. On the other hand, the parasitic elements were placed to surround the lattice. Every antenna element was placed at a height of one meter from the floor. The details of the geometry and the experiment, are available in [72] and Chapter 4 of this thesis. Termination impedances of parasitic elements (connected to microelectromechanical systems (MEMS) switches both at TX and RX) were altered to determine the optimal channel capacity using genetic algorithms (GA). For each configuration obtained from GA evaluations of channel simulations, the channel matrix $\mathbf{H}$ is measured by employing a vector network analyzer. The transmitted SNR was selected so as to achieve a channel capacity of 4 bits/s/Hz solely with active antennas and the performance of AdaM system were evaluated with this transmitted SNR throughout the simulations and measurements.

Here, MEF is utilized to simulate the aforementioned measurement environment, and particle swarm optimization (PSO) [81] is employed to find the optimal channel capacity. When modeling the scattering environment, parameters are set to be the same as those of [72], details of which can be found in Chapter 4 of this thesis. Under these conditions, the experiment performed in [72] is simulated. It should be noted that, along with the experiment, the details on the PSO algorithm are discussed in Chapter 4. The results of the channel model in conjunction with PSO are depicted in Figure 2.4 [represented by MEF with

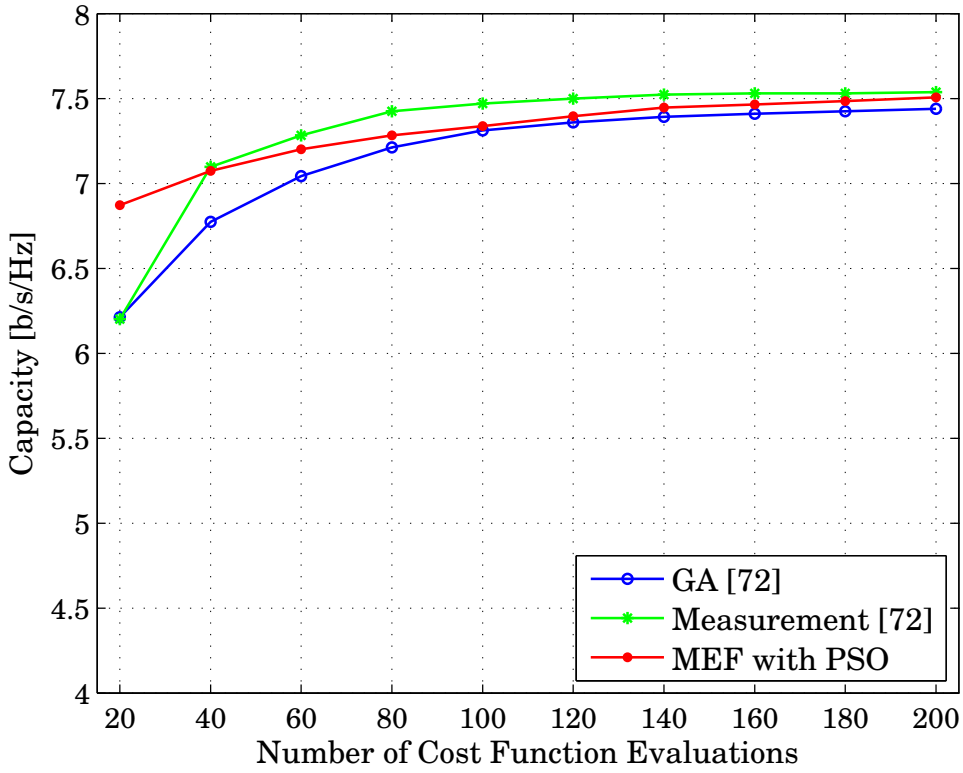

Figure 2.4: Validation of MEF with both simulations and measurements of [72].

PSO] along with the measurement and GA simulation results of [72], and they are all in very good agreement which illustrates the validity and accuracy of the MIMO channel model used.

2.4.2 Comparison with the Coupling Matrices of [4]

As stated before, the coupling matrices of [4] are frequently utilized to include the effects of mutual coupling for FS dipole arrays in various studies [17–36]. Here we compare the method in [4] with MEF.

In [4], for the same circuit models in Figure 2.2, *induced voltages* are defined as

$$\bar{V}_{ind}^{tx} = (\mathbf{Z}_S + \mathbf{Z}_M^{tx} + \mathbf{Z}_{diag}^{tx})(\mathbf{Z}_S + \mathbf{Z}_M^{tx} + \mathbf{Z}^{tx})^{-1}\ \bar{V}_{tx} = \mathbf{C}_T\ \bar{V}_{tx} \quad (2.24)$$

$$\bar{V}_{ind}^{rx} = (\mathbf{Z}_L + \mathbf{Z}_M^{rx} + \mathbf{Z}_{diag}^{rx})(\mathbf{Z}_L + \mathbf{Z}_M^{rx} + \mathbf{Z}^{rx})^{-1}\ \bar{V}\ = \mathbf{C}_R\ \bar{V} \quad (2.25)$$

where $\mathbf{Z}_{diag}$ is the diagonal matrix with self impedances. Afterwards, the channel is defined referring to the induced voltages, such that $h_{mn} = V^{rx}_{ind,m}/V^{tx}_{ind,n}$. Thus, the mutual coupling included channel matrix ($\mathbf{H}$) is expressed in terms of the one without coupling ($\mathbf{H}'$) as $\mathbf{H} = \mathbf{C}_R\ \mathbf{H}'\ \mathbf{C}_T$. Neglecting mutual coupling (i.e., $\mathbf{Z}^{tx} = \mathbf{Z}^{tx}_{diag}$ and $\mathbf{Z}^{rx} = \mathbf{Z}^{rx}_{diag}$), coupling matrices ($\mathbf{C}_{R,T}$) become identity matrices. Whereas, MEF relates the channels to the source voltages at TX and load voltages at RX.

Figures 2.5-2.7 show the comparison of two techniques in terms of the capacity (Figure 2.5), correlation (Figure 2.6) and received SNR per RX branch (Figure 2.7) for a MIMO system formed by identical two element FS dipoles both at RX and TX. For these results, the single-bounce scenario is formed by locating $S = 100$ uniformly distributed scatterers around the transmitter within a disk of radius of $R_D = 200\lambda$, on the plane perpendicular to the direction of the current on antenna elements. Transmit and receive arrays are assumed to be located 300λ away from each other in a broadside manner, formed by $R = T = 2$ uniform side-by-side dipoles, where the interelement spacing for both arrays is Δ. Results are generated for different Δ values between 0.1λ and λ. In the results, the transmit SNR ($\rho_{_T}$) is fixed for all Δ values in such a way that the average received SNR including mutual coupling, averaged over all interelement spacing values, is 10 dB. The capacity results are obtained by averaging the MIMO channel capacity over $N_R = 1000$ channel realizations. It should be noted that, $N_R \cdot S$ scatterer locations and coefficient matrices are generated and kept in the memory, then used for all numerical simulations. Therefore, effects of these random parameters on comparisons are eliminated for the same scatterer geometry.

The impedances in the circuit models are chosen such that

$$Z_{S,n} = \left(Z^{tx}_{nn}\right)^* \tag{2.26}$$

$$Z_{L,m} = \left(Z^{rx}_{mm}\right)^* \tag{2.27}$$

$$Z^{tx}_{M,n} = Z^{rx}_{M,m} = 0\ \Omega \tag{2.28}$$

in order to have a conjugate matching condition, where $(.)^*$ is the conjugate operator.

The channel correlation is defined by the correlation coefficient given by

$$\rho_{_h} = \left| \frac{\mathcal{E}\left[h_{11}h_{12}^*\right]}{\sqrt{\mathcal{E}\left[|h_{11}|^2\right]\ \mathcal{E}\left[|h_{12}|^2\right]}} \right|, \tag{2.29}$$

and the received SNR per RX branch is calculated by

$$\rho_{_R} = \frac{\mathcal{E}\left[(\bar{v}_{rx})^h\ \bar{v}_{rx}\right]}{R} \tag{2.30}$$

where $\bar{v}_{rx}$ is the received voltages vector obtained by $\bar{v}_{rx} = \mathbf{H}\ \bar{v}_{tx}$, when $\bar{v}_{tx}$ is the input voltages vector under the condition that all transmit elements are given the same amount of power, that is

$$\bar{v}_{tx} = \begin{bmatrix} \sqrt{\frac{\rho_{_T}}{T}} \\ \vdots \\ \sqrt{\frac{\rho_{_T}}{T}} \end{bmatrix}. \tag{2.31}$$

First, results by MEF are plotted for a fixed transmit power of $\rho_{_T} = 104$ dB (for an average received SNR of 10 dB). Then, with the aid of the MEF, coupling ignored channel matrix referred to the induced voltages ($\mathbf{H}'$) is found and mutual coupling effects are incorporated using the coupling matrices in [4], which is denoted as MEF$_i$ in Figures 2.5-2.7. Similar behavior for mean capacity and correlation is observed with a shift of received SNR around 5 dB. This offset is due to the fact that channel coefficients without mutual coupling are defined as $h_{mn}^{nomc} = V_m/V_n^{tx}$ in [4] whereas $h_{mn}^{nomc} = Z_{L,m}/(Z_{L,m} + Z_{M,m}^{rx} + Z_{mm}^{rx})\ V_m/V_n^{tx}$ in the MEF. Reducing the transmit power to 99 dB in the MEF$_i$ case, the perfect agreement is obtained.

Therefore, one can say that, the use of coupling matrices of [4] is appropriate under the following conditions:

- The channel should be defined referring to the induced voltages at the TX and RX.

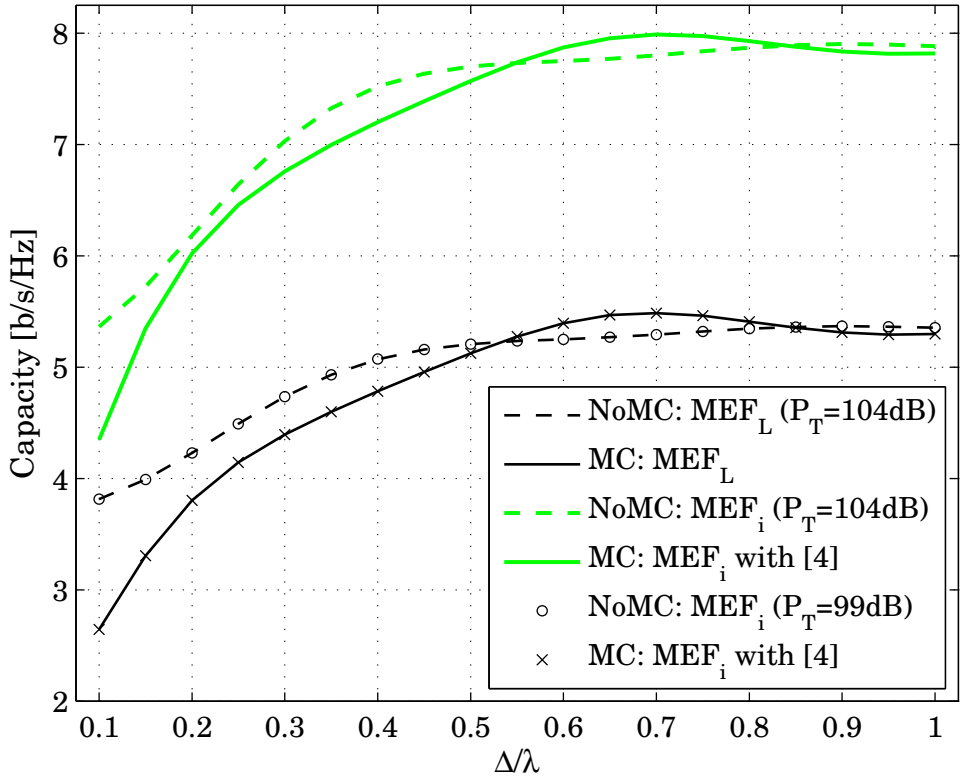

Figure 2.5: Comparison of the proposed MEF with the method in [4] in terms of capacity. Identical FLDA with 2 side-by-side dipoles are located both at TX and RX. Conjugate matching is applied at the terminals.

- The model to generate the mutual coupling excluded channel matrix should be sufficiently accurate that is capable of analyzing array characteristics such as electrical and geometrical properties in detail.

For instance in [18], although these coupling matrices are utilized, the channels are defined referring to the terminal voltages, therefore the results may be misleading.

Moreover, when a comparison between different antenna types is desired in a negligible mutual coupling situation ($\mathbf{C}_{R,T} \approx \mathbf{I}_{R,T}$), the overall channel matrices for both types will become roughly identical ($\mathbf{H} \approx \mathbf{H}'$). If $\mathbf{H}'$ is obtained via a channel model that is inadequate to involve electromagnetic properties of antennas, the technique in [4] will not completely integrate the antenna effects

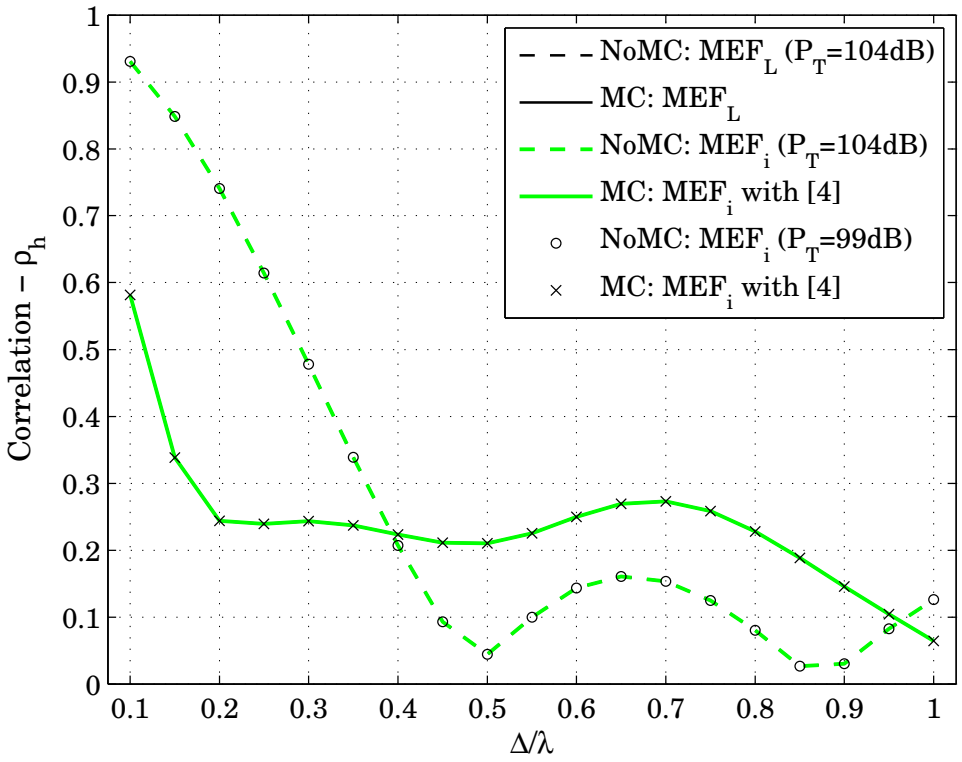

Figure 2.6: Comparison of the proposed MEF with the method in [4] in terms of correlations. Note that the green and black curves are on the top of each other.

into the wireless channel, and hence, the comparison may fail. However, utilizing MEF, antenna effects are accurately incorporated by the computation of the exact fields of array elements, for the cases whether mutual coupling is negligible or not.

Inspecting Figures 2.5-2.7 from the MIMO performances of FS dipoles point of view, one can conclude with the following remarks: As expected, for small interelement spacings, the effect of mutual coupling reduces the capacity, due to decreased received SNR even though the correlation is lower. Considering the capacity results, mutual coupling can be said to be negligible for interelement spacings larger than 0.5λ for freestanding dipole elements. It should be noted that, for some interelement spacing values, mutual coupling included capacity can be higher than the one without coupling. This phenomenon was explained before in early studies [4, 6] by the deformation of the antenna pattern due to mutual coupling. Later [19] stated that mutual coupling is beneficial to the

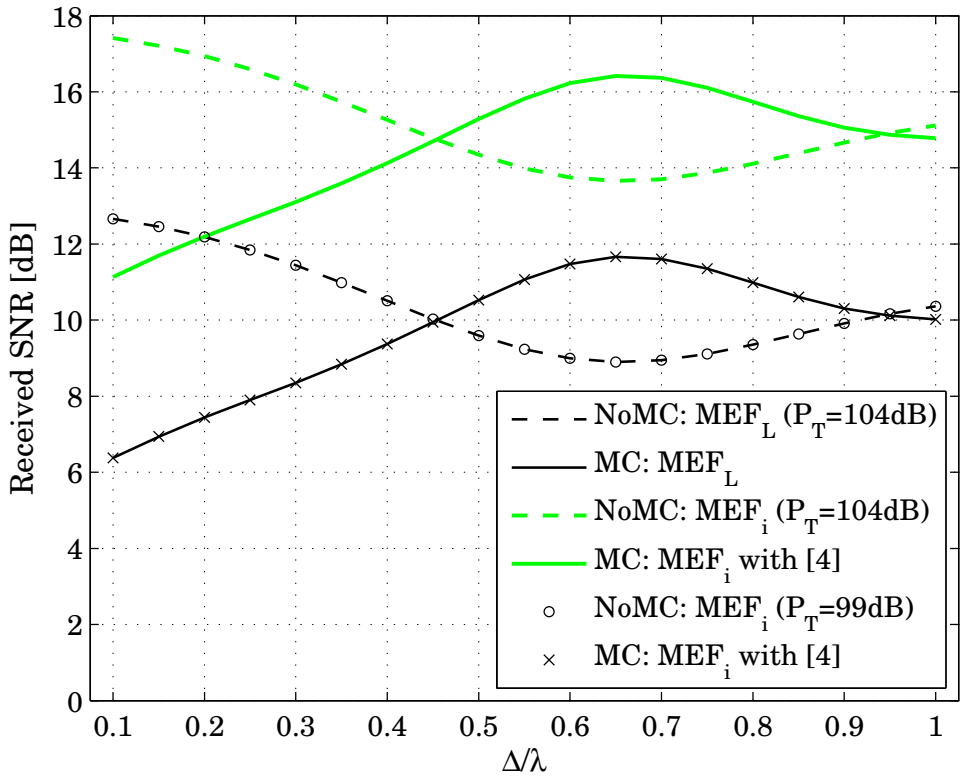

Figure 2.7: Comparison of the proposed MEF with the method in [4] in terms of received SNR per RX branch.

channel energy for antenna distances between 0.4 and 0.9λ, under the directional scattering conditions and when the receiver array is oriented orthogonally to the main direction of arrival.

2.5 Conclusions

A full-wave channel model (MEF) based on the method of moments solution of the electric field integral equation is presented and used in order to evaluate the MIMO channel matrix accurately. MEF calculates the exact fields via the radiation integrals, and hence, it is rigorous except the scatterer scenario. The accuracy of the model is further verified by the measurement results of [72]. Thus, it is concluded that MEF achieves the accuracy over other approaches which are incapable of analyzing antenna effects in detail.

Making use of the presented technique may also help in the analysis of effects of geometrical and electrical properties - such as dielectric thickness and permittivity, surface waves or termination impedances - on the communication system performance. Hence, investigation of printed dipole arrays in the MIMO channel is accomplishable via MEF, and is discussed in the next chapter.

Moreover, the numerical efficiency of the technique allows analyzing MIMO performance of arrays with large number of antennas, and high performance array design in conjunction with well-known optimization tools. Our studies on the particle swarm optimization of dipole arrays for superior MIMO capacity will be presented in Chapter 4.

Chapter 3

Capacity of Printed Dipole Arrays in the MIMO Channel

The choice of the multi-element antenna array type in MIMO communication systems may affect the wireless channel behavior significantly. Freestanding linear arrays of uniform dipole antennas are frequently investigated by incorporating the antenna coupling effects into the MIMO channel [3–36]. However, the performance of printed dipole arrays in MIMO applications are not studied as much as the freestanding ones, though they are advantageous over other antenna types for their low cost, light weight, conformability to the mounting surface and direct integrability with other printed antennas and microwave devices.

In this chapter, we examine the MIMO channel capacity of printed dipole arrays. Antenna and electromagnetic effects, such as interactions among the dipoles through space and surface waves and radiated fields, are accurately incorporated into the wireless channel by MEF, namely, using the method of moments (MoM) solution of the electric field integral equation (EFIE) and by calculating the radiation integrals.

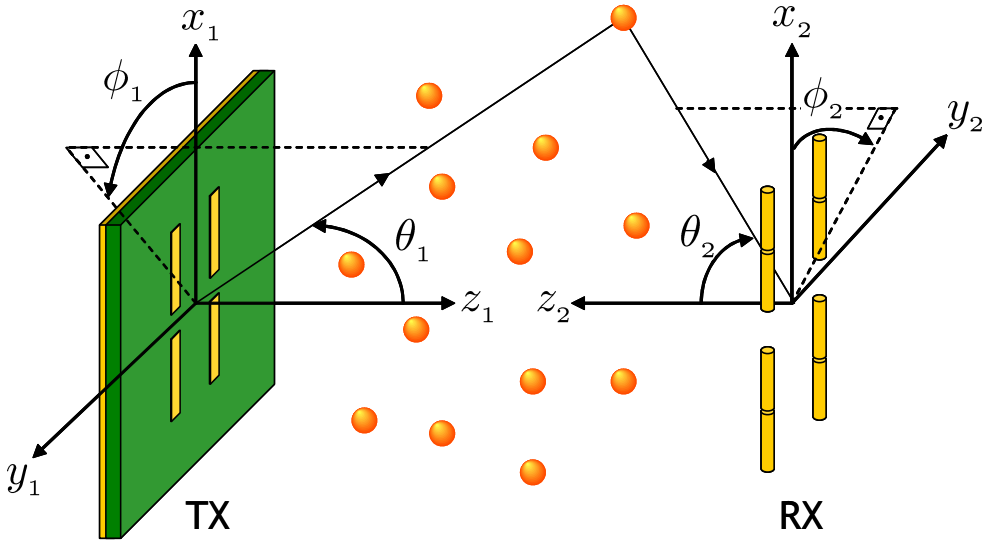

Figure 3.1: MIMO system with a printed dipole array at TX in a three dimensional, single-bounce scatterer environment.

MIMO capacity of printed dipole arrays is explored and comparisons with freestanding ones are given. Furthermore, we investigate the effects of geometrical and electrical properties of printed arrays (e.g., dielectric thickness and permittivity, surface waves) on the performance in the MIMO channel. Appropriate dielectric slab configurations yielding high capacity printed dipole arrays are presented.

3.1 MEF for Printed Dipole Arrays

In this chapter, the scattering environment is considered to be a three dimensional (3D), single-bounce geometric model as shown in Figure 3.1. It assumes S uniformly distributed scatterers in a specified volume. As the capacity of the system, the achievable data rate in (2.2) is used as well as the previous chapter.

As the first step of the MEF procedure in the case of printed arrays, different Green's function representations are used in a computationally optimized manner based on the distance between array elements [82–86] for the evaluation of the self and mutual interactions. The investigation of printed dipole arrays is done

utilizing the more general two dimensional finite array of printed dipoles [82,84], using a hybrid MoM/Green's function technique. Assuming an ideal delta gap generator at the terminals of each center-fed dipole and using Galerkin's MoM solution, entries of the mutual interaction matrices ($\mathbf{Z}^{tx,rx}$) are obtained as in Bakır's thesis [84]. The electric surface current density on each dipole is expanded in terms of one piecewise sinusoidal mode which is found to be successful in [82,83]. Bakır's thesis [84] is a comprehensive study on the evaluation and implementation of grounded dielectric slab Green's functions that may be referred along with [82,83] and [86], for in depth investigation.

The electric field of a single x-directed printed element in a transmit mode printed dipole array resulting from the radiation integral in (2.5) and incident on the pth scatterer is given by [82]

$$E_{np,\theta} = -j60k \; P_\theta^p \cos\phi_1^p \; I_n^{tx} \; F_n(ku_p, kv_p) \; \frac{e^{-jkr_{pn}}}{r_{pn}} \tag{3.1}$$

$$E_{np,\phi} = j60k \; P_\phi^p \sin\phi_1^p \; I_n^{tx} \; F_n(ku_p, kv_p) \; \frac{e^{-jkr_{pn}}}{r_{pn}} \tag{3.2}$$

where

$$P_\phi^p = \frac{\cos\theta_1^p}{\cos\theta_1^p - j\gamma_p \cot(kd\gamma_p)} \tag{3.3}$$

$$P_\theta^p = P_\phi^p \; \frac{\gamma_p \left[\gamma_p + j\cos\theta_1^p \tan(kd\gamma_p)\right]}{\epsilon_r \cos\theta_1^p + j\gamma_p \tan(kd\gamma_p)} \tag{3.4}$$

$$\gamma_p = \sqrt{\epsilon_r - \sin^2\theta_1^p} \tag{3.5}$$

$$u_p = \sin\theta_1^p \cos\phi_1^p \tag{3.6}$$

$$v_p = \sin\theta_1^p \sin\phi_1^p \tag{3.7}$$

and ϵ_r is the relative permittivity of the dielectric slab with thickness d. $F_n(ku_p, kv_p)$ is the Fourier transform of the single piecewise sinusoidal expansion mode, and can be expressed as

$$F_n(ku_p, kv_p) = \frac{2k_e \left[\cos(k_e h_n) - \cos(ku_p h_n)\right]}{\sin(k_e h_n) \left[k^2 u_p^2 - k_e^2\right]} \tag{3.8}$$

where h_n is the half length of the nth dipole element, and k_e is the wavenumber of the expansion mode due to the dielectric slab, given by

$$k_e = k\sqrt{\frac{\epsilon_r + 1}{2}}. \tag{3.9}$$

Note that, $F_n(ku_p, kv_p)$ has no v_p dependence here, due to the dipoles being on the xy-plane and in x-direction.

Following the rest of the MEF procedure that is given in the previous chapter, the channel matrix is evaluated accurately and efficiently for printed dipole arrays, as well.

3.2 Numerical Results

In this section, numerical results on the MIMO capacity of printed dipole antennas and comparisons with freestanding ones are given. The 3D scattering environment is considered to be formed by 20 uniformly distributed point scatterers located in a common office room of dimensions 8 meters length, 3 meters width and height as in [72]. The capacity results are obtained by averaging the MIMO channel capacity over 1000 different channel realizations.

Freestanding dipole arrays in this section are considered to be formed by thin-wire elements of $\lambda/2$ length and $\lambda/200$ radius, whereas printed ones are of $\lambda_e/2$ length and $\lambda/100$ width that are placed on top of a dielectric substrate with a dielectric constant of ϵ_r and a thickness of d above a ground plane. Note that λ is the wavelength in free space and $\lambda_e = \lambda/\sqrt{0.5(\epsilon_r + 1)}$ is the effective wavelength due to the dielectric material.

For all numerical results presented from this point forward, the following receiver array configuration is used: $R = 2 \times 2 = 4$ freestanding dipoles are located in a plane broadside to the transmitter array. Here, 2×2 stands for a configuration as the square matrix notation, such that, 2 side-by-side pairs of

2 collinear antennas form the $R = 4$ element RX array, as illustrated in Figure 3.1. Both horizontal and vertical spacings between phase centers of dipoles are set to be 0.75λ. The distance between the parallel TX and RX planes is taken as 7.5 meters. Furthermore, for all the following numerical results, the circuit models in Figure 2.2 are utilized. The termination impedances are considered to be 50 Ω (i.e., $Z_{S,n} = Z_{L,m} = 50\ \Omega$) and conjugate matching is assumed (i.e., $Z_{nn}^{tx} + Z_{M,n}^{tx} = Z_{S,n}^{*} = 50\ \Omega$ and $Z_{mm}^{rx} + Z_{M,m}^{rx} = Z_{L,m}^{*} = 50\ \Omega$). Also, the transmit SNR is fixed; such that, the single input multiple output (SIMO) capacity for a single freestanding dipole at TX is 4 bits/sec/Hz.

In Figure 3.2 and 3.3, the MIMO performance of printed dipole arrays is compared with that of freestanding ones. For this purpose, first, the dielectric slab parameters are selected as $\epsilon_r = 3.0$ and $d = 0.1\lambda$ yielding approximately the same SIMO capacity of the freestanding dipole (see Figure 3.2). Then, MIMO capacities of TX arrays of printed (PR) and freestanding (FS) dipoles with both side-by-side ($1 \times T$) and collinear ($T \times 1$) arrangements, are plotted versus the interelement spacing for $T = 2$ in Figure 3.2 (a) and for $T = 3$ in Figure 3.2 (b) along with the SIMO capacities.

Inspecting Figure 3.2 (a) and (b), it can be said that, the capacity of FS dipoles show a fluctuating behavior versus interelement spacing, whereas printed dipoles are more stable in that sense. Furthermore, as the number of antenna elements increases, the variation in the capacity raises particularly for FS dipoles. For both types of dipoles, it is observed that, after certain interelement spacing values, the capacities of side-by-side or collinear arrangements do not differ significantly.

The effect of mutual coupling is investigated in Figure 3.3 (a) and (b), by plotting $\mathcal{C}_{nomc} - \mathcal{C}_{mc}$, where $\mathcal{C}_{nomc}$ is the capacity obtained ignoring mutual coupling by setting the off-diagonal elements of the mutual interactions matrix to zero; whereas $\mathcal{C}_{mc}$ is the capacity in the regular (coupled) case. It is observed

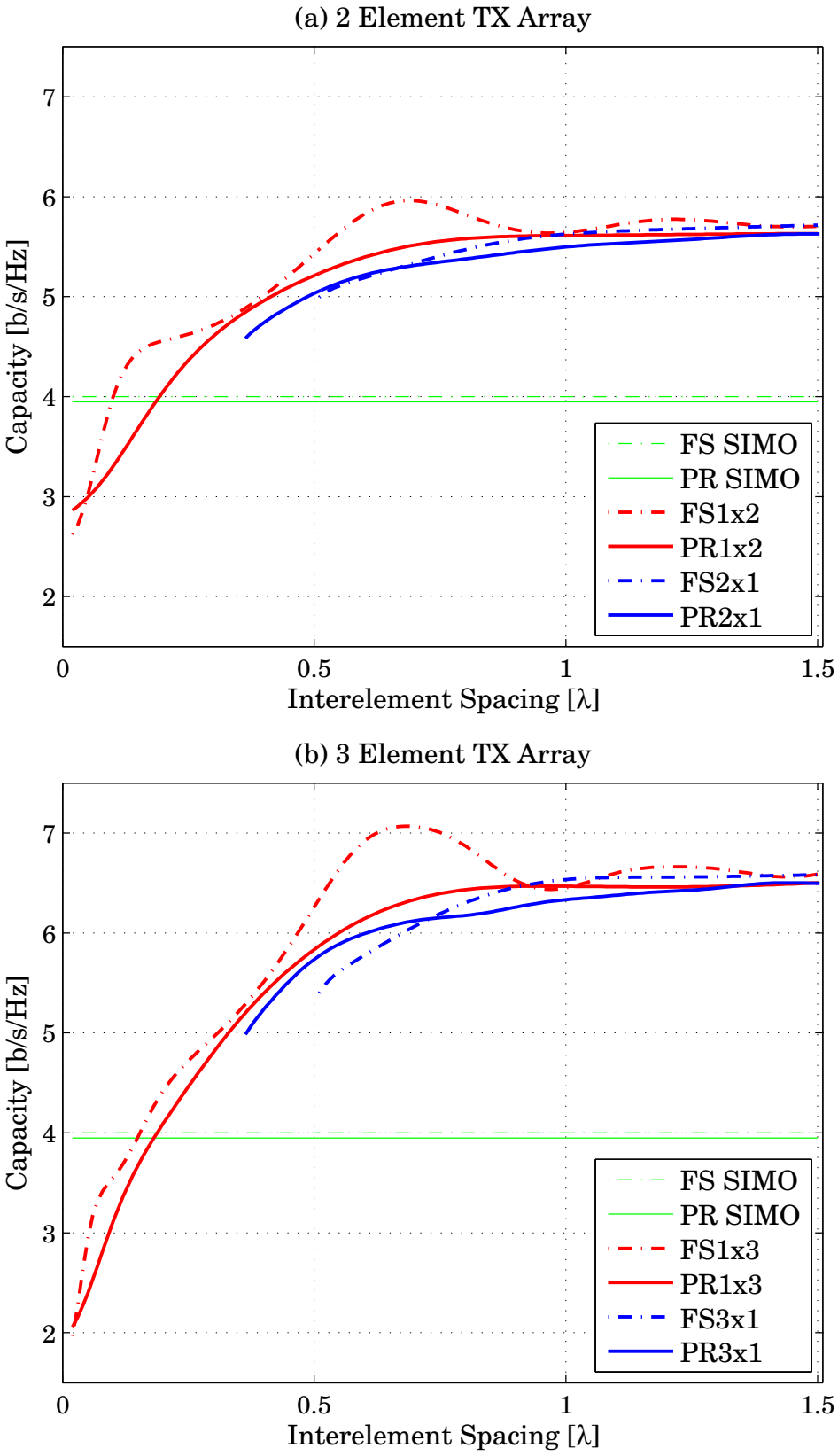

Figure 3.2: Capacity versus interelement spacing for T-element freestanding (FS) and printed (PR) dipole arrays with side-by-side ($1 \times T$) and collinear ($T \times 1$) arrangements. (a) $T = 2$, (b) $T = 3$.

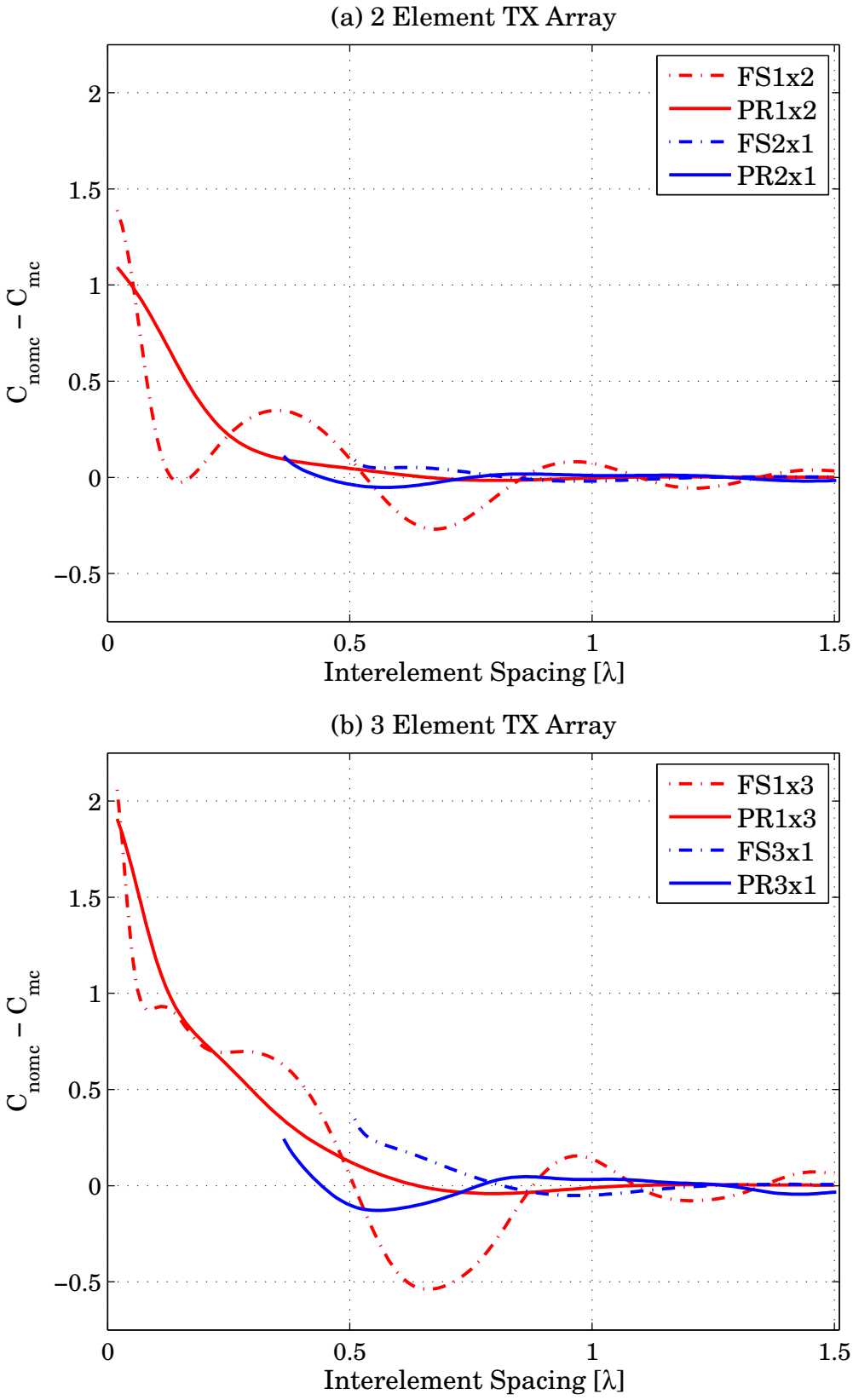

Figure 3.3: Mutual coupling effects on the capacity for T-element freestanding (FS) and printed (PR) dipole arrays with side-by-side ($1\times T$) and collinear ($T\times 1$) arrangements. (a) $T = 2$, (b) $T = 3$.

that, printed dipole arrays are less sensitive to mutual coupling than the FS ones; and coupling can be safely ignored for element separations larger than 0.5λ. For the collinear arrangement of printed dipoles, the coupling is mainly due to the surface waves; and it should be noted that, coupling through surface waves has no significant effect on the MIMO channel capacity. The fluctuations for FS dipoles are observed for the mutual coupling effect as well, whereas the curves for printed dipoles are smoother. However, for higher ϵ_r values, $\mathcal{C}_{nomc} - \mathcal{C}_{mc}$ results for printed arrays may oscillate slightly due to increased surface waves.

In order to examine the effect of dielectric constant (ϵ_r) on the MIMO performance, the capacity is plotted against varying ϵ_r and element separation (Δ) in Figure 3.4 for printed arrays with 3 side-by-side dipoles (1×3), while the thickness of the material is kept as $d = 0.1\lambda$. It is observed that, the capacity variation versus interelement spacing has a similar behavior for different ϵ_r values. In Figure 3.6, the variation of the capacity is plotted for 4 different separation values (i.e., $\Delta = 0.45\lambda, 0.5\lambda, 0.55\lambda, 0.6\lambda$), and it is seen that, increasing ϵ_r slightly raises the channel capacity due to increased beam width in the azimuth pattern of printed dipoles [82, 87].

The effect of the dielectric thickness (d) on the capacity is explored in Figures 3.5 and 3.7. In Figure 3.5, the capacity is plotted versus varying d and element separation, while the dielectric constant is kept constant at $\epsilon_r = 3$. Exceeding certain d values, capacity curves are observed to be bent. For the same cross-sections in Figure 3.6, the variation of the capacity due to the dielectric thickness is plotted in Figure 3.7. For small d values, the images due the ground plane tend to cancel the effects of dipoles, and hence the capacity is low. Up to certain thickness values, the capacity increases drastically due to increased radiation intensity in both the azimuth and elevation planes, then it starts to decay because of the increased number of surface wave modes so that the losses due to the surface waves increase [88].

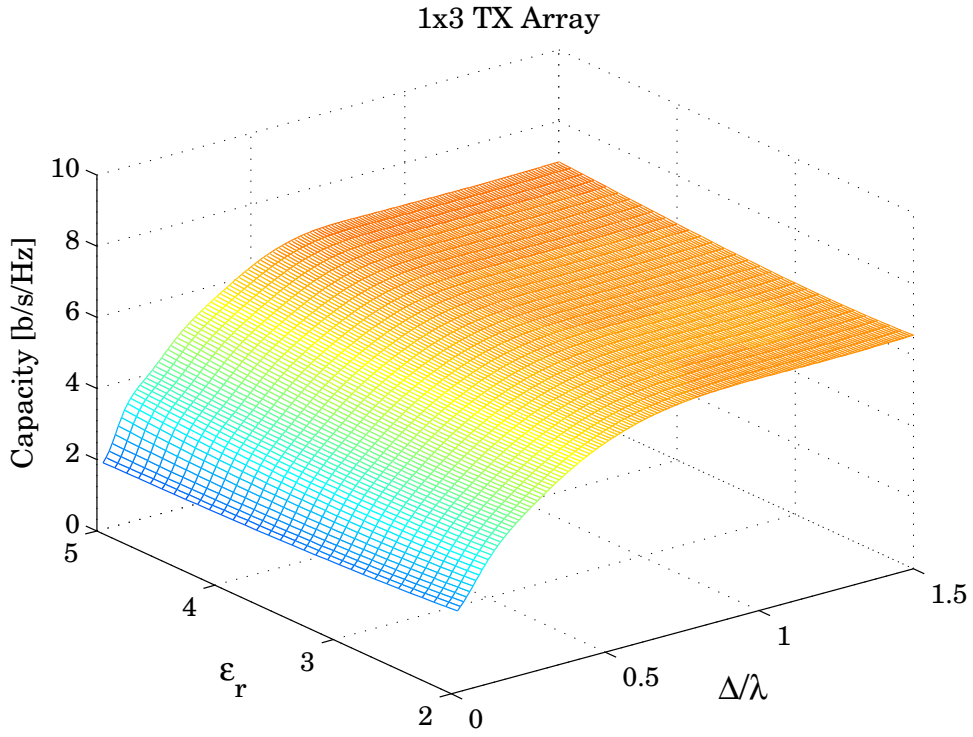

Figure 3.4: Capacity versus dielectric permittivity (ϵ_r) and interelement spacing (Δ) for printed arrays with 3 side-by-side dipoles.

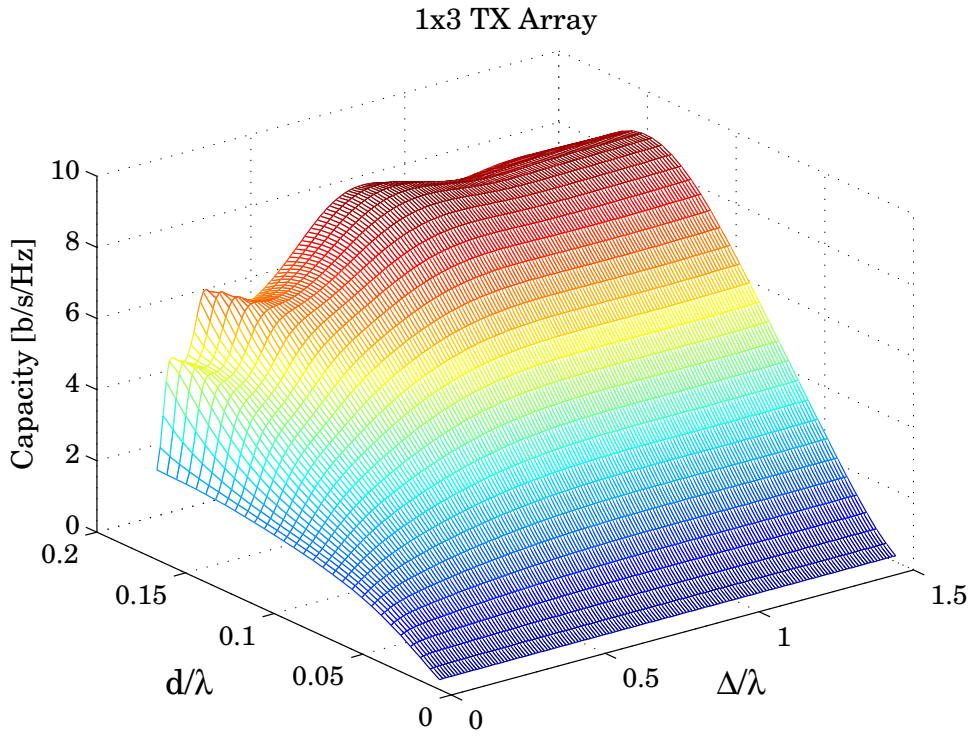

Figure 3.5: Capacity versus dielectric thickness (d) and interelement spacing (Δ) for printed arrays with 3 side-by-side dipoles.

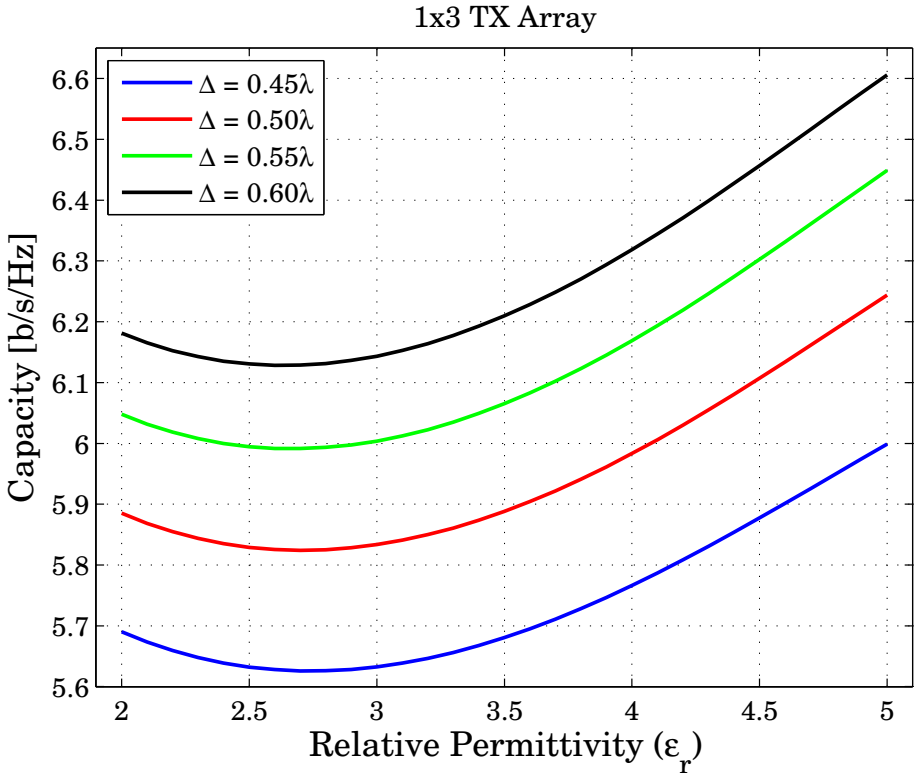

Figure 3.6: Capacity versus dielectric permittivity for printed arrays with 3 side-by-side dipoles.

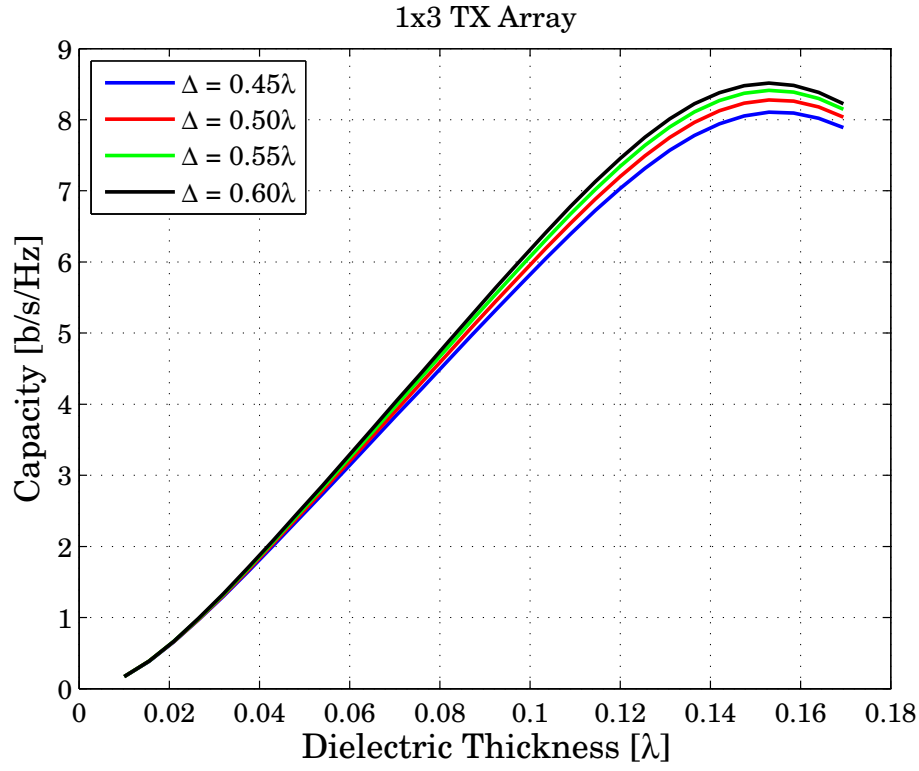

Figure 3.7: Capacity versus dielectric thickness for printed arrays with 3 side-by-side dipoles.

In Figure 3.8, the capacity is plotted against varying ϵ_r and d, while the element separation is kept constant at $\Delta = 0.5\lambda$. The maxima where the capacity curves start to bent can be explicitly seen. Note that, all the capacity values at these maxima are larger than the largest capacity of FS array. Figure 3.9 illustrates the (ϵ_r, d) configurations yielding the maximum capacity values. A curve with the relation

$$\frac{d}{\lambda}\sqrt{\epsilon_r} \approx 0.55\pi \tag{3.10}$$

can be fitted to the configuration data. Note that, the fitting curve relation in (3.2) is found to be valid for other Δ values as well.

The interelement spacing required to exceed the SIMO capacity for printed dipoles, Δ_{exceed}, depends on the dielectric parameters (more on d than ϵ_r). For example, inspecting Figure 3.10, for a substrate of $\epsilon_r = 3$, $\Delta_{exceed} = 0.19\lambda$ when $d = 0.1\lambda$, whereas it becomes 0.05λ when $d = 0.17\lambda$. Thus, printed arrays with closely spaced elements that have a relatively high capacity can be designed by using appropriate dielectric slabs. However, if the dielectric substrate is not chosen carefully, then Δ_{exceed} for printed dipoles can be larger than that of the FS dipoles, as seen in Figure 3.2, resulting SIMO capacity to be better than MIMO capacity. This is obviously an undesired situation for designers. Besides, high MIMO capacity for arrays with elements closely placed can also be obtained by properly adjusting the termination impedances. This is shown in [5,6] for FS dipole cases.

3.3 Conclusions

MIMO performance of printed dipole arrays is analyzed using the full-wave channel model (MEF), which is given in Chapter 2. The capacity comparisons of printed dipole arrays with freestanding (FS) ones are given. It is observed that, printed dipoles are less sensitive to the mutual coupling than FS ones in terms of

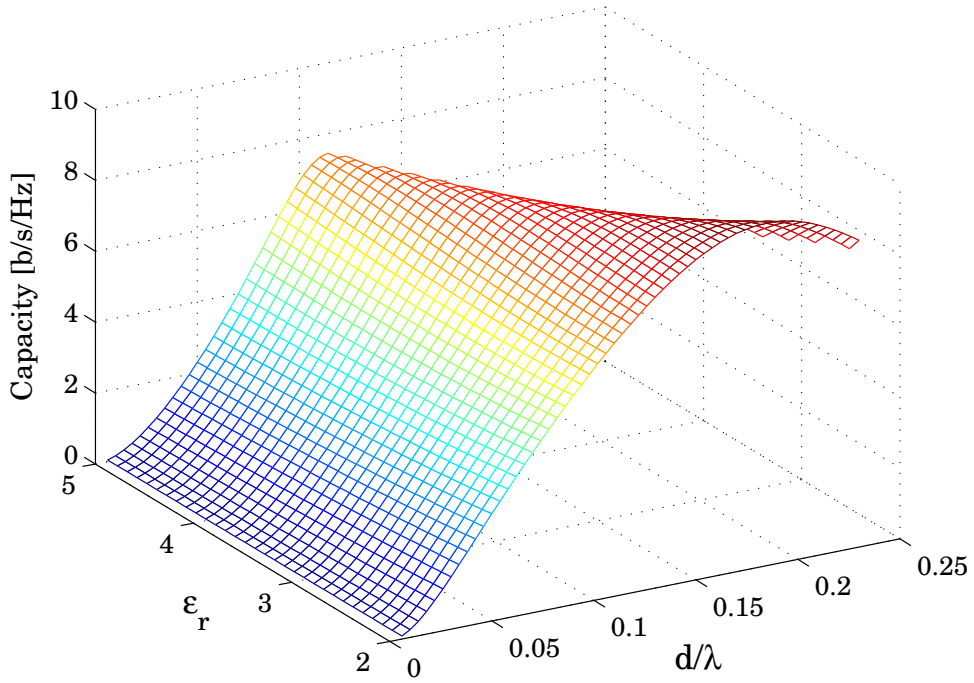

Figure 3.8: Capacity versus dielectric thickness and permittivity for printed arrays with 3 side-by-side dipoles.

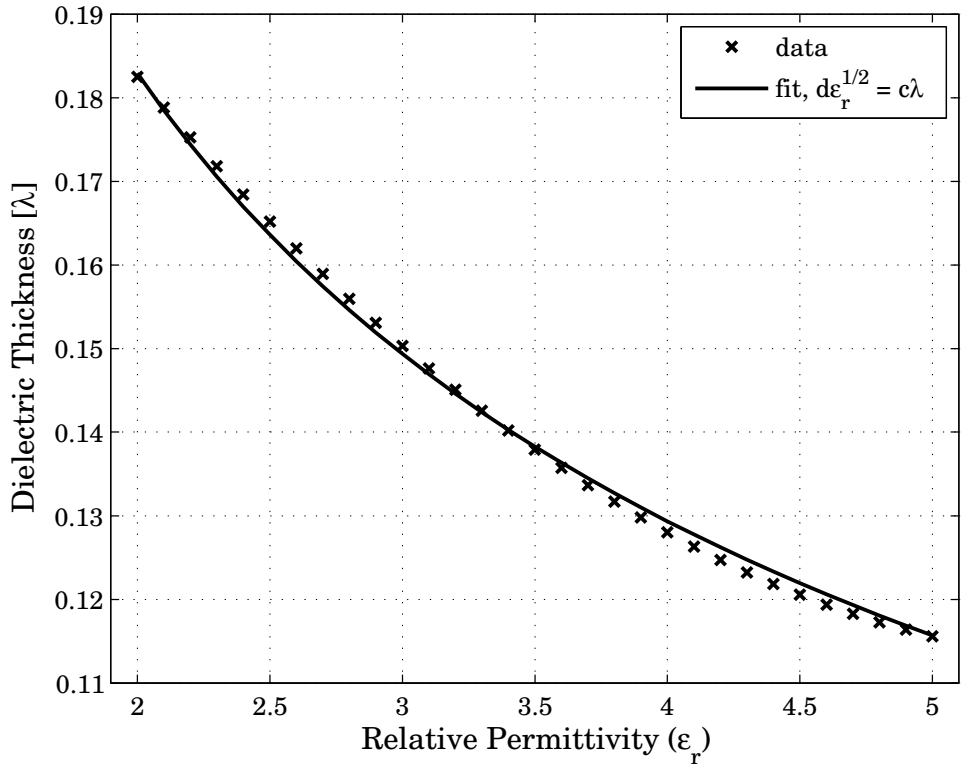

Figure 3.9: Dielectric thickness and permittivity configurations yielding maximum capacity.

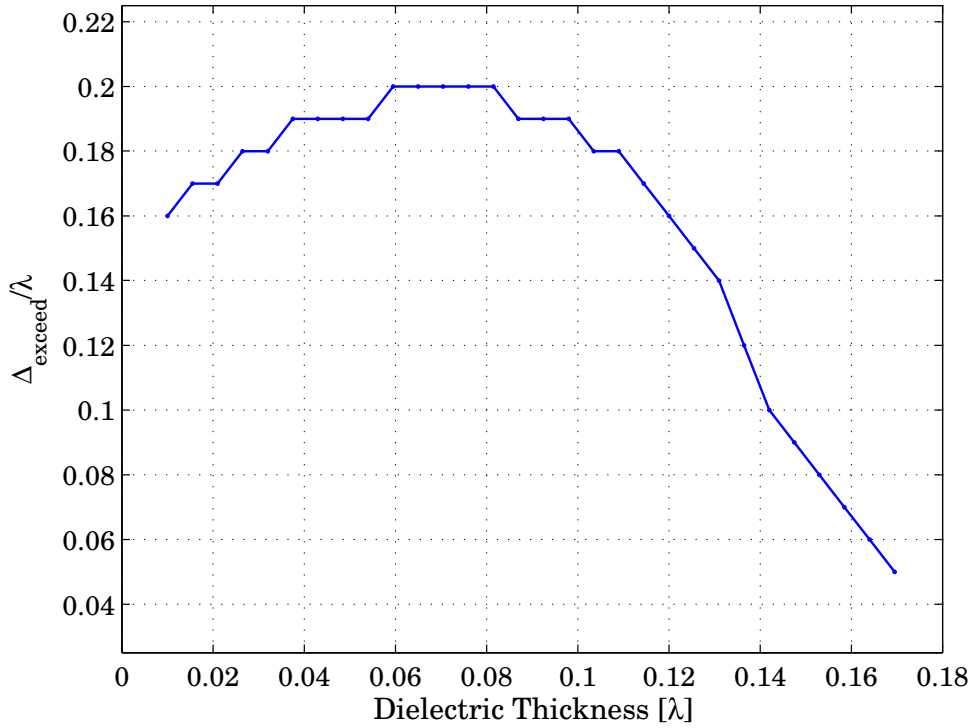

Figure 3.10: The interelement spacing required to exceed the SIMO capacity for printed dipoles, Δ_{exceed}, versus dielectric thickness, d.

MIMO capacity. Furthermore, coupling between printed dipoles through surface waves is shown to have no significant effect on the channel capacity.

Effects of the electrical properties of printed dipoles on the MIMO capacity are explored in terms of the relative permittivity and thickness of the dielectric material. Appropriate dielectric slab configurations yielding high capacity printed dipole arrays are presented.

It should be mentioned that, efficiency of the proposed MEF algorithm is governed by the evaluation of the interactions, in particular in the case of printed arrays, and the inversion time of the MoM impedance matrix. However, considering the fact that typical MIMO systems do not contain thousands of antennas at the transmitter and receiver sides, inversion time of the MoM matrix is fast and the efficiency of MEF strongly depends on the calculation of self and mutual interactions (especially the case for printed arrays). Because we use different Green's function representations for printed arrays in the MoM procedure in

a computationally optimized manner (based on the distance between antenna elements) [82–84, 86], the proposed MEF yields accurate results within seconds.

Chapter 4

Particle Swarm Optimization of Dipole Arrays for Superior MIMO Capacity

Even though MIMO offers high channel capacity in a limited bandwidth, some work still needs to be done to achieve that. To acquire the superior capacity out of a MIMO channel, the choice of array type and configuration at the transmitter (TX) and receiver (RX) is a fundamental design issue. Foreseeing that MIMO communication systems will be everywhere in near future, it is envisioned that capability of designing these systems with optimum channel capacities will be handy. For a classic MIMO system in which the transmitter and/or receiver antennas are placed in a specified volume, it is important to determine the individual antenna lengths and locations together with number of elements used. For instance, uniform linear arrays (ULA) are intensely studied for MIMO systems, however, the question of whether non-uniform linear arrays are able to outperform ULA in terms of their capacity was unanswered. Furthermore, for an adaptive MIMO system, deciding which elements to activate or how

to terminate the parasitic elements such that the channel capacity is maximized are significant issues.

Aforementioned optimization may be accomplished when a MIMO channel model, which has the ability of simulating real world cases, is armed with an optimization algorithm. Particle swarm optimization (PSO), a popular and yet evolving powerful optimization algorithm inspired by the swarm behavior [81], can be employed for this purpose. PSO is proven to be fast, efficient and capable of solving a vast variety of complex computational electromagnetics (EM) problems. It should be stressed that, an antenna optimization problem which aims to maximize the channel capacity provides a more natural approach for antenna synthesis, since it maximizes the quantity of true interest in any communication system. The introduction of information theoretical cost functions in the design of antennas turns out to be a promising approach [72].

Simulating real world cases is a vital issue for the accuracy and reliability of the designs but this is hard to accomplish. The models used to simulate the behavior of MIMO channels can yield accurate and reliable results only if they are well tested and experimentally verified. Hence, throughout this study our channel model with electric fields (MEF) is utilized. Since the technique is computationally efficient, MEF allows analyzing MIMO performance of arrays with large number of dipole elements, and high performance arrays can be designed using a combination of MEF and optimization techniques.

In this chapter, MEF is combined with PSO, in order to design dipole arrays with superior MIMO capacity. First, the accuracy and numerical efficiency of PSO is demonstrated on a sample scenario. For this purpose, a predefined problem is solved first in a brute force manner and then with PSO. As PSO succeeds in solving the problem with great efficiency, MEF with PSO is benchmarked with genetic algorithm (GA) based simulations and measurements of [72]. In [72], Migliore *et al.* designed an adaptive MIMO antenna system using GA

and measured its channel capacity under various test conditions. MEF with PSO is employed to solve the same setup in [72], and it is observed that the results match with the simulations and measurements demonstrating the ability of both MEF and PSO in designing MIMO systems. Then, examples of MIMO system designs of freestanding and printed dipoles are introduced. Uniform circular arrays (UCA) of freestanding dipoles are shown to be a reasonable choice for high MIMO capacity, though results for other array configurations outperforming UCAs are given. Adaptive MIMO array performance of printed dipole arrays with loaded parasitic elements is investigated and compared with that of freestanding dipole arrays.

4.1 MIMO Channel Model

In this chapter, as the scattering environment, two different three dimensional (3D), single-bounce geometric models are considered. As the capacity of the system, the achievable data rate in (2.2) is used as well. Following the MEF procedure that is given in the previous chapters, the channel matrix is evaluated accurately and efficiently both for freestanding dipole arrays and printed ones.

4.2 Particle Swarm Optimization

Particle swarm optimization (PSO) is a population based stochastic optimization technique inspired by the social behavior of bee swarming or bird flocking. In PSO, the swarm is initialized with a random population, namely particles. Particles search for optimum solution by flying through the problem space by following the current optimum particles. Each particle keeps track of its coordinates in the problem space and associates the position with the *personal* best solution, p_{best}, it has achieved so far. Another best value that is tracked by the

particle swarm optimizer is the best value obtained so far by any particle in the swarm and is called the *global* best, g_{best}.

In past several years, PSO has been successfully applied in many electromagnetic problems. It is demonstrated that PSO gets better results in an easier and faster way compared to other methods. The particle swarm optimization concept requires, at each time step, accelerating each particle toward its p_{best} and g_{best} locations. Acceleration is weighted by a random term, with separate random numbers being generated for acceleration toward p_{best} and g_{best} locations as,

$$x_{n,t+1} = x_{n,t} + v_{n,t}\ \Delta t \tag{4.1}$$

$$v_{n,t+1} = K\left[v_{n,t} + \varphi_1\ \mathcal{U}(0,1)\ (p_{best_{n,t}} - x_{n,t}) + \varphi_2\ \mathcal{U}(0,1)\ (g_{best_{n,t}} - x_{n,t})\right] \tag{4.2}$$

where $x_{n,t}$ and $v_{n,t}$ are the particle's position and velocity in the nth dimension at instant t, Δt is the time step which is chosen to be one, K is the constriction factor, $\mathcal{U}$ is drawn from the uniform distribution on the unit interval $(0, 1]$, finally φ_1 and φ_2 are the scaling factors that determine the relative pull of p_{best} and g_{best} of the particles, respectively. As stated and analyzed in [81], the optimal selection of constants mentioned above necessitates the choice of K to be 0.729, φ_1 to be 2.8 and φ_2 to be 1.3, thus removing the need for setting a maximum velocity limit.

Occasionally, particles pass beyond the boundaries of given solution space, hence adoption of a boundary policy to the algorithm is essential [89]. In order to enforce particles to search inside the solution space of interest, damping wall and invisible wall techniques suit our applications best and therefore are used in this study. In the damping wall technique, when a particle attempts to search outside the allowable solution space in one of the dimensions, it is relocated at the boundary of the solution space and the velocity component in that dimension is changed in the opposite direction and multiplied with a random factor between zero and one. In the invisible wall technique, particles are allowed to fly outside the allowable solution space in one of the dimensions, but assigned zero fitness

values. Eventually, the particles are expected to return to the solution space since fitness values (i.e., the capacity values evaluated for cases represented by each particle) are larger inside the allowed space.

4.3 Numerical Results

We start by assessing the speed, accuracy and computational cost of the PSO implementation. Next, we check the validity of the channel model that we used. Finally, results for sample MIMO wireless system designs with arrays of freestanding and printed dipoles are given.

We first solve a predefined problem in a brute force manner, i.e., without employing PSO. The mission is to obtain the highest possible channel capacity by using a two element fixed separation (i.e., $\Delta = 0.61\lambda$) varying length (i.e., from $L = 0.01\lambda$ to $L = 1\lambda$ with 0.01λ increments yielding 100 different lengths for each antenna) freestanding linear dipole array (FSLA) at the transmitter. The problem is to find the optimum individual element lengths of this transmitting FSLA. On the other hand, the receiver array is assumed to be fixed, i.e., an FSLA located 300λ away from the transmitter in a broadside manner, formed by $R = 10$ uniform linear dipoles each of which is separated by a distance of $\lambda/2$. Elements of both TX and RX array have a radius of $\lambda/200$ and are matched to 50Ω source and load impedances, respectively. Transmit SNR of the array is assumed to be fixed. The channel is modeled by locating $S = 100$ uniformly distributed scatterers around the transmitter within a spherical region (i.e., in the far zone of the transmitter) and the capacity results are obtained by simulating $N_R = 1000$ channel realizations.

Result of the brute force solution is presented in Figure 4.1 (a) which depicts that the highest capacity is achieved when lengths of two elements are equal to 0.46λ. Afterwards, PSO is applied to the abovementioned problem, and it

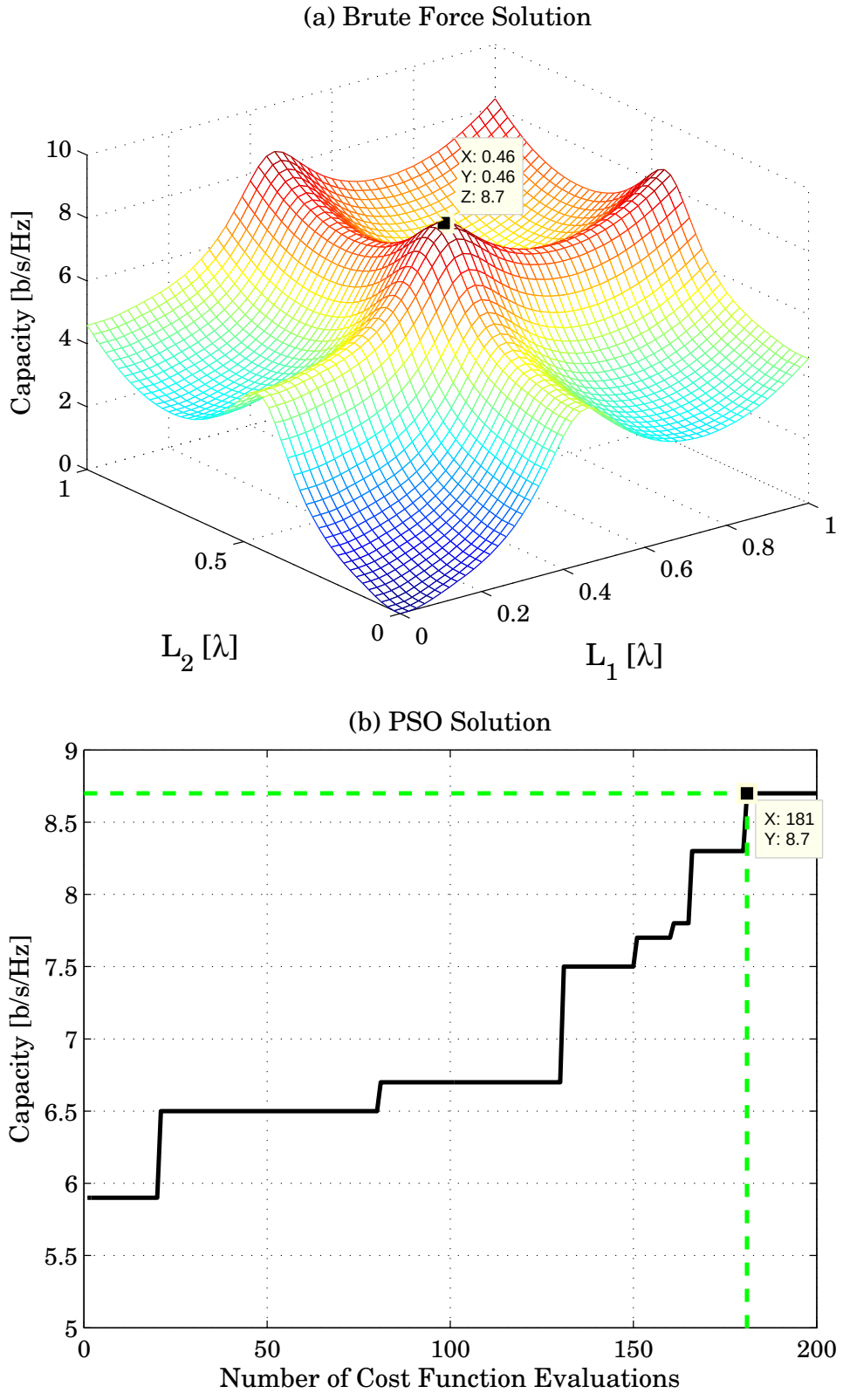

Figure 4.1: Numerical validation of PSO. (a) Brute force solution with 10 000 cost function evaluations. (b) PSO solution yields the optimum configuration ($L_1 = 0.46\lambda$, $L_2 = 0.46\lambda$) with the maximum capacity (8.7 b/s/Hz) in 181 cost function evaluations.

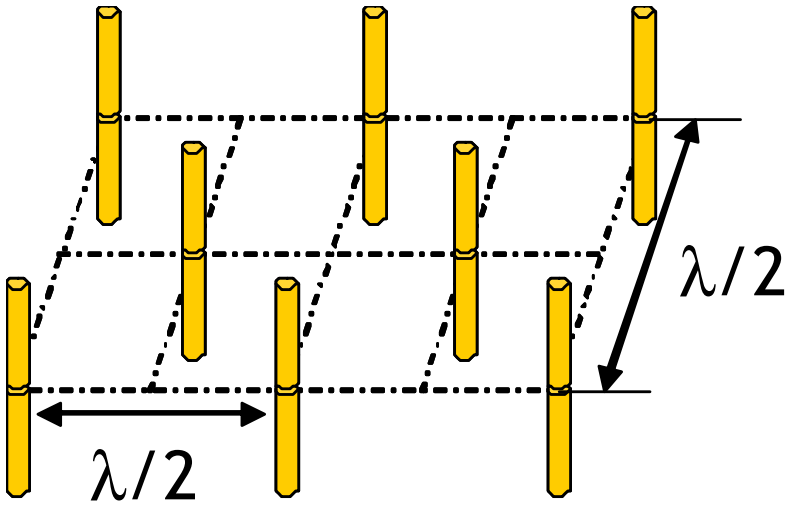

Figure 4.2: The geometry of adaptive MIMO array of FS dipoles.

is observed that the result of PSO coincides with that of brute force solution as depicted in Figure 4.1 (b). Investigating Figure 4.1 (a) and (b), it is noted that the brute force solution requires $100^2 = 10000$ cost (capacity) function evaluations (since the element length for each antenna is quantized into 100 possible values) whereas PSO has completed it in less than 200 evaluations. This computational test proves the efficiency and accuracy of PSO in solving this sort of computational EM problems.

Second step of the validation of our implementation is to check how accurately MEF models the MIMO channel. This step utilizes experimental measurements under real life conditions. For this purpose, the work done in [72] is used. In [72], Migliore *et al.* fabricated an Adaptive MIMO (AdaM) system of identical transmitter and receiver of freestanding (FS) dipole arrays with two active elements surrounded by six parasitic elements. The geometry of the AdaM system used is rather simple as shown in Figure 4.2. $\lambda/2$ length thin-wire dipole antennas were placed in a rectangular lattice of 2×4 square grids with edge length $\lambda/4$. Active elements were placed in the middle of the lattice and were $\lambda/2$ apart from each other. On the other hand, the parasitic elements were placed to surround the lattice. Active elements were terminated in 50Ω dummy loads and parasitic

elements were connected to microelectromechanical systems (MEMS) switches with impedances $Z_{on} = 76.6 - j426\Omega$ and $Z_{off} = 5.2 - j8.8\Omega$. Every antenna element was placed at a height of one meter from the floor. The measurements were made in a common office room of 8 meters width and 3 meters height and length. The measurement method was to measure each element of the channel matrix $\mathbf{H}$ separately by employing a vector network analyzer. The transmitted SNR was selected so as to achieve a channel capacity of 4 bits/s/Hz solely with active antennas and the performance of AdaM system were evaluated with this transmitted SNR throughout the measurements.

In this work, MEF with PSO is configured to simulate the aforementioned measurement environment and employed to find the optimal channel capacity that can be achieved. When modeling the office room in which measurements were made, a scattering scenario of uniformly distributed 20 point scatterers is considered. The capacity results of AdaM are obtained by averaging the MIMO channel capacity over 1000 different channel realizations. Remaining parameters are set to be the same as those of measurements of [72]. Under these conditions, termination impedances of parasitic elements are altered to achieve the optimal channel capacity, i.e., simulate the experiment done in [72]. The results of MEF with PSO are depicted in Figure 4.3 [represented by MEF with PSO (FS)] along with the measurement and GA simulation results of [72], and they are all in very good agreement which proves the validity and accuracy of MEF in modeling MIMO channels. Figure 4.3 also shows that, for small number of cost function evaluations, PSO can reach higher capacity values than GA does; though after 80 evaluations, two optimization algorithms lead to approximately the same results. At this point, both MEF and PSO are proven to be reliable, accurate and efficient thus validating its use in MIMO system design. From now on, we may utilize them to design sample MIMO arrays for superior channel capacity.

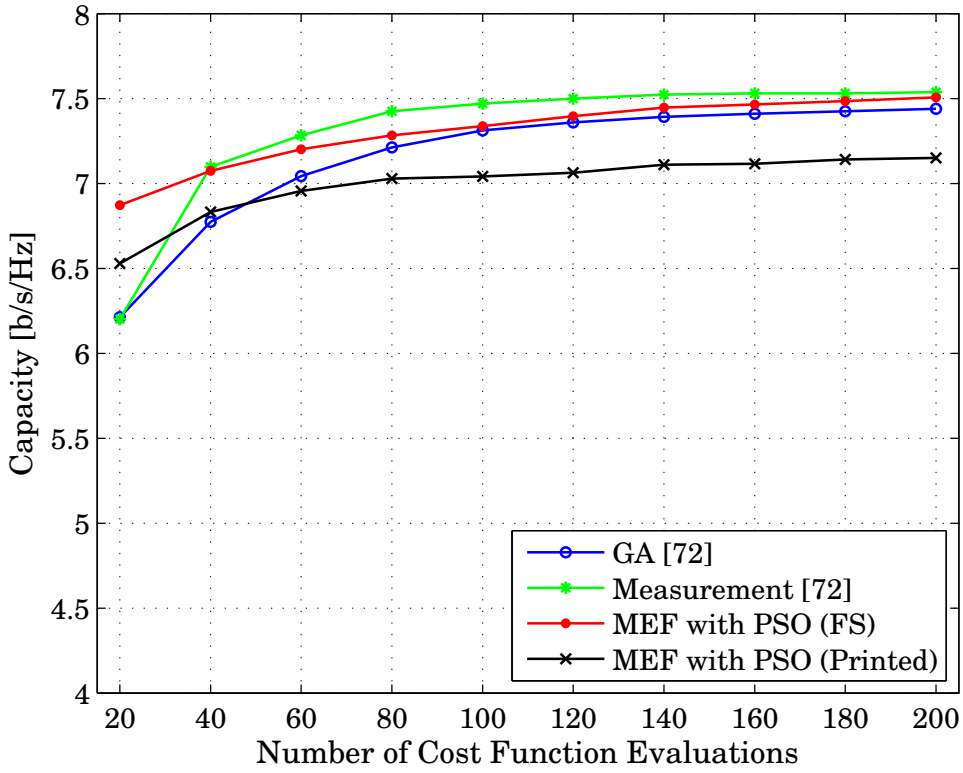

Figure 4.3: Validation of MEF+PSO with both GA simulations and measurements of [72] for freestanding adaptive dipoles; and comparison of adaptive performance of printed dipoles obtained by MEF+PSO.

Uniform circular arrays (UCA) are among the most popular arrays that antenna engineers use in their designs. It is interesting to investigate whether other geometries can bring significant gains over them. For this purpose, we consider a volume of $\lambda \times \lambda \times \lambda$ in which the varying number of antenna elements are going to be placed. In this volume, we employ MEF with PSO to find a better MIMO design than $\lambda/2$ length UCA. As a first step, we seek for an improvement over the circularity of uniform arrays, that is to say we look for optimum locations rather than playing with the individual lengths of antennas which are set to be the same as UCA (2D case). In the second step, we set PSO (3D case) completely free to change both the locations and the lengths of every individual element in the array. The geometry and environment that is used in this part of the work is exactly the same to the one used to prove the validity of PSO.

Since UCA is known to be a good antenna engineering solution and an improvement over UCA is sought, one PSO particle is smartly initialized with a UCA design. This saved us from doing many fitness evaluations since with full random initialization PSO could first reach the UCA configuration and then try to improve that. Since we are looking for an improvement over circularity in this stage of our work, we fix the element lengths to 0.5λ, i.e. PSO only varies the positions of array elements in a 2D space which is in fact a square of area λ^2. The improvement over UCA is plotted in Figure 4.4 (a). Figure 4.4 (a) also shows that the designs are made in less than 700 evaluations for a solution space of order 100^{2T}, i.e. $O(100^{2T})$, where each solution dimension (i.e., x and y which are the phase center coordinates) has a size of 100 per each TX element.

In the 2D case, PSO finds the locations of antennas (in terms of wavelength) as the optimum on a xy-plane of 100^2 grid points. As is obvious from Figure 4.4 (a), for the plane we used PSO can find better results than UCA provided that T does not exceed six. However if it is more than that, PSO agrees that UCA is the best solution. Figure 4.5 (a) shows the geometry, which is not a circular one, of the six element TX designed by PSO and Figure 4.5 (b) shows the geometry, which is a circular one, of the seven element TX which is also designed by PSO.

As just mentioned and also illustrated in Figure 4.4 (a), in the geometry we consider, PSO cannot improve UCA confidently when TX is a seven or more element antenna array. This is the case since with the increase in the number of TX elements used, due to physical limitations, elements are forced to be placed closely which results in the generation of considerable amount of mutual coupling. Therefore to achieve the optimum interelement spacing, elements of the TX array are spaced in a circular fashion when T exceeds six. This yields us to conclude that although there are improvements over circularity of uniform arrays, UCA is still a good design option since improvements are comparatively small for this λ^2 geometry.

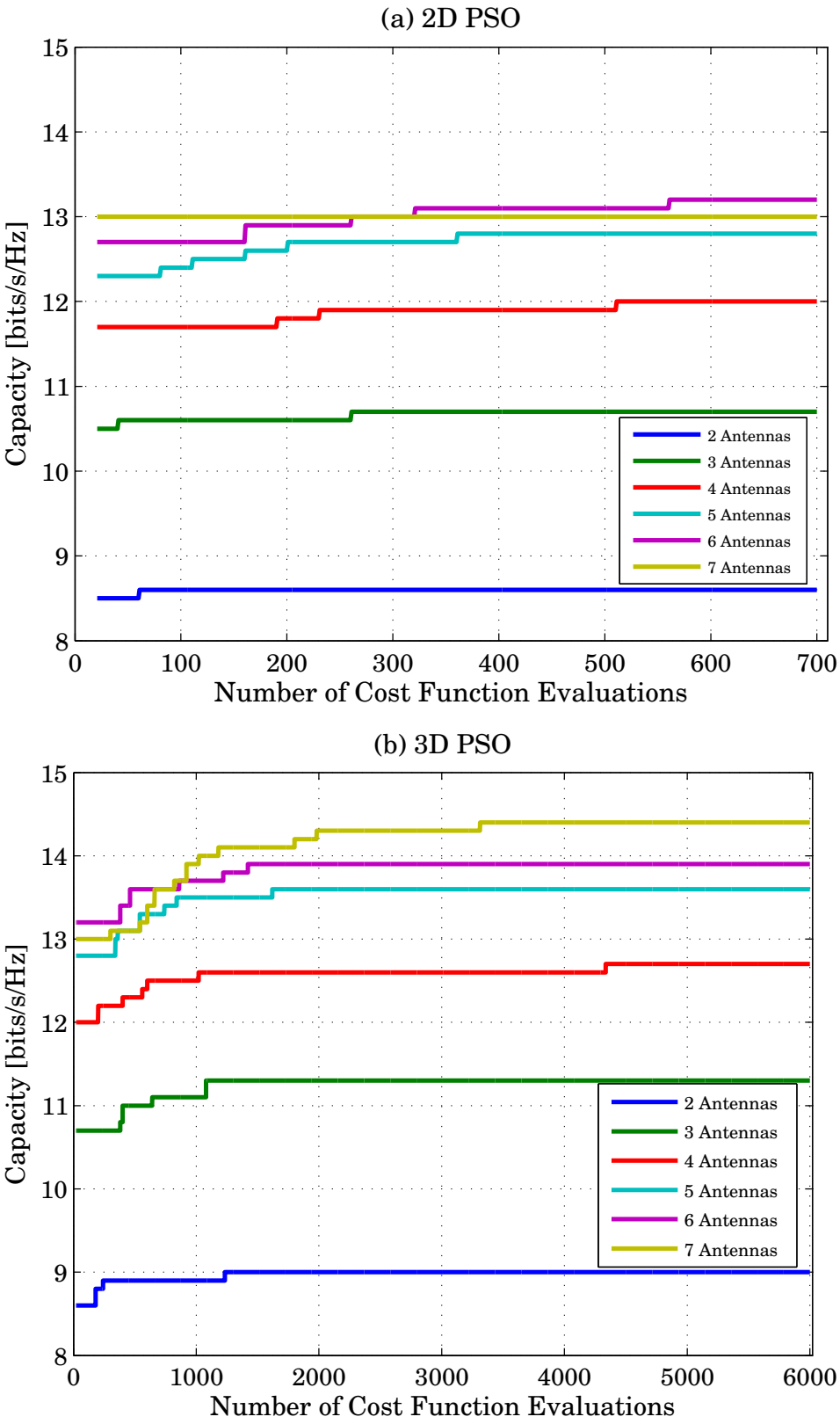

Figure 4.4: Capacity improvement over UCA for (a) 2D (b) 3D PSO optimization.

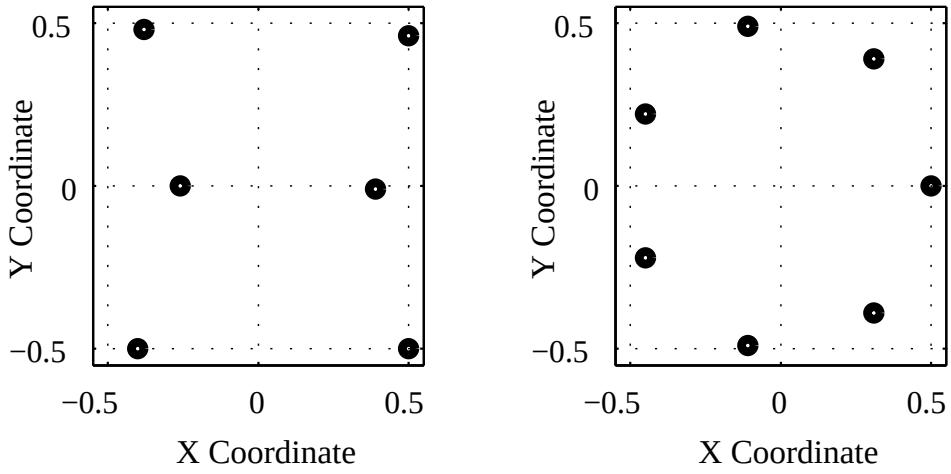

(a) 6 Antennas (b) 7 Antennas

Figure 4.5: Top view geometries of sample designs made by 2D PSO.

T	$\mathcal{C}_{uca}$	$\mathcal{C}_{3D}$	$x(\lambda)$	$y(\lambda)$	$z(\lambda)$	$L(\lambda)$
2	8.5	9.0	0.45	0.47	−0.265	0.47
			−0.5	−0.15	0.265	0.47
3	10.5	11.3	0.27	−0.05	0.27	0.46
			0.15	0.5	−0.265	0.47
			−0.32	−0.5	0.22	0.46
4	11.7	12.7	0.31	−0.07	0.01	0.46
			0.26	0.5	−0.265	0.47
			−0.42	−0.5	0.4	0.46
			0.5	−0.5	0.27	0.46
5	12.3	13.7	0.37	−0.13	0.265	0.47
			0.31	0.5	0.05	0.46
			−0.5	0.5	−0.09	0.46
			−0.39	−0.5	−0.05	0.46
			0.5	−0.5	0.03	0.46
6	12.7	14.0	0.48	0.3	−0.035	0.47
			0.5	0.5	0	0.46
			−0.33	0.48	0.06	0.46
			−0.28	0.04	0.05	0.46
			−0.5	−0.5	0.005	0.47
			0.48	−0.5	−0.005	0.47
7	13.0	14.3	0.44	−0.07	−0.02	0.46
			0.44	0.46	0	0.46
			−0.37	0.5	−0.005	0.45
			−0.42	0.14	0.005	0.45
			−0.49	−0.28	−0.27	0.46
			−0.47	−0.5	0.04	0.46
			0.44	−0.49	−0.05	0.46

Table 4.1: Optimum TX locations for 3D PSO optimization

Thereafter, we modify the PSO so as to include the lengths of TX elements into its variable basket. In other words, PSO is now employed to make a 3D design in the cube mentioned at the beginning of this section. Our modified PSO is now powered with the capability of analyzing arrays in nonstaggered, staggered and collinear arrangement. In order to sustain our smart tradition, we initialize one of our particles with the final designs made by PSO in 2D space while another one still starts with a UCA. Remaining particles are released randomly to the solution space of $O(100^{4T})$ where each solution dimension (i.e., x, y, z and L where the first three are the phase center coordinates and L is the length) has a size of 100 per each TX element.

Table 4.1 reviews the mean capacity obtained from the UCA and introduces the one obtained from 3D PSO along with the optimum phase center location and length for each element in the array. 3D PSO changed the xy locations of phase centers of its 2D counterpart as well as changing the element lengths to achieve more capacity. This improvement over 2D PSO is plotted in Figure 4.4 (b).

As mentioned in 2D PSO, we are unable to find a better solution than UCA for seven element TX. On the other hand, the design by 3D PSO has managed to outperform UCA because of its ability to place elements in staggered or collinear arrangements. Figure 4.6 depicts the design made by PSO for seven element TX where elements are seen to be arranged as mentioned before. It should be noted for the Figure 4.6 (c) that since the x coordinate of the phase centers of three elements are the same, it is seen as if there are five elements placed although there are seven. Figure 4.7 shows that as the number of elements in the TX array increases while keeping the volume constant, the capacity increases until a point. It also suggests that UCA is still a good solution and even the best one when the volume is relatively small or the array gets larger.

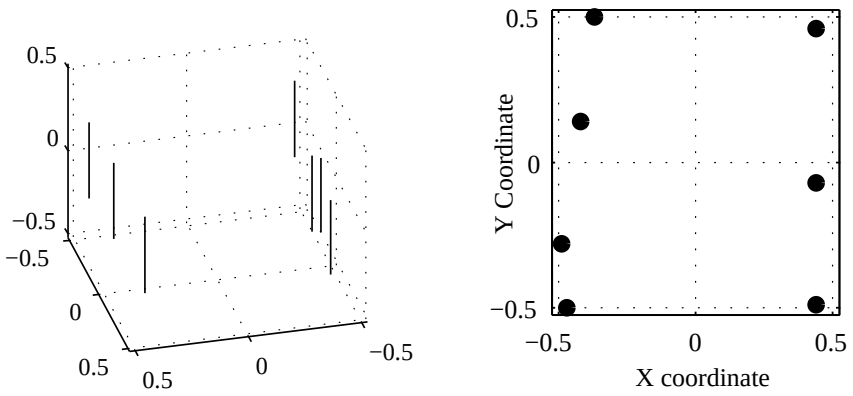

(a) 3D view (b) Top view

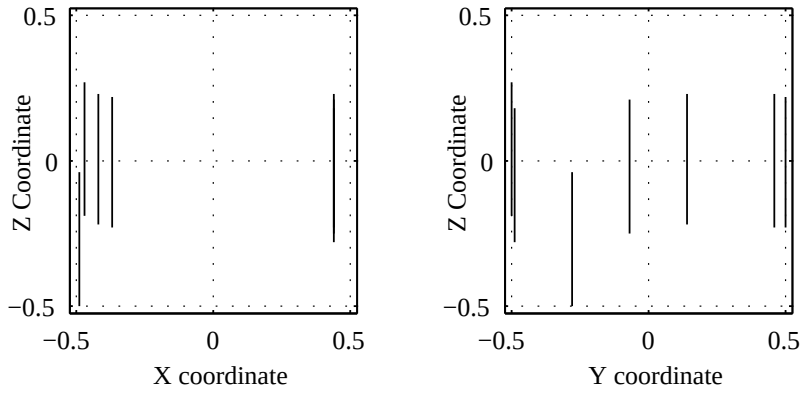

(c) xz-view (d) yz-view

Figure 4.6: Geometry of 7 element TX designed by 3D PSO.

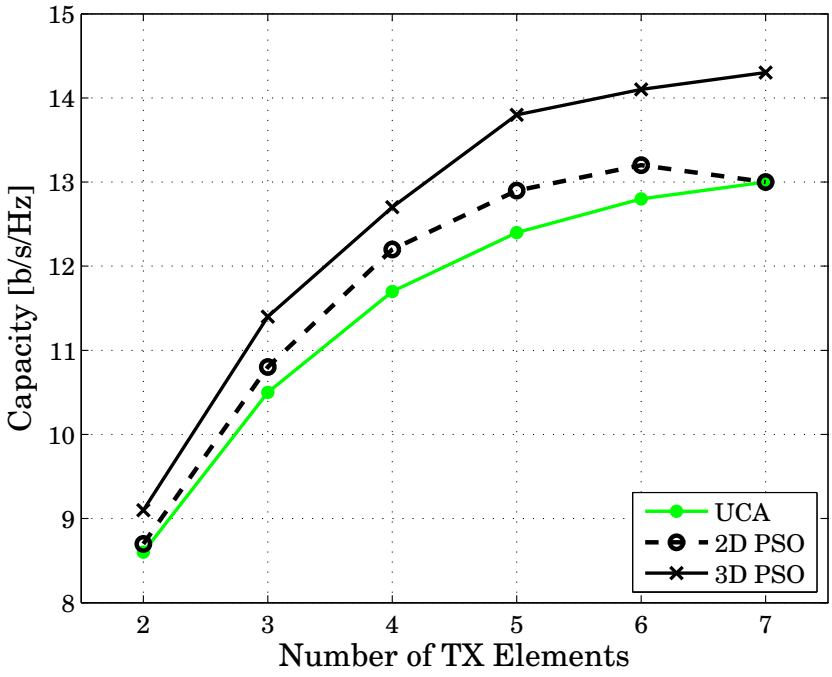

Figure 4.7: Capacity results obtained by PSO for freestanding dipoles in a λ^2 area (2D), and a λ^3 volume (3D). Comparison with uniform circular arrays (UCA).

Up to this point, only FS dipoles have been taken into account in all of our MIMO array designs. Thus, as the next step MEF with PSO is used to investigate printed dipoles for superior channel capacity. An adaptive MIMO system of a printed TX array is optimized by expanding the work of [72] to printed dipoles. The scenario, geometry and environment used in this new design are very similar to the ones in [72]. The main difference between them is, as expected, the geometry of the new TX, which is depicted in Figure 4.8. The dielectric slab on the ground plane is assumed to have a thickness of $d = 0.1\lambda$ and a relative permittivity of $\epsilon_r = 3$. The length of the dipoles is chosen as $l = \lambda_e/2$, where $\lambda_e = \lambda/\sqrt{0.5(\epsilon_r + 1)}$ is the effective wavelength due to the dielectric material; whereas their widths are considered to be $\lambda/100$. The other difference from [72] is about the termination impedances of the TX elements. For the sake of a fair comparison (i.e., to eliminate the effects of antenna impedance mismatch between printed and FS dipoles), the termination impedance of the printed dipole is matched to that of the FS one, and then connected to the MEMS switch mentioned before.

Figure 4.3 also depicts the MIMO channel capacity performance of printed adaptive TX array, represented by PSO with MEF (Printed). As the figure suggests, the performance of FS dipoles is slightly better than the printed case. For in depth investigation, solutions for all 4096 (2^{12}) possible terminations (since we have a total of 12 parasitic elements and each of them can be either "on" or "off") are obtained for both cases. The histograms of channel capacities for all possible solutions are given in Figure 4.9 (a) for FS dipoles and (b) for printed ones. As can be seen from Figure 4.9, the maximum capacity for the FS adaptive array is larger than that of the printed adaptive array. The reason behind this result can be understood by inspecting the radiation patterns of single FS and printed dipoles in Figure 4.10 (note that both dipoles are x-directed). Figure 4.10 (b) suggests that, the radiation pattern of FS dipole on azimuth plane is isotropic whereas the one for printed dipole is curved due to the dielectric

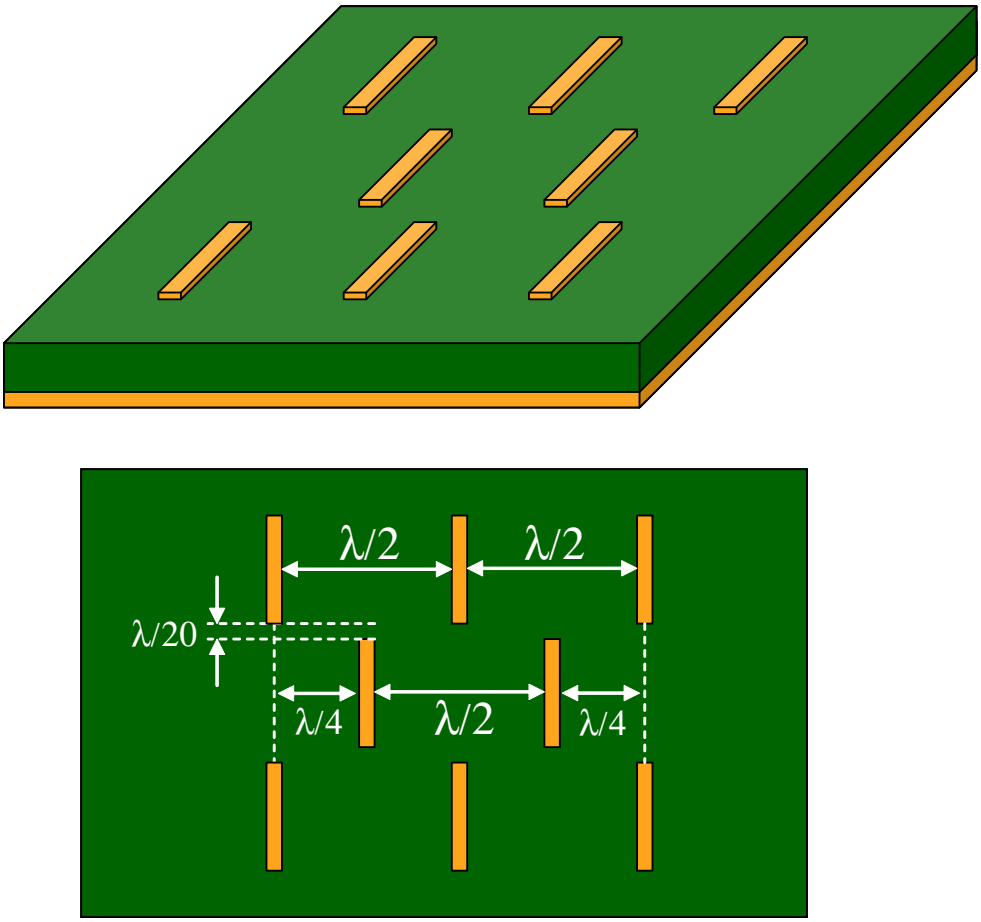

Figure 4.8: Printed array geometry.

slab on the ground plane, leading to less radiated power under fixed transmit SNR. However, as Figure 4.9 suggests, the printed dipoles can be said to be less sensitive to the termination impedances based on the used MEMS switches in comparison with FS ones, since the minimum capacity of printed adaptive array is significantly larger than that of FS one; due to the fact that FS array elements are more mutually coupled than the printed ones for the configurations considered here. In the FS adaptive array, all elements are designed to be located at the maximum radiation direction of each other; and hence, FS array configuration given in [72] and this work suffers more from mutual coupling than the printed one does.

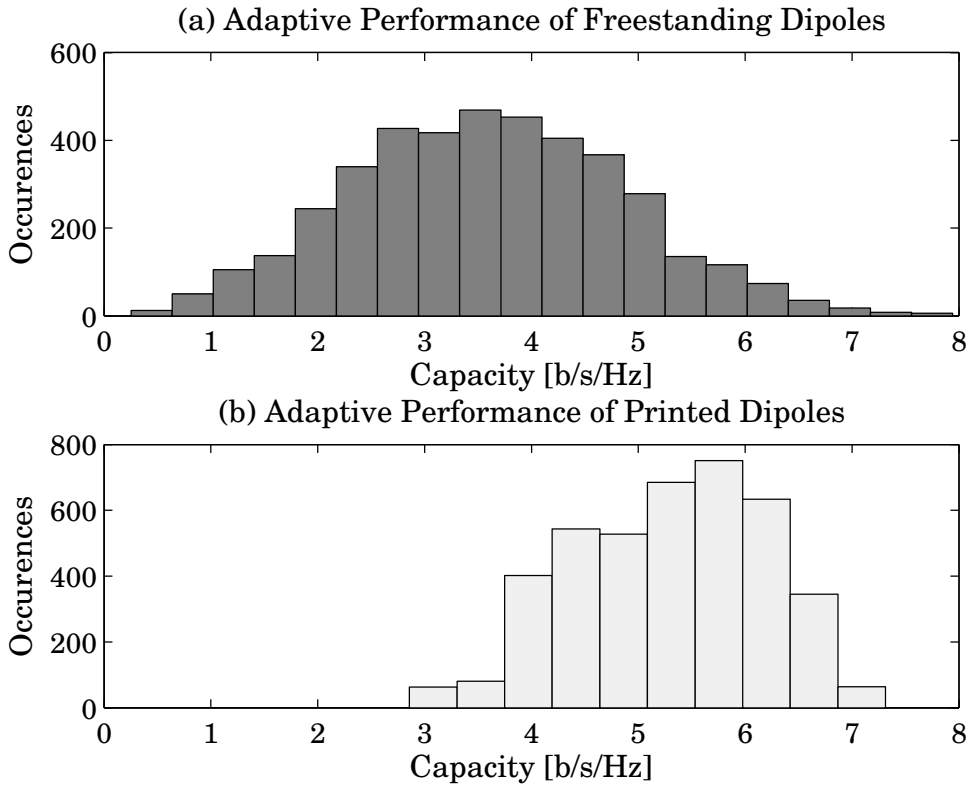

Figure 4.9: MIMO performance of adaptive arrays for all possible termination impedances. (a) Freestanding dipoles. (b) Printed dipoles.

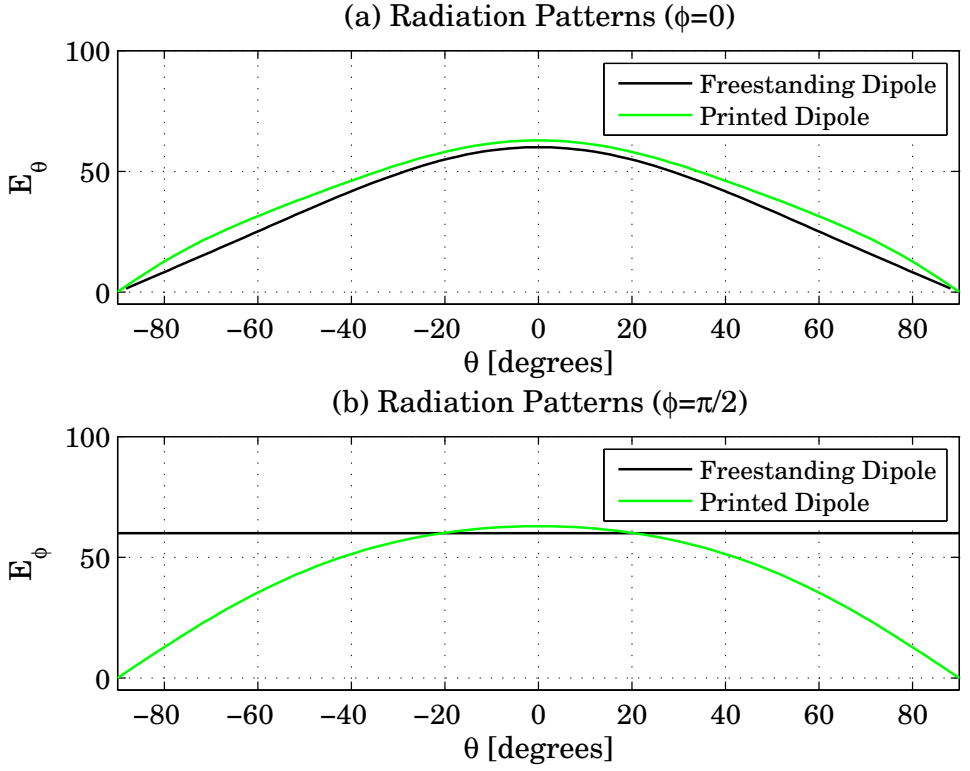

Figure 4.10: Radiation patterns of x-directed freestanding and printed dipoles.

4.4 Conclusions

The channel model with electric fields is combined with particle swarm optimization to design MIMO arrays of dipole elements for superior capacity. Validation of both the channel model and PSO is done by comparing the results with measurements and GA simulations. Freestanding and printed dipole arrays are analyzed and optimized.

FS dipole arrays are designed for high MIMO performance by optimizing the number of antenna elements, their individual locations and lengths, in a physically limited volume. It is shown that, the use of UCA is a reasonable choice for high capacity, even though results for other array configurations outperforming UCA are given as well.

The work of [72] is expanded to printed dipole arrays, and their adaptive performance in the MIMO channel is investigated. Adaptive printed dipoles are shown to be good alternatives to FS ones, due to less mutual coupling; though their reduced radiated power under fixed transmit SNR leads to slightly decreased MIMO capacity.

Chapter 5

Capacity of Printed Planar Rectangular Patch Antenna Arrays in the MIMO Channel

5.1 Introduction

Microstrip patch antennas have gained immense popularity in microwave communications applications owing to their conformal, lightweight and low cost nature. Since their invention, microstrip patch antennas have been employed heavily for military applications like airborne, guided missile and spacecraft systems. Due to the recent decline of the dielectric substrate prices, the utilization of microstrip antennas by the commercial communication applications have also been boosted.

Microstrip patch antennas have built their popularity on their inherent ability to have polarization diversity and their ease of fabrication. A microstrip patch antenna can be easily designed to have any desired polarization and can be easily

fabricated by etching the antenna element from the metal that bonds the dielectric substrate. With very little additional cost, patch antennas can be fabricated as antenna arrays which allows achieving very high gain while preserving the lightweight and planar nature of the antenna. Considering these splendid features of microstrip patch antennas, their performance in MIMO systems seems very promising but has yet to be investigated. Popular microstrip radiator shapes include square, rectangular and circular but any continuous shape will do the job.

In this study, rectangular patches fed by a probe are chosen over others since the input impedance of the probe-fed rectangular patch can be controlled easily. Several probe-fed rectangular microstrip patches are fabricated and employed in a MIMO wireless communication system. The performance of different patch antenna arrays in terms of MIMO channel capacity is obtained by measurements and compared with each other, as well as the numerical results of a modified version of the developed channel model with electric fields (MEF).

5.2 Wireless Channel Measurement Using Vector Network Analyzer

Let us consider the wireless communication system with single antennas at the transmitter and receiver sides as illustrated in Figure 5.1. Using network analysis, the total port voltages and currents at the terminal planes for the transmitter (port 1) and the receiver ports (port 2) can be written as

$$V_n = (a_n + b_n)\sqrt{Z_{in,n}} \tag{5.1}$$

$$I_n = \frac{a_n - b_n}{\sqrt{Z_{in,n}}} \tag{5.2}$$

where $n = 1, 2$; $Z_{in,n}$ is the input impedance seen through the port, a_n represents an incident wave at the nth port, and b_n represents a reflected wave from that port. These in and outward propagating waves are related to each other via the

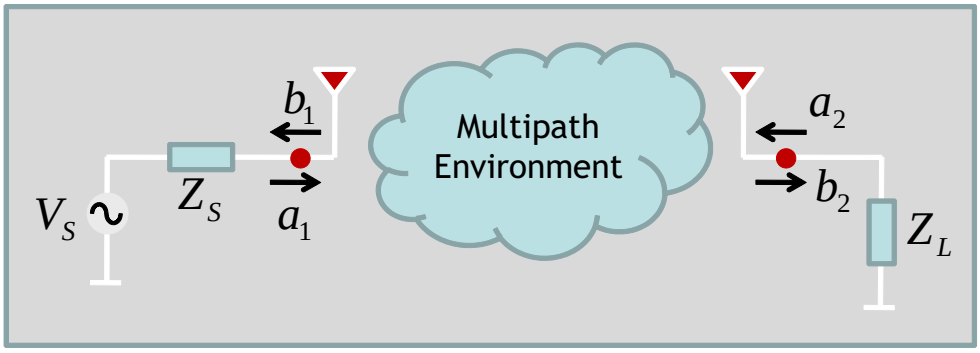

Figure 5.1: SISO wireless communication system.

scatterer (S) parameters such that

$$\bar{b} = \mathbf{S}\ \bar{a} \tag{5.3}$$

$$\begin{bmatrix} b_1 \\ b_2 \end{bmatrix} = \begin{bmatrix} s_{11} & s_{12} \\ s_{21} & s_{22} \end{bmatrix} \begin{bmatrix} a_1 \\ a_2 \end{bmatrix}. \tag{5.4}$$

Then, the voltage and the current at the transmitter antenna port become

$$V_1 = (a_1 + s_{11}a_1 + s_{12}a_2)\sqrt{Z_{in,1}} \tag{5.5}$$

$$I_1 = \frac{a_1 - s_{11}a_1 - s_{12}a_2}{\sqrt{Z_{in,1}}}. \tag{5.6}$$

The source voltage (V_S) can be expressed in terms of the source impedance (Z_S), the port voltage and current by

$$V_S = V_1 + I_1 Z_S. \tag{5.7}$$

If the input impedance of the transmit antenna is matched to the source impedance such that $Z_{in,1} = Z_S$, (5.7) turns out to be

$$V_S = 2a_1\sqrt{Z_{in,1}}. \tag{5.8}$$

Similarly, when the input impedance of the receiver antenna is matched to the load impedance, i.e., $Z_{in,2} = Z_L$, the following relations are valid:

$$V_2 = (a_2 + b_2)\sqrt{Z_{in,2}} = -I_2 Z_L \tag{5.9}$$

$$= -(a_2 - b_2)\sqrt{Z_{in,2}}. \tag{5.10}$$

The equality of (5.9) with (5.10) yields

$$a_2 = 0 \tag{5.11}$$

and

$$V_L = b_2\sqrt{Z_{in,2}}. \tag{5.12}$$

Assuming $Z_S = Z_L$, the channel response defined from the source voltage to the load voltage can be expressed as,

$$h = \frac{V_L}{V_S} = \frac{1}{2}\frac{b_2}{a_1}, \tag{5.13}$$

which becomes

$$h = \frac{s_{21}}{2} \tag{5.14}$$

since $a_2 = 0$.

Namely, if the input impedances of the transmitter and receiver antennas are matched ($Z_{in,1} = Z_{in,2} = Z_S = Z_L$), measuring s_{21} of such a communication system with the use of a 2-port vector network analyzer (VNA) will give twice the channel response, since the impedances seen through the ports are usually equal ($Z_S = Z_L = 50\Omega$). Therefore, VNA systems have been used frequently to measure the channel characteristics of indoor environments [72, 78, 90]. For the measurement of the channel matrix entries of a 2×2 MIMO system, either a 4-port VNA alone or a 2-port one with appropriate switches can be used [72].

5.3 Design and Production of the Patch Antenna Arrays

Design of the coax-fed rectangular patch antennas with 50Ω input impedances are done by employing the analytical expressions given in [91]. In [91], the input impedance of a rectangular microstrip patch antenna excited by a coaxial feed

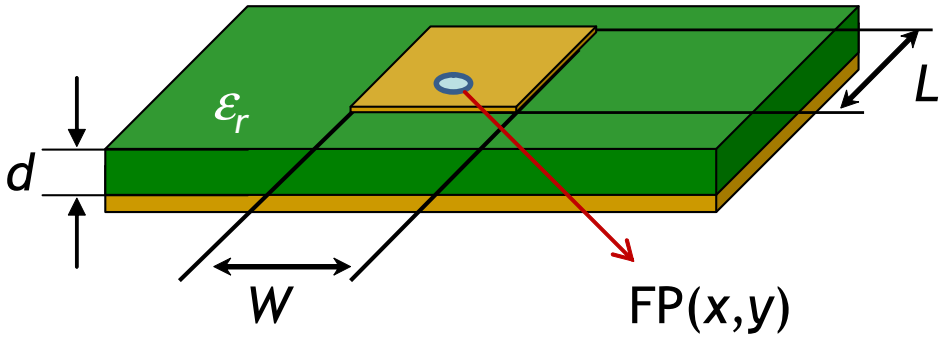

Figure 5.2: Rectangular patch antenna.

Antenna	A	B	C
ϵ_r	3.0	3.2	4.5
$\tan\delta$	0.0040	0.0045	0.0030
d (mm)	1.524	0.508	1.575

Table 5.1: Dielectric substrate parameters

probe is modeled by an equivalent resonant parallel RLC circuit and a serial reactance. An analytical expression is given for the input impedance in terms of the characteristic parameters of the rectangular patch antenna, such as the width, length, dielectric thickness and permittivity and feed point coordinates as shown in Figure 5.2.

Three sets of low loss dielectric substrates with copper at both sides are chosen, characteristic parameters of which are given in Table 5.1. In Table 5.1, ϵ_r and d represent the dielectric permittivity and thickness, respectively. Furthermore, $\tan\delta = \sigma/(\omega\epsilon_0\epsilon_r)$ is the loss tangent which represents the loss due to the conductivity (σ).

The operating frequency is chosen to be $f = 2$ GHz, and using the analytical expressions in [91], the width (W) and length (L) of the rectangular patches and the coordinates of the feed points $[FP(x, y)]$ are obtained as in Table 5.2, to yield $Z_{in} \approx 50\Omega$ or $s_{11} \approx 0$.

Afterwards, the designs are checked by a software package called Ansoft Ensemble [92] to see whether the design objective is achieved. Ansoft Ensemble

Antenna	A	B	C
W	0.353λ	0.339λ	0.301λ
L	0.283λ	0.281λ	0.232λ
$FP(x, y)$	$0.089\lambda, W/2$	$0.209\lambda, W/2$	$0.156\lambda, W/2$

Table 5.2: Rectangular patch parameters

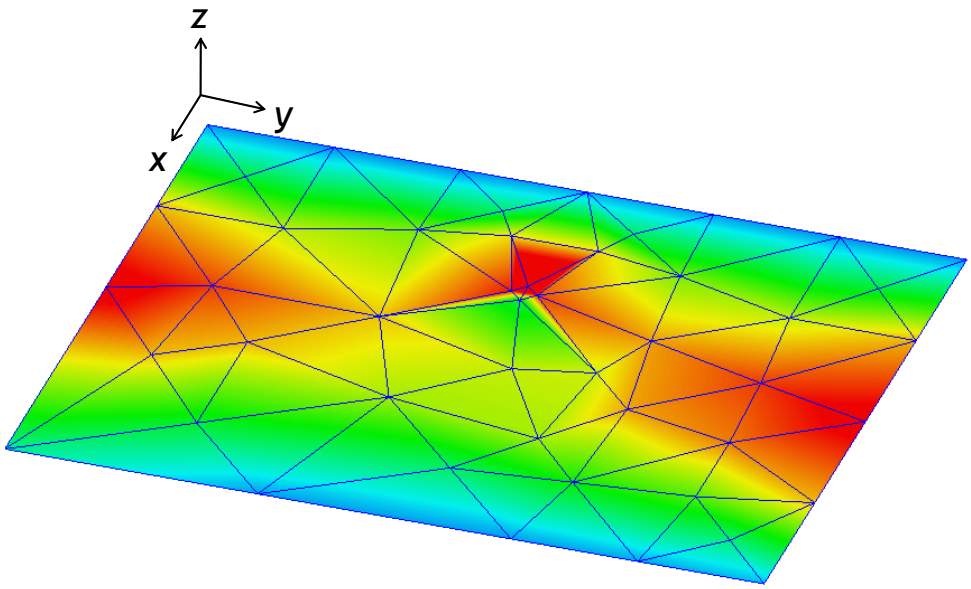

Figure 5.3: The triangular mesh and the magnitude of the current distribution on Antenna A by Ansoft Ensemble.

divides the surface of the geometric model automatically into triangles, collection of which is referred to as the mesh. A mixed-potential integral equation is applied and solved using the method of moments after the surface mesh has been generated. This provides the current distribution throughout the geometry. The solver then uses the current to calculate S-parameters and radiated fields. Figure 5.3 shows the magnitude of the current distribution along with the triangular mesh over Antenna A. Figure 5.4 (a) shows the real and imaginary parts of the input impedances for all three patch antenna designs, and Figure 5.4 (b) depicts the corresponding s_{11} results. Furthermore, the radiation field patterns are illustrated in Figure 5.5.

Since the input impedance results obtained by simulations are quite appealing, antennas having the aforementioned parameters are fabricated. Applying

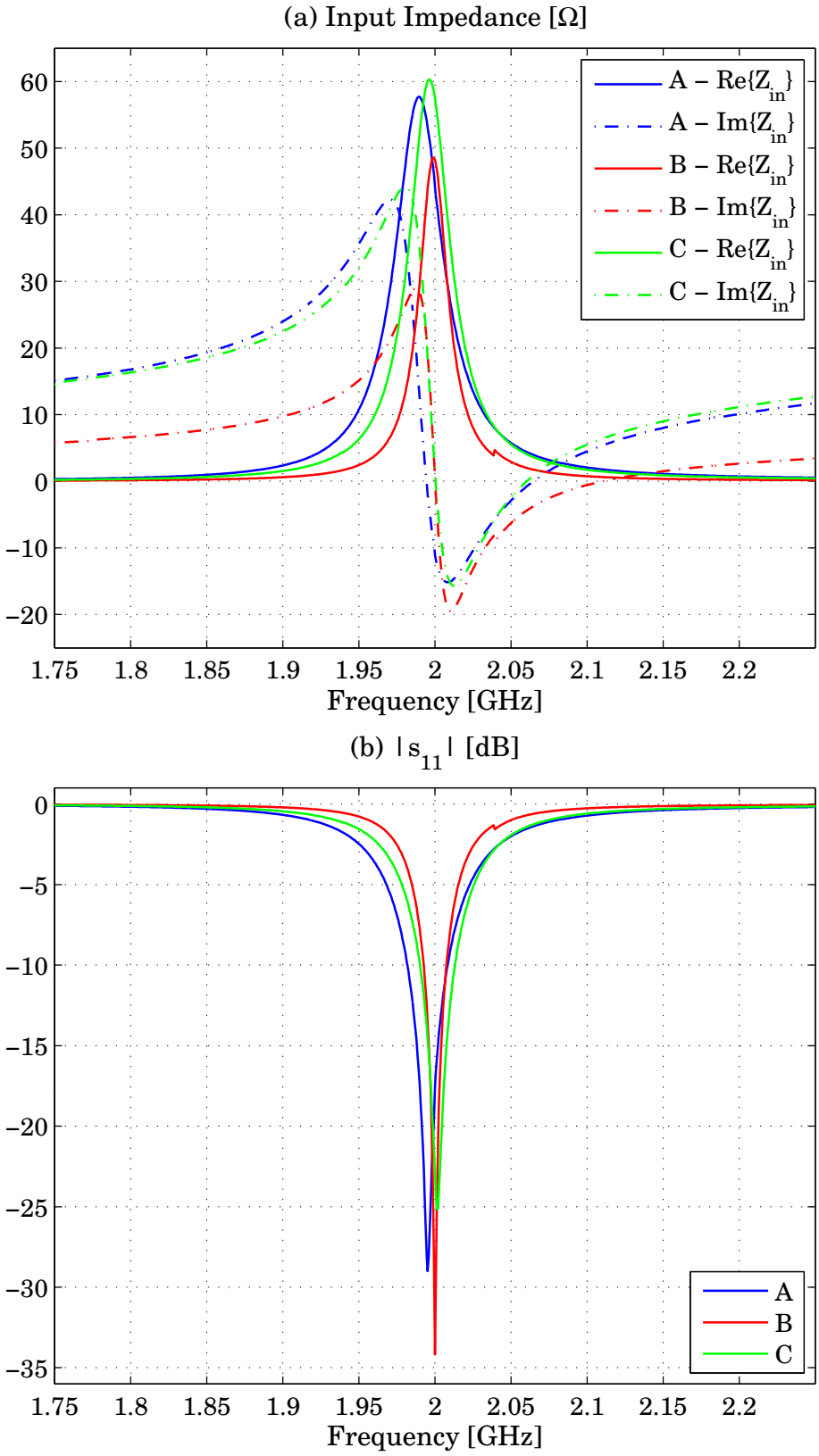

Figure 5.4: Ansoft Ensemble results for single patch antennas (electrical and geometrical parameters of antennas (A, B, C) are given in Tables 5.1 and 5.2). (a) Input impedance. (b) Magnitude of s_{11}.

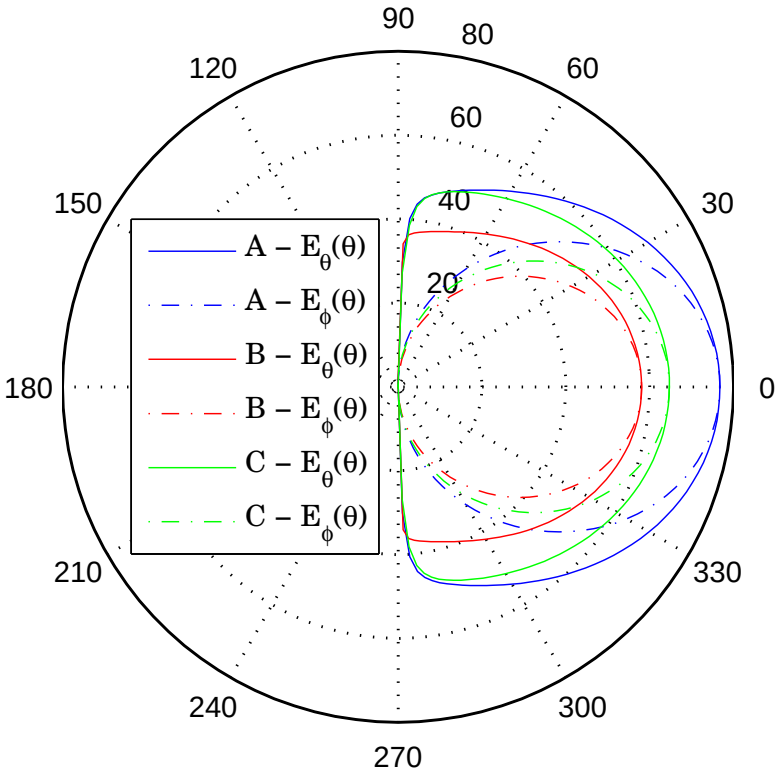

Figure 5.5: Radiation field patterns obtained using Ansoft Ensemble (electrical and geometrical parameters of antennas (A, B, C) are given in Tables 5.1 and 5.2).

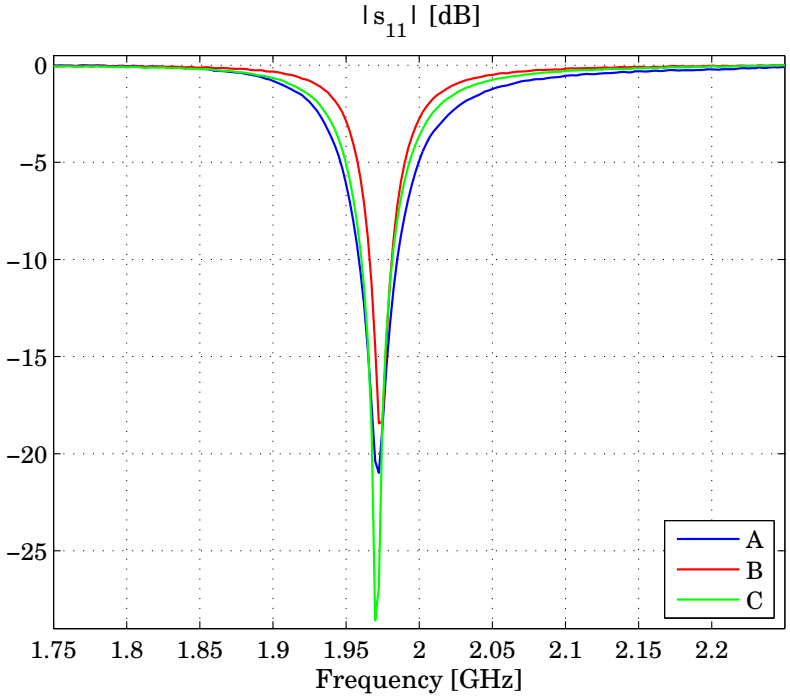

Figure 5.6: Measured $|s_{11}|$ by the use of VNA for fabricated antennas (A, B, C).

Antenna	Δ/λ
A1×2C	0.403
A1×2F	0.800
A2×1C	0.333
A2×1F	0.800
B1×2C	0.388
B1×2F	0.800

Antenna	Δ/λ
B2×1C	0.331
B2×1F	0.800
C1×2C	0.351
C1×2F	0.800
C2×1C	0.282
C2×1F	0.800

Table 5.3: Fabricated patch array configurations with distances between feed point (Δ/λ).

tiny clippings to the patches, all antennas are adjusted to operate at $f = 1.9725$ GHz, as can be seen from the measured s_{11} curves in Figure 5.6. The discrepancy from the simulation results is due to the error limits of method of moments solution of the Ansoft Ensemble, as well as any possible imperfection arising from the fabrication process. Afterwards, arrays with various configurations are fabricated. Mainly, for each substrate type, 2 element arrays are manufactured, antennas of which are located in side-by-side or collinear agreements. To investigate the mutual coupling effects, antenna elements in an array are sited either close to or far away from each other. Table 5.3 shows the configurations of fabricated arrays explicitly. In the table, the collinear agreements are represented by 2×1, whereas 1×2 is used to show the side-by-side elements, just like the matrix notation. Furthermore, arrays with close antennas are symbolized by c, while f stands for the far apart elements. Namely, for instance B1×2F stands for an array with two side-by-side patch elements located apart from each other on a grounded dielectric substrate of thickness 0.508 mm and $\epsilon_r = 3.2$. In Table 5.3, Δ denotes the distance between feed points of antenna elements in an array. Note that, for the closer element configurations, the patches are located physically apart by 0.05λ, therefore, the distance between the feed points is different for each substrate, since the patch sizes are different as well. Moreover, three single antennas on each substrate are fabricated to be the transmitter antenna (i.e., A1×1, B1×1, C1×1) for the single-input-single-output (SISO), and single-input-multiple-output (SIMO) cases. For the receiver array, two different

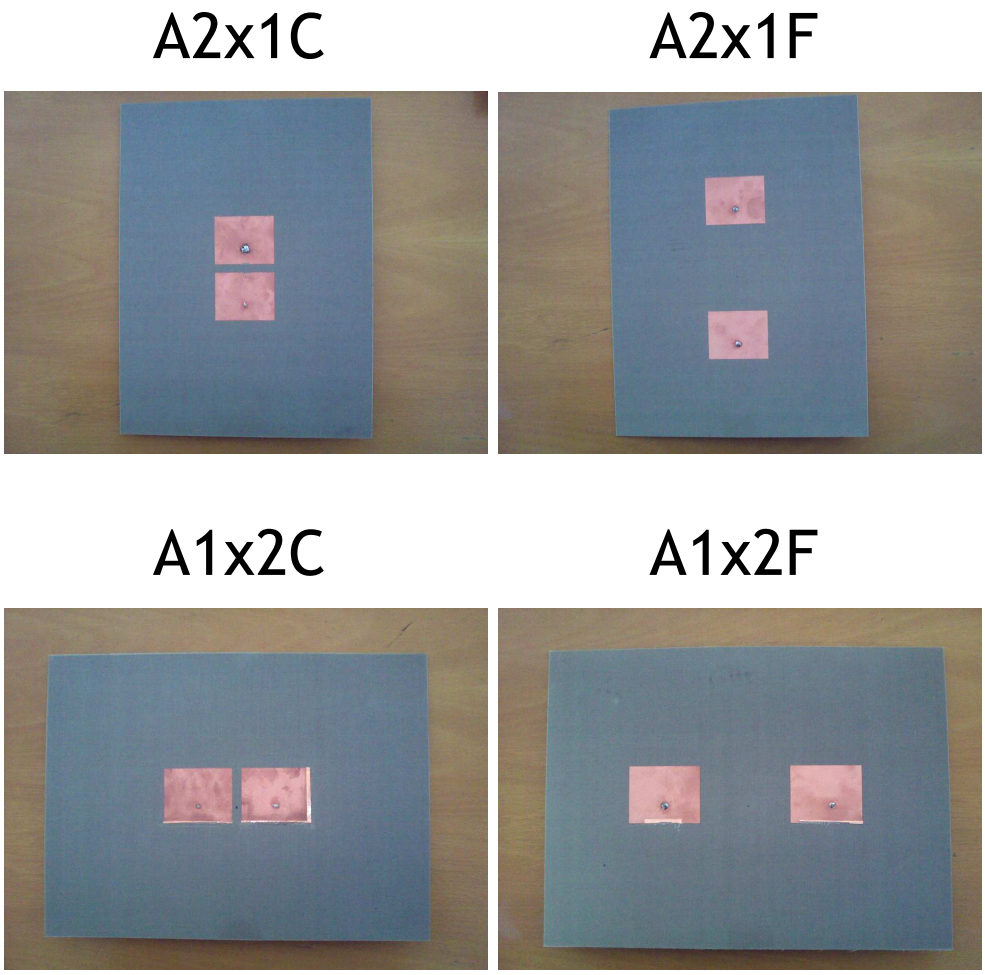

Figure 5.7: 4 different array configurations on substrate A.

configurations are manufactured: (*i*) A1×1 for the SISO case and (*ii*) A1×2F for SIMO and MIMO cases. That is to say, 17 different patch antenna/array configurations are fabricated. In Figure 5.7, 4 of these configurations are shown.

5.4 Indoor MIMO Measurements of Printed Rectangular Patch Antenna Arrays

An indoor measurement setup is established at the Antenna Laboratory of Bilkent University. The schematic representation of the setup is given in Figure 5.8. Aforementioned technique, that is to measure the channel matrix entries by

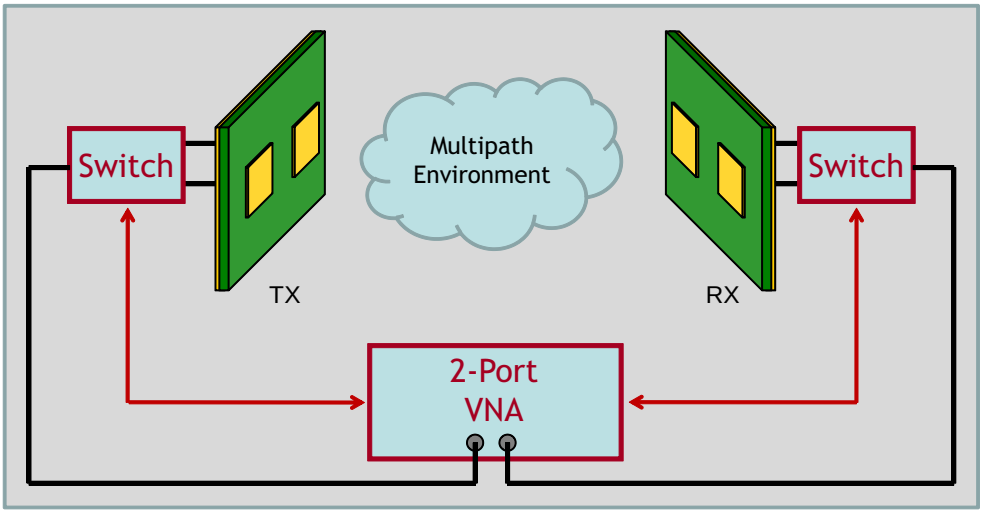

Figure 5.8: Schematic representation of the indoor MIMO measurement setup.

the use of a 2-port VNA and appropriate switches, is adopted as in [72]. The VNA is of the Agilent Technologies, the model of which is ENA5062A. It can work as a typical personal computer as well, since the Microsoft Windows 2000 operating system is installed on the equipment. Two coaxial switches, terminals of which are ended by 50Ω impedances, and two 5 meter long phase stable cables with subminiature version A (SMA) connectors are purchased, which can be seen in Figure 5.9. Also in Figure 5.10, the 2 element receiver array with the switch and cable attached is shown.

The measurement environment is given in 5.11 and sketched in Figure 5.12. It is located at a corner of an empty room with dimensions 16.5 meters by 14.5 meters. The locations of the transmitting and receiving arrays are fixed as the distance between is 3.66 meters, and the line of sight between them is blocked by a box which is covered by aluminum folio. The use of the aluminum here is to obtain conductive obstacles, namely to increase the reflections in the environment. There exist two other covered boxes in the environment along with a table, a chair and the VNA, as well.

For the array configurations given in Table 5.3, SISO, SIMO and MIMO measurements are done. A code is written in Visual Basic Applications (VBA)

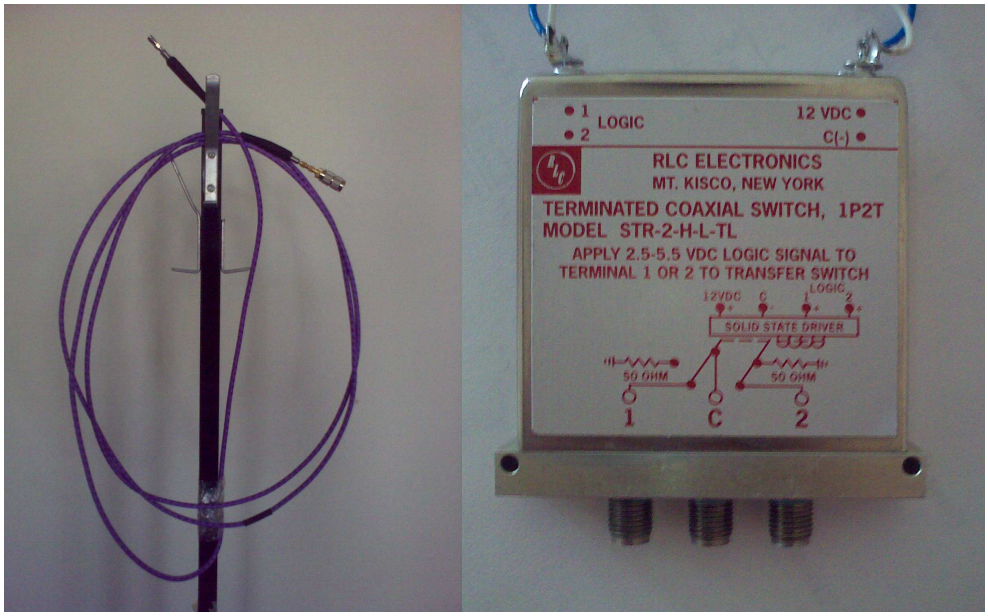

Figure 5.9: The phase stable cable and the coaxial switch.

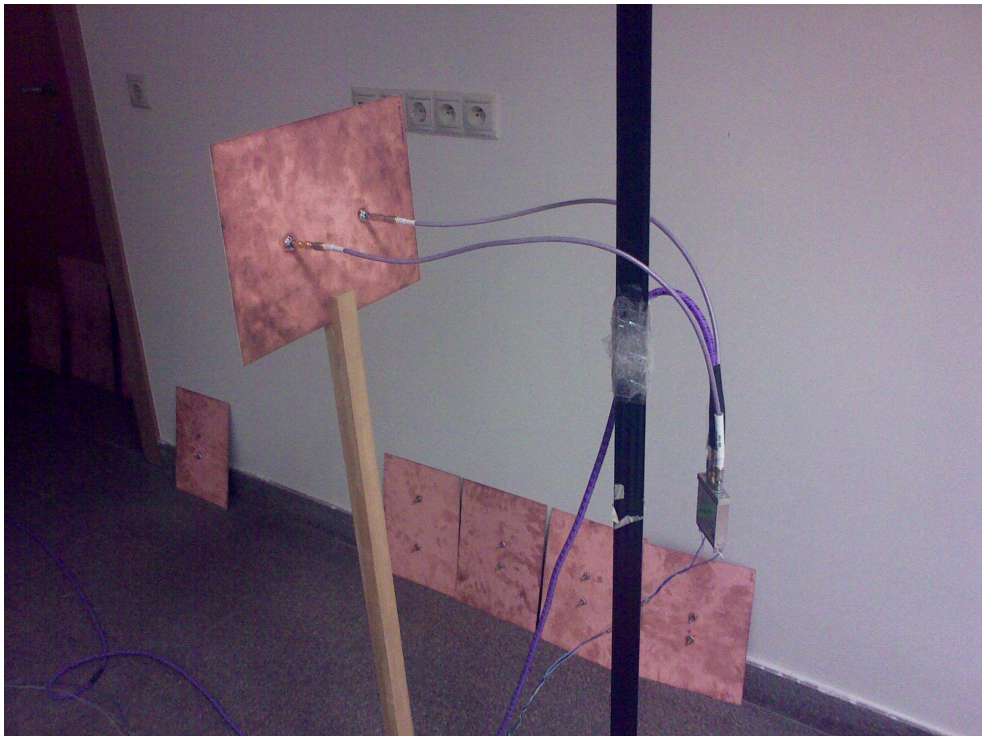

Figure 5.10: The 2 element receiver array with the switch and cable attached.

Figure 5.11: The indoor MIMO measurement environment.

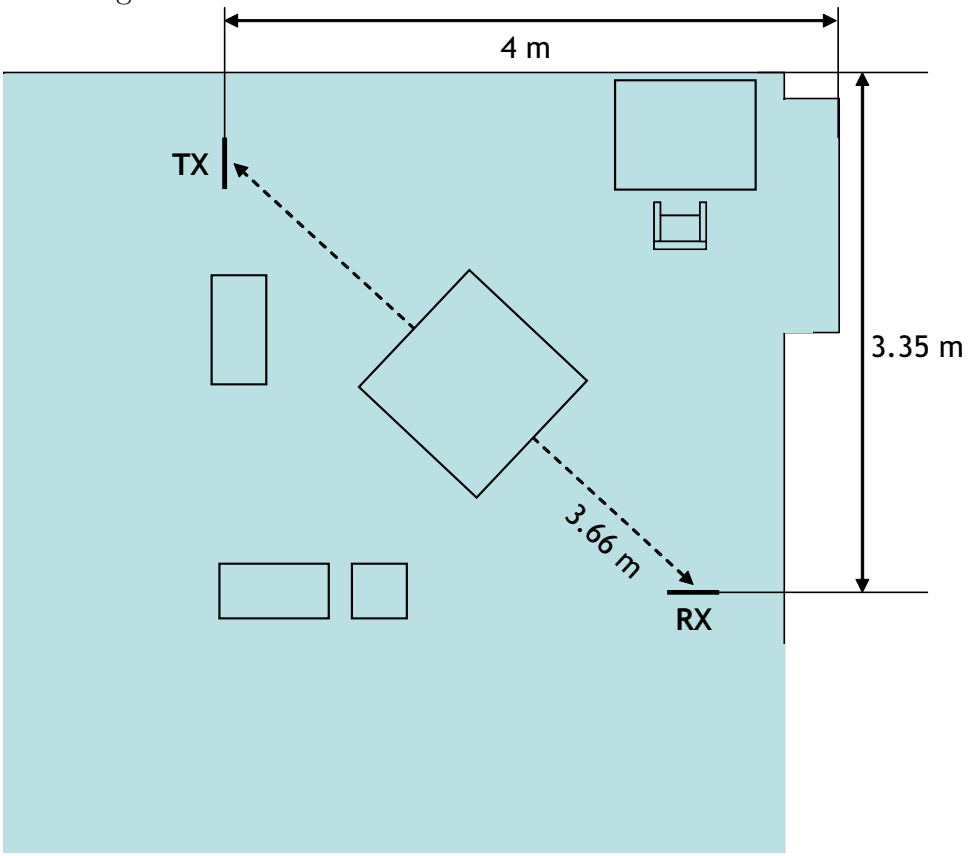

Figure 5.12: The sketch of the environment.

environment, which is inherently installed on the VNA, to trigger the measurements and save the data output. The switches are controlled by the parallel port of the VNA via the code written, by applying 3.3 Volts to one of the transistor-transistor logic (TTL) inputs of the switch, which needs 2.5 Volts at least to alter. Furthermore, the transistors require a 12 Volts biasing voltage to operate, which is applied by a DC source. One measurement process is formed by 1000 successive realizations, and corresponding channel responses (i.e., s_{21} values) are measured through a 201 point frequency sweep between 1.75 and 2.25 GHz and saved. Figure 5.13 illustrates the average channel coefficients over 1000 different measurements in the SISO cases for three different TX array configurations. The narrow band channel can be clearly seen from the figure around 1.9725 GHz. One can absolutely expect that the highest capacity will rise from Antenna A, since the average channel response is the highest in magnitude. The histograms of the magnitude and the phase of the channel response at the operating frequency (1.9725 GHz) for Antenna A is given in Figure 5.14 (a) and (b), respectively. Since there exist neither moving scatterers nor mobile antennas in the environment, the variation in the capacity is very low, and is considered to be due to the inherently unpredictable fluctuations in the readings of the VNA.

Taking the inverse fast Fourier transform of the channel coefficients, the response can be converted to the time domain, resulting a band-limited version of the channel impulse response, $h(t, \tau)$, where t denotes the time and τ is the delay component. As mentioned, the measured channel here is time-invariant. Hence, the average power delay profile (PDP) can be obtained by

$$P(\tau) = \frac{1}{1000} \sum_{r=1}^{1000} |h(r, \tau)|^2 \tag{5.15}$$

where r represents one of the 1000 realizations (or time instances). The normalized average PDPs for Antennas A, B and C are plotted in Figure 5.15. Note that, the power results greater than a threshold value are plotted. The threshold is taken as -25 dB, which is the value of the power seems to contribute before

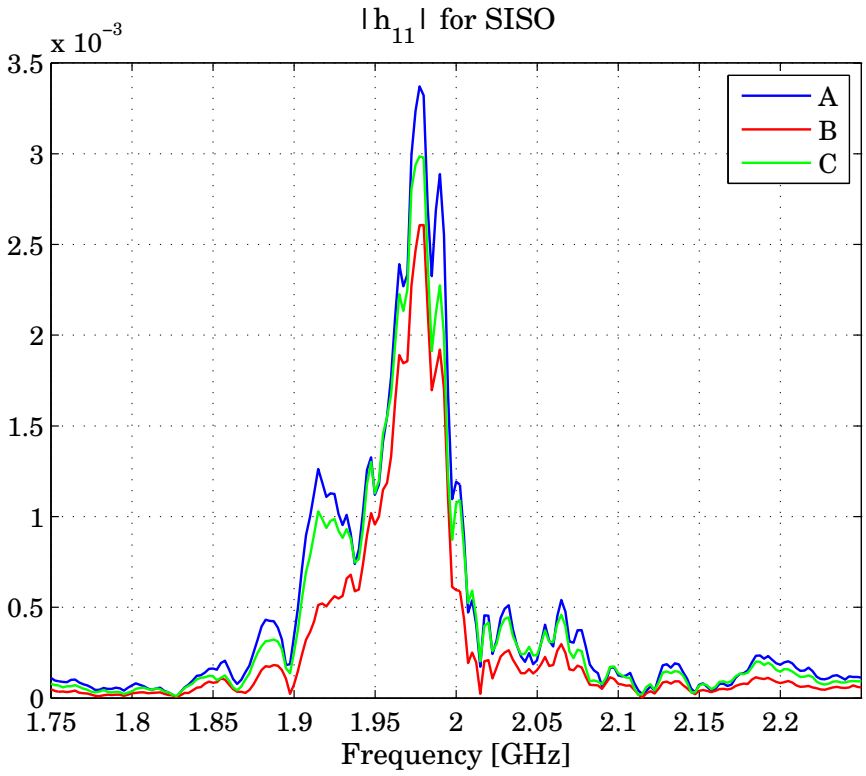

Figure 5.13: The average channel coefficients over 1000 different measurements in the SISO cases for three different TX array configurations.

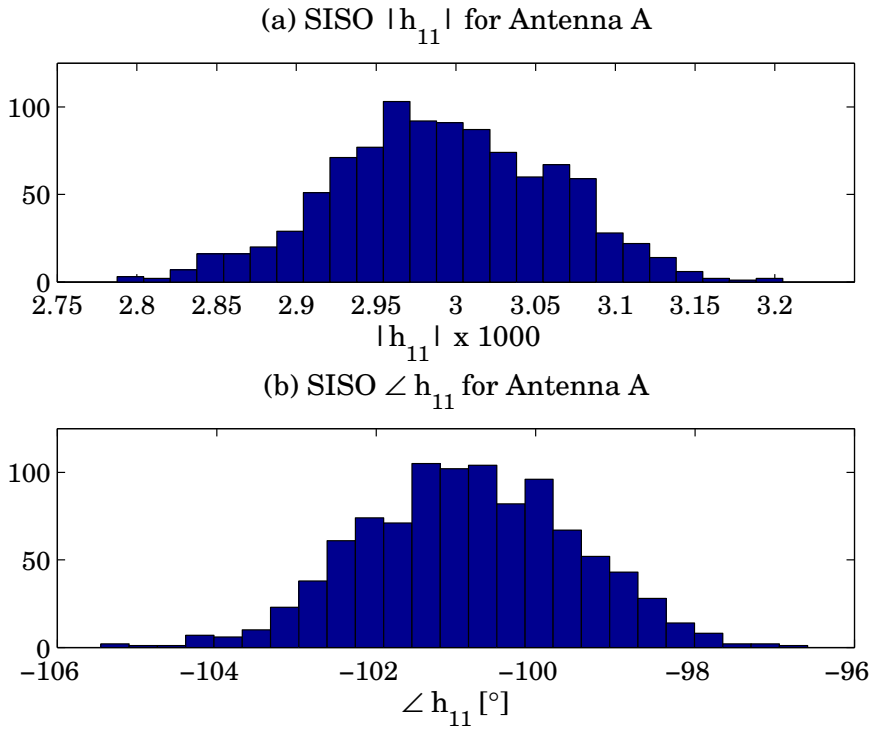

Figure 5.14: The histograms of the measured channel response at the operating frequency (1.9725 GHz) for Antenna A. (a) Magnitude (b) Phase.

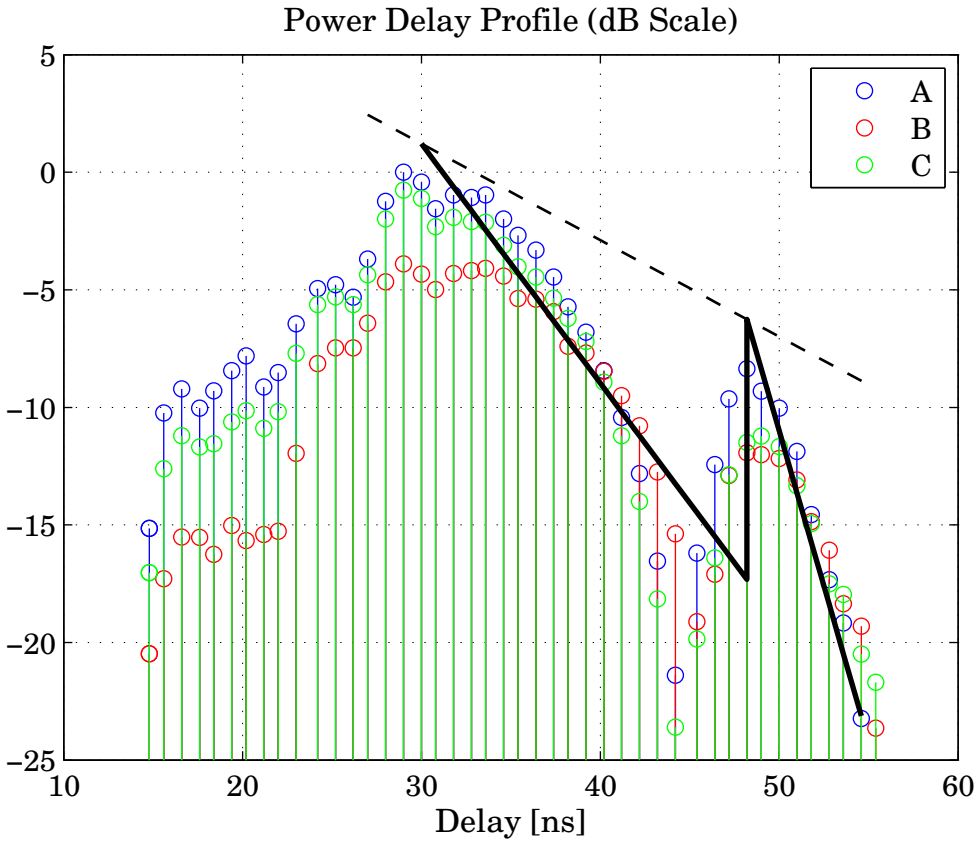

Figure 5.15: The normalized average PDPs of measurements for Antennas A, B and C. The solid black lines represent the exponential decays in the two clusters of scatterers, whereas the dashed one represents the general exponential decay of the power against delay.

the line-of-sight path (τ=12.2 ns). Investigating the figure, one can observe that, there are 2 clusters of scatterers, one composed of paths with delays between 14 and 45 nanoseconds; whereas the paths in the other cluster have delay components between 45 and 56 nanoseconds. Furthermore, the exponential decay of the power (linear in dB scale) both within the clusters, and between the maxima of the envelopes can be noticed, which is consistent with the literature [93].

The mean excess delay, which is the first moment of the given profile can be expressed by

$$< \tau >= \frac{\sum_k P(\tau_k)\tau_k}{\sum_k P(\tau_k)} \tag{5.16}$$

Antenna	A	B	C
$< \tau >$ (ns)	31.2	33.0	31.2
σ_τ (ns)	6.9	7	6.5

Table 5.4: Mean excess delay ($< \tau >$) and rms delay spread (σ_τ) values obtained from the measurements of three antennas.

and the mean square excess delay is

$$< \tau^2 >= \frac{\sum_k P(\tau_k)\tau_k^2}{\sum_k P(\tau_k)} \tag{5.17}$$

and finally, the standard deviation of the PDP gives the root mean square (rms) delay spread, that is

$$\sigma_\tau = \sqrt{< \tau^2 > - < \tau >^2}. \tag{5.18}$$

Table 5.4 shows the mean delay time (mean excess delay) and rms delay spread values obtained from the measurements of three antennas. Note that, these delays are measured relative to the first detectable signal arriving at the receiver, which is not necessarily the largest one [94].

It should be noticed that, although all three antennas are placed in the same location and orientation in a fixed environment, the power delay profile, the mean excess delay and rms delay spread values are different because of the different transmission characteristics, such as the radiation intensities of the antennas. Therefore, it can be concluded that, the channel is antenna dependent as well as its response, time dispersion parameters and capacity.

5.5 Channel Model with Electric Fields (MEF) for Patch Antenna Arrays

In the previously given versions of MEF, the current distribution over free-standing or printed dipole elements was modeled by basis and weighting functions of single mode piecewise sinusoidals. Furthermore, the port currents were

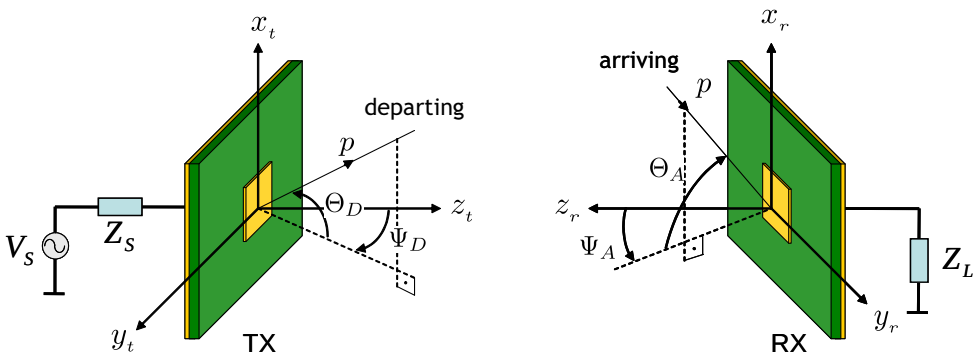

Figure 5.16: SISO wireless communication system where TX and RX patch antennas of are attached to a VNA.

assumed to be the magnitude of these sinusoidal functions, which is found to be successful in [82, 83]. This assumption models the induced currents due to mutual coupling in the same shape as the excited current has, with a difference in the magnitude.

It is obvious that this assumption will fail, when patch antennas are under consideration. Namely, the induced current distribution due to coupling on the patch element under observation will not preserve the shape of the one on the source element. Clearly, on the parts which are closer to the active antenna, more current will be induced. Here we make use of the Ansoft Ensemble again, to handle the patch elements, and modify our MEF accordingly.

5.5.1 SISO Case

Let us consider the SISO wireless communication system in Figure 5.16, TX and RX patch antennas of which are assumed to be attached to a VNA as mentioned in the previous sections. Between them, the pth propagation path is represented by the angle of departure (AoD), $\Omega_{D,p}$, angle of arrival (AoA), $\Omega_{A,p}$, the delay component, τ_p, and 2×2 cross polarized scattering coefficient matrix, $\mathbf{A}_p$. Path angles are taken from both the elevation and azimuthal planes, to create a three dimensional (3D) multipath environment. Namely, (Θ_D, Ψ_D) and

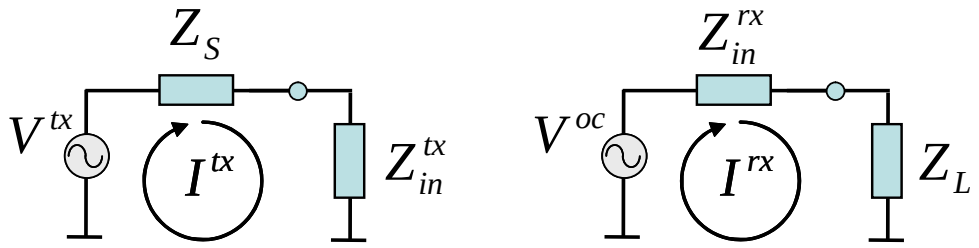

Figure 5.17: The circuit models for patch antennas at TX (left) and RX (right).

(Θ_A, Ψ_A) pairs form the AoD and AoA, respectively. The elevation angles are represented by Θ, whereas the azimuthal ones are shown by Ψ. As illustrated in Figure 5.16, these angles are different from the conventional spherical coordinate angles (θ, ϕ), though all are convertible to each other via simple trigonometric relations. Note that, these parameters are drawn randomly from corresponding probability density functions, which will be given later. It should also be noted that, this multi-path model can involve not only single-bounce scattering but also the multi-bounce one as well, since there is no such restriction on the departing and arriving paths to intersect at one point.

Making use of the circuit models in Figure 5.17, the channel response will be

$$h = V^{rx} \tag{5.19}$$

if the source is activated by $V^{tx} = 1$ V, as we did previously. The received voltage can be expressed in terms of the induced one and the input impedance of the receiver patch by

$$V^{rx} = I^{rx}\ Z_L = \frac{V^{oc}}{Z_{in}^{rx} + Z_L}\ Z_L. \tag{5.20}$$

Since the system will be utilized to model a measurement setup in which a VNA is used, source and load impedances are taken as $Z_S = Z_L = 50\ \Omega$, and Z_{in}^{tx} and Z_{in}^{rx} will be the impedances read by the VNA seen through the transmitter and receiver antenna ports, respectively.

In (5.20), V^{oc} is the induced (or open circuit) voltage, expression of which is given in [79] by

$$V^{oc} = \bar{E}^{rx} \cdot \bar{l}^{e} = l_{\theta}^{e} E_{\theta}^{rx} + l_{\phi}^{e} E_{\phi}^{rx} \tag{5.21}$$

where, $\bar{E}^{rx}$ is the total electric field on the RX element, and $\bar{l}^e$ is the vector effective length [79] of it. Note that, $\bar{E}^{rx}$ is the sum of the fields incident through multi-paths and their reflection from the ground plane beneath the substrate. Namely, the expression for $\bar{E}^{rx}$ can be given by

$$E_\theta^{rx} = \sum_p (1 - R_{\theta,p})\ E_\theta^{inc}(\theta_p^r, \phi_p^r) \tag{5.22}$$

$$E_\phi^{rx} = \sum_p (1 + R_{\phi,p})\ E_\phi^{inc}(\theta_p^r, \phi_p^r) \tag{5.23}$$

where $E_{\theta,\phi}^{inc}(\theta_p^r, \phi_p^r)$ are the field components incident on the RX antenna arriving through the pth path, corresponding spherical coordinate angles of which are (θ_p^r, ϕ_p^r) derived from the randomly generated $\Omega_{A,p}$. $R_{\theta,p}$ and $R_{\phi,p}$ are the reflection coefficients due to the field polarizations, expressions of which are given as follows [95]:

$$R_{\theta,p} = \frac{k_d \cos\theta_p^r - j z_d \sqrt{k_d^2 - k^2 \sin^2\theta_p^r}\ \tan\left(\sqrt{k_d^2 - k^2 \sin^2\theta_p^r}\ d\right)}{k_d \cos\theta_p^r + j z_d \sqrt{k_d^2 - k^2 \sin^2\theta_p^r}\ \tan\left(\sqrt{k_d^2 - k^2 \sin^2\theta_p^r}\ d\right)} \tag{5.24}$$

$$R_{\phi,p} = \frac{k_d \cos\theta_p^r + j y_d \sqrt{k_d^2 - k^2 \sin^2\theta_p^r}\ \cot\left(\sqrt{k_d^2 - k^2 \sin^2\theta_p^r}\ d\right)}{k_d \cos\theta_p^r - j y_d \sqrt{k_d^2 - k^2 \sin^2\theta_p^r}\ \cot\left(\sqrt{k_d^2 - k^2 \sin^2\theta_p^r}\ d\right)} \tag{5.25}$$

with

$$y_d = \sqrt{\epsilon_r}, \tag{5.26}$$

$$z_d = \frac{1}{y_d} \tag{5.27}$$

and

$$k_d = \sqrt{\epsilon_r}\ k. \tag{5.28}$$

From the definition of the vector effective length in [79], $\bar{l}^e$ can be written for the RX antenna as follows:

$$\bar{l}^e(\theta_p^r, \phi_p^r) = \frac{\bar{E}_{rad}^{rx}(\theta_p^r, \phi_p^r)}{-jk30I_{in}}\ \frac{R}{e^{-jkR}} \tag{5.29}$$

where $\bar{E}_{rad}^{rx}$ is radiated field of the patch antenna at RX when a current I^{in} is applied at the port, and R is the distance from RX. The usage of the Ansoft

Ensemble intervenes at this very point. Since the Ansoft Ensemble can give us

$$\bar{E}^{rx}_{en}(\theta^r_p, \phi^r_p) = \bar{E}^{rx}_{rad}(\theta^r_p, \phi^r_p)\ \frac{R}{e^{-jkR}} \tag{5.30}$$

when $I_{in} = 1$ A, the vector effective length of the patch antenna at RX turns out to be

$$\bar{l}^e(\theta^r_p, \phi^r_p) = \frac{\bar{E}^{rx}_{en}(\theta^r_p, \phi^r_p)}{-jk30} \tag{5.31}$$

and finally the open circuit voltage induced on the RX antenna can be expressed by

$$\begin{aligned} V^{oc} = \frac{j}{30k}\sum_p \quad & \left\{E^{rx}_{en,\theta}(\theta^r_p, \phi^r_p)\ E^{inc}_{\theta}(\theta^r_p, \phi^r_p)\ (1 - R_{\theta,p})\right. \\ & \left. + E^{rx}_{en,\phi}(\theta^r_p, \phi^r_p)\ E^{inc}_{\phi}(\theta^r_p, \phi^r_p)\ (1 + R_{\phi,p})\right\}. \end{aligned} \tag{5.32}$$

The field arriving through the pth path can be written in terms of the radiated fields by the transmitter patch antenna ($\bar{E}^{tx}$) by

$$\bar{E}^{inc}_p = \mathbf{A}_p\ \bar{E}^{tx}_p \tag{5.33}$$

$$\begin{bmatrix} E^{inc}_{\theta}(\theta^r_p, \phi^r_p) \\ E^{inc}_{\phi}(\theta^r_p, \phi^r_p) \end{bmatrix} = \begin{bmatrix} \alpha^{\theta\theta}_p & \alpha^{\theta\phi}_p \\ \alpha^{\phi\theta}_p & \alpha^{\phi\phi}_p \end{bmatrix} \begin{bmatrix} E^{tx}_{\theta}(\theta^t_p, \phi^t_p) \\ E^{tx}_{\phi}(\theta^t_p, \phi^t_p) \end{bmatrix} e^{-jkc\tau_p} \tag{5.34}$$

where (θ^t_p, ϕ^t_p) are the spherical coordinate angles of the departure, linked with the pth path, derived from the randomly generated $\Omega_{D,p}$; and $c\tau_p$ is the total length due to the same path.

We again appeal to the Ansoft Ensemble for the evaluation of the fields radiated by the TX patch antenna. Note that, $\bar{E}^{tx}(\theta^t_p, \phi^t_p)$ is the field radiated by the TX patch antenna, when $V^{tx} = 1$ V (say the port current in this case is I^{tx}). However, Ansoft Ensemble gives us the radiated fields for $I_{in} = 1$ A. Then, by the use of the circuit model for TX given in Figure 5.17, the transmitted fields can be obtained via the fields by Ensemble as:

$$\bar{E}^{tx}(\theta^t_p, \phi^t_p) = I^{tx}\ \bar{E}^{tx}_{en}(\theta^t_p, \phi^t_p) = \frac{\bar{E}^{tx}_{en}(\theta^t_p, \phi^t_p)}{Z^{tx}_{in} + Z_S}. \tag{5.35}$$

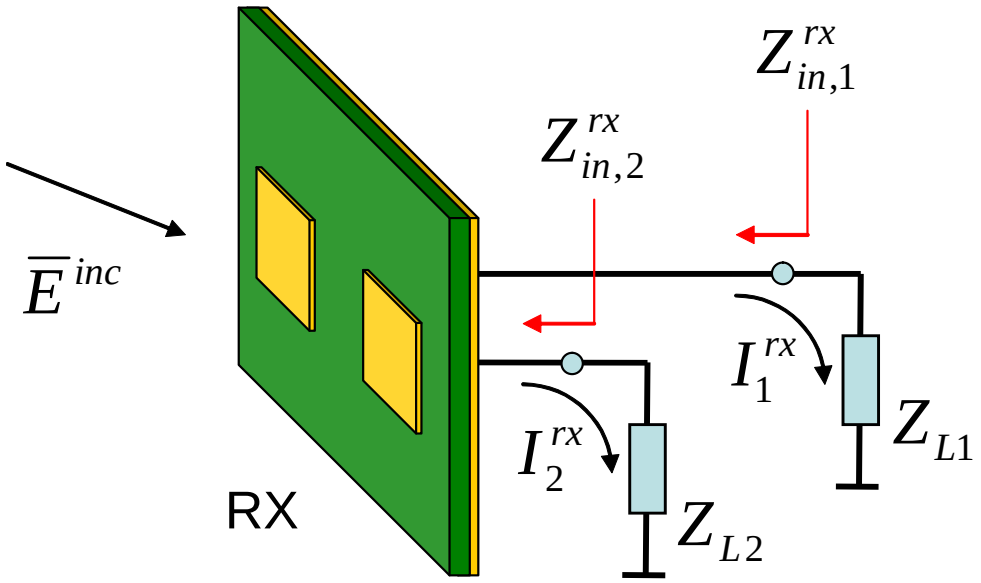

Figure 5.18: Multiple antennas at the receiver side.

Equations (5.20)-(5.35) relate the source voltage of a TX patch antenna to the received voltage by another one, and hence, are fully capable to obtain the channel response, i.e., (5.19), for the SISO case.

5.5.2 Multiple Patches at RX

Inspecting Figure 5.18, let the electric field incident on the 2-element patch array at RX, $\bar{E}^{inc}$, creates the currents $I_{1,2}^{rx}$ at the ports of the RX array, along with the reflected fields from the ground plane. Let us denote the radiated field by this array, when its antennas are excited by input currents I_1 and I_2, with $\bar{E}_{rad}^{rx}(I_1, I_2)$. Utilizing the superposition principle, this field can be rewritten as,

$$\bar{E}_{rad}^{rx}(I_1, I_2) = I_1\ \bar{E}_{rad}^{rx}(1,0) + I_2\ \bar{E}_{rad}^{rx}(0,1). \tag{5.36}$$

where $\bar{E}_{rad}^{rx}(1,0)$ and $\bar{E}_{rad}^{rx}(0,1)$ are the complex active element field patterns for the first and second patch, respectively, in which the mutual coupling is already included, since zero port current does not mean zero induced current distribution due to coupling on the passive element. The active element fields are obtained via the method of moments solution by the Ansoft Ensemble as well, sample

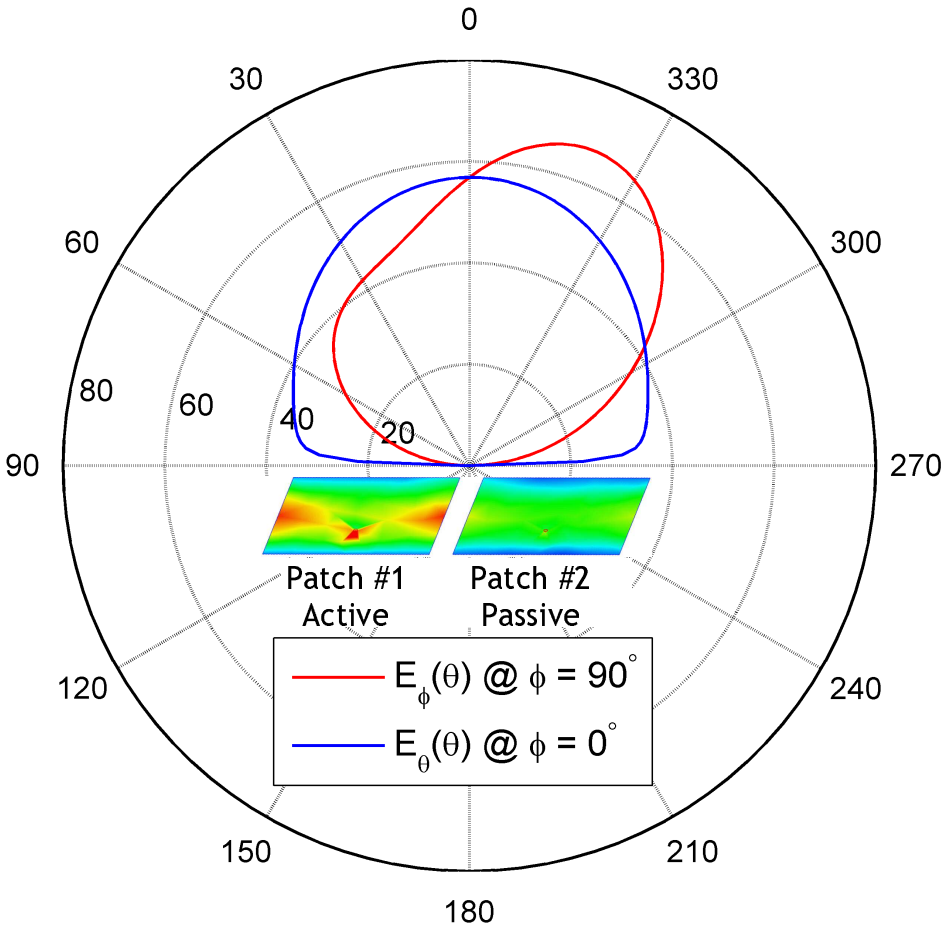

Figure 5.19: The active element patterns by the Ansoft Ensemble, $\bar{E}^{rx}_{en}(1,0)$.

patterns of which are plotted in Figure 5.19 for the receiver array of 2 patch elements considered in this work. It should be noted that, in the course of the calculation of the active element pattern of one patch antenna, the other port is assumed to be terminated by $Z_L = 50\ \Omega$, as in the case of measurements done by the VNA along with the switch operation.

Making use of the vector effective length definition given in (5.29) again, the induced open circuit voltages on the receiving patch elements can be expressed by,

$$V_1^{oc} = \frac{j}{30k}\ \bar{E}^{rx}_{rad}(1,0) \cdot [\hat{a}_\theta\ E^{inc}_\theta\ (1 - R_\theta) + \hat{a}_\phi\ E^{inc}_\phi\ (1 + R_\phi)] \tag{5.37}$$

$$V_2^{oc} = \frac{j}{30k}\ \bar{E}^{rx}_{rad}(0,1) \cdot [\hat{a}_\theta\ E^{inc}_\theta\ (1 - R_\theta) + \hat{a}_\phi\ E^{inc}_\phi\ (1 + R_\phi)]. \tag{5.38}$$

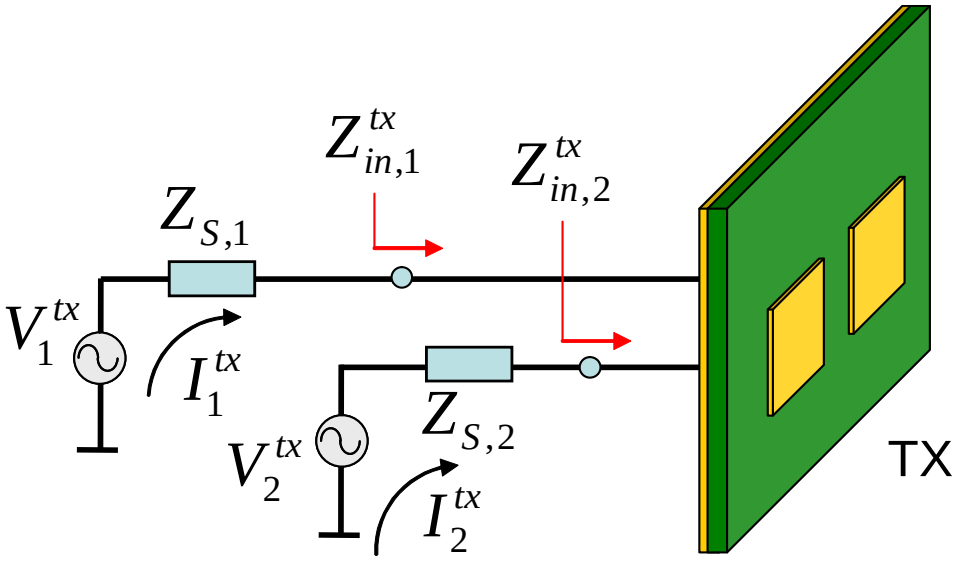

Figure 5.20: Multiple antennas at the transmitter side.

Note that, the open circuit voltage expressions in (5.37)-(5.38) already include the mutual coupling effects due to the active element patterns. Therefore, the use of the circuit model given in Figure 5.17 is adequate to evaluate the received voltages, i.e.,

$$V_1^{rx} = I_1^{rx}\ Z_{L,1} = \frac{V_1^{oc}}{Z_{in,1}^{rx} + Z_{L,1}}\ Z_{L,1} \tag{5.39}$$

$$V_2^{rx} = I_2^{rx}\ Z_{L,2} = \frac{V_2^{oc}}{Z_{in,2}^{rx} + Z_{L,2}}\ Z_{L,2} \tag{5.40}$$

where $Z_{L,m} = 50\ \Omega$ are the termination impedances with $m = 1, 2$, and $Z_{in,m}^{rx}$ is the input impedance seen through the mth antenna port by the VNA, in the presence of the nth patch antenna with $n \neq m$, whilst the nth port is terminated by 50 Ω.

Then in the SIMO case, relating the incident field upon the RX array to the electric fields emitted by the transmitter patch antenna just the same as in (5.34)-(5.35), the 2×1 channel response matrix entries can be expressed by,

$$h_{11} = \frac{V_1^{rx}}{V^{tx}} = V_1^{rx} \tag{5.41}$$

$$h_{21} = \frac{V_2^{rx}}{V^{tx}} = V_2^{rx} \tag{5.42}$$

since the transmitter patch antenna is activated by $V^{tx} = 1$ V.

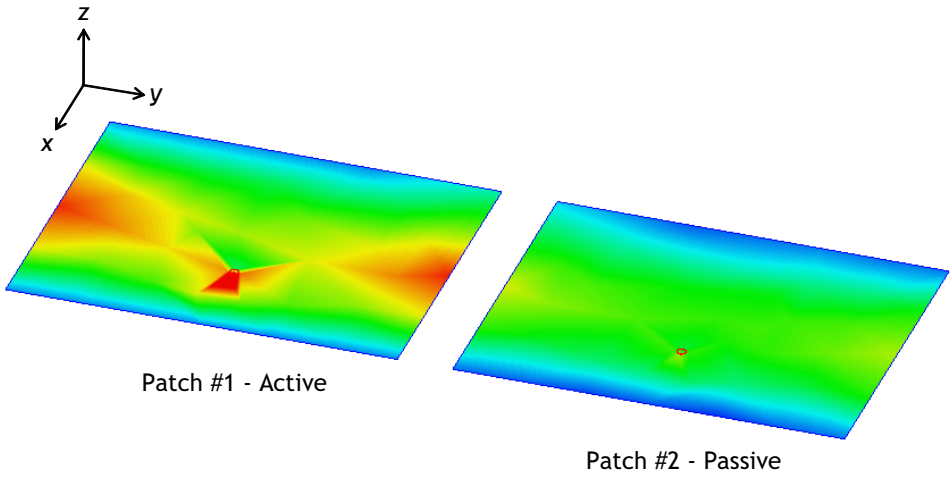

Figure 5.21: Currents induced on the array elements by Ensemble, when the first antenna is activated.

5.5.3 Multiple Patch Antennas at TX

As we can evaluate the active element field patterns of given patch antenna arrays, we may make use of them to obtain the radiated fields by the TX array with mutual coupling, in the direction of the pth departing path as well. Noticing Figure 5.20, utilizing the circuit model in Figure 5.17, and applying the MEF procedure by activating the first antenna by $V_1^{tx} = 1$ V and $V_2^{tx} = 0$; the current constituted upon the port of the first patch antenna is

$$I_1^{tx} = \frac{V_1^{tx}}{Z_{in,1}^{tx} + Z_{S,1}} = \frac{1}{Z_{in,1}^{tx} + Z_{S,1}} \tag{5.43}$$

where $Z_{S,1} = 50\ \Omega = Z_{S,2}$ is the source impedance, and $Z_{in,1}^{tx}$ is the input impedance seen through the first antenna port by the VNA, in the presence of the other patch antenna, whilst the second port is terminated by 50 Ω. Then, the field emitted by the TX array in the direction of the pth departing path, $\bar{E}_p^{tx}$, can be written in terms of the active element pattern of the first antenna, $\bar{E}_p^{tx}(1,0)$, by

$$\bar{E}_p^{tx} = I_1^{tx}\ \bar{E}_p^{tx}(1,0). \tag{5.44}$$

Note that, during the evaluation of the active element pattern of the first antenna by the Ansoft Ensemble, $\bar{E}_p^{tx}(1,0)$, the port current at the second port

is inherently forced to be $I_2^{tx} = 0$. However, this does not mean that the second antenna does not contribute to the radiated field, because of the current induced on the passive element due to mutual coupling as seen in Figure 5.21.

Relating, in advance, the transmitted fields to the incident ones upon the RX array as in (5.34)-(5.35), and then, the incident fields to the received voltages as in (5.37)-(5.40); the channel matrix entries can be evaluated for the first antenna is activated (i.e., h_{11} and h_{21}).

Similarly, when the second antenna is activated by $V_2^{tx} = 1$ V and $V_1^{tx} = 0$, the field emitted by the TX array can be written in terms of the active element pattern of the second antenna, $\bar{E}_p^{tx} = \bar{E}_p^{tx}(0,1)/(Z_{in,2}^{tx} + Z_{S,2})$. Referring to the corresponding equations again, which relate the transmitted fields to the received voltages, the channel matrix entries can be evaluated as,

$$h_{12} = \frac{V_1^{rx}}{V_2^{tx}} = V_1^{rx} \tag{5.45}$$

$$h_{22} = \frac{V_2^{rx}}{V_2^{tx}} = V_2^{rx} \tag{5.46}$$

for the second antenna is activated.

5.6 Experimental and Numerical Results

5.6.1 The Multipath Scenario

The parameters of the aforementioned 3D, multi-bounce scattering environment for MEF are given here. Over $N_R = 1000$ scenario realizations, all path angles are defined with Laplacian distributions of zero mean and specific angular spread values (σ_{Θ_D}, σ_{Θ_A}, σ_{Ψ_D}, σ_{Ψ_A}), as

$$\Phi = -\frac{\sigma}{\sqrt{2}} \operatorname{sgn}(\mathcal{U} - 0.5) \ln(1 - 2|\mathcal{U} - 0.5|). \tag{5.47}$$

σ_{Θ_D}	σ_{Θ_A}	σ_{Ψ_D}	σ_{Ψ_A}
25°	25°	30°	30°

Table 5.5: Multipath scenario parameters

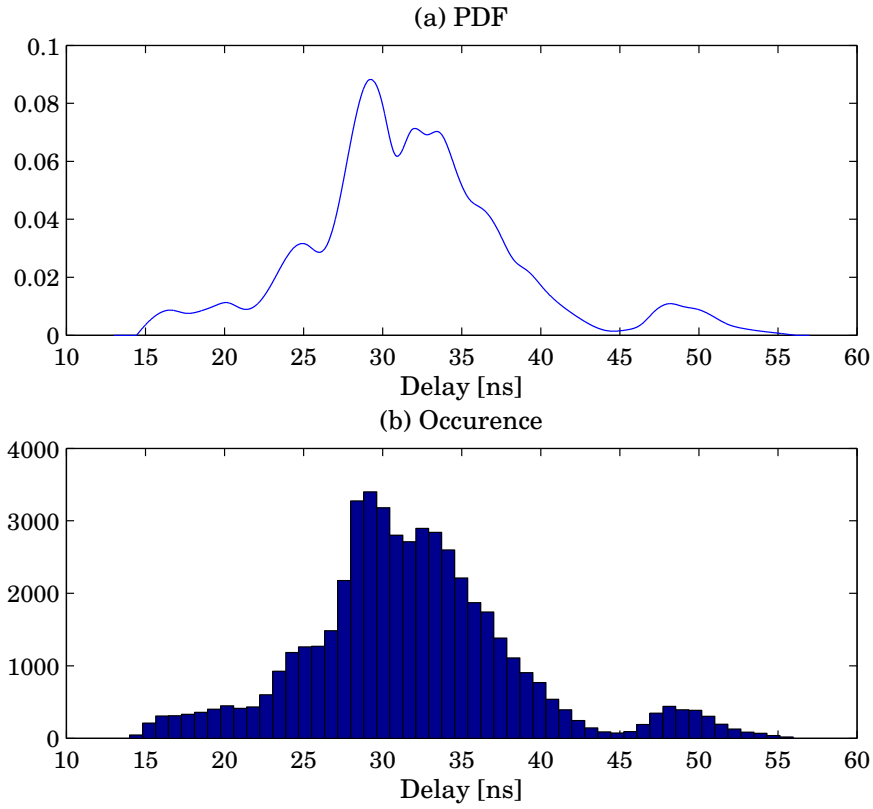

Figure 5.22: (a) The probability distribution function obtained from the measured PDPs (b) Generated delay components.

where $\mathcal{U}$ is drawn from the uniform distribution on the unit interval $(0, 1]$; and, the entries of the cross polarized scattering coefficient matrix are chosen to be independent and identically-distributed (iid) random variables of zero mean and unit variance. Thus, we will have Laplacian power azimuth/elevation spectra. Numerical values for all parameters for the distributions utilized in this work are given in Table 5.5. In each channel realization, $S = 50$ paths are assumed. Note that, the choice of the Laplacian distributed power azimuth/elevation spectra, as well as the larger azimuthal spread, is consistent with the measurements in the literature [93].

Antenna	A	B	C
ϵ_r	3.0	3.2	4.5
$\tan\delta$	0.0040	0.0045	0.0030
d (mm)	1.524	0.508	1.575

Table 5.6: Dielectric substrate parameters

The delay components are drawn randomly from a specific probability distribution function (PDF). The measured power delay profiles previously given for three different antenna types in Figure 5.15 are averaged (in the linear magnitude scale), and normalized to form a PDF (i.e., the integral of it over the delay domain gives one). The resulting PDF is plotted in Figure 5.22 (a), along with the histogram of generated $N_R \cdot S$ delay components in 5.22 (b). For each of the $N_R = 1000$ realizations, $S = 50$ of these delay components are chosen uniformly and associated with the previously generated angles and scattering matrices to form the corresponding paths.

5.6.2 SISO Results

The capacity result for the rth measurement realization is obtained by

$$\mathcal{C}_r = \log_2\left(\left|\mathbf{I}_R + \frac{\rho_T}{T}\mathbf{H}\mathbf{H}^h\right|\right) \tag{5.48}$$

and they are averaged over $N_R = 1000$ total realizations to find the mean capacity results, such as

$$\mathcal{C} = \mathcal{E}[\mathcal{C}_r] = \frac{1}{N_R}\sum_{r=1}^{N_R}\mathcal{C}_r \tag{5.49}$$

where $\mathbf{I}_R$ is the $R\times R$ identity matrix, $|.|$ is the matrix determinant, $\rho_{_T}$ is the total transmitted signal to noise ratio (SNR) with $(.)^h$ and $\mathcal{E}[.]$ denoting the conjugate transpose and expectation operations, respectively. Note that, $R = T = 1$ for the SISO case.

Figure 5.23 shows the histograms of the measured capacities for three different antenna configurations. The transmitted SNR is adjusted such that, the mean

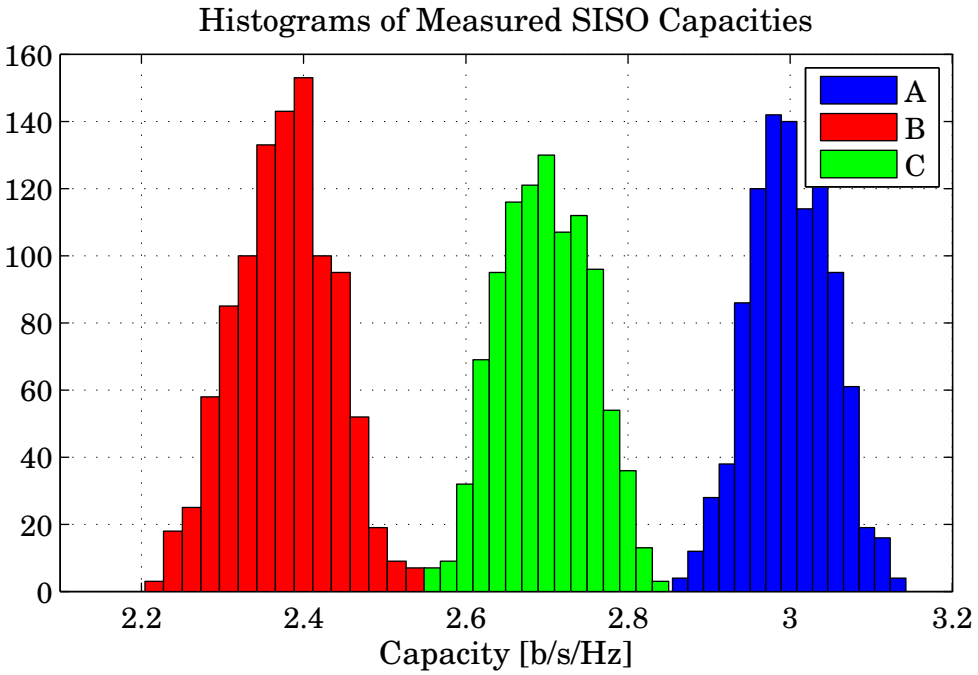

Figure 5.23: Histograms of the capacities for measurements of three different antenna configurations.

capacity of Antenna A is 3 b/s/Hz. It is observed that, as expected from Figure 5.13, Antenna A has a larger capacity than the others. As concluded in Chapter 3, the thinner the substrate, the less the capacity, since the ground plane is closer to the antenna, and tends to cancel the effects due to the image theory.

The comparison of the mean capacities by MEF and measurements is illustrated in Figure 5.24. Very good agreement is observed between the proposed MEF and the measurement results within 5 percent absolute error. Since the substrate upon which Antenna B is located, is very thin relative to other substrates, the structure can be easily bent, and it is difficult to stabilize. The discrepancy for Antenna B may arise from this reason.

Moreover, the PDP results by MEF and measurements are compared in Figure 5.25. The normalized received power versus delay is plotted in the linear magnitude scale. Again, good agreement is observed. Finally, the received power azimuth and elevation spectra obtained by MEF results are illustrated in Figure

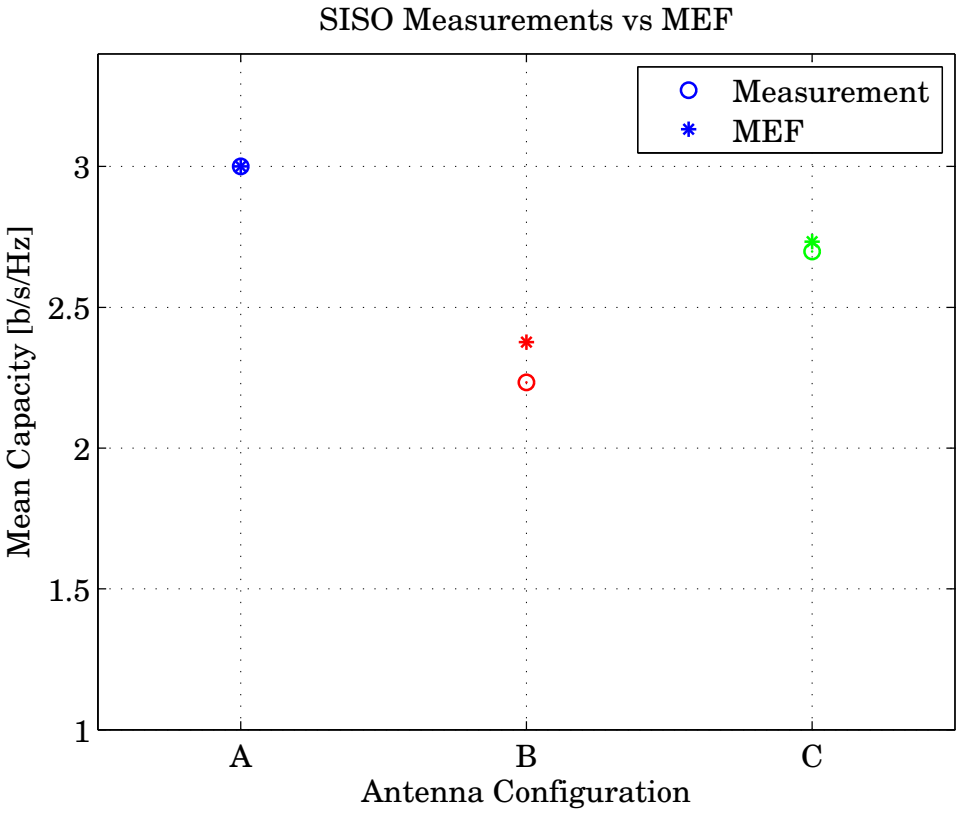

Figure 5.24: The comparison of the mean capacities by MEF and measurements.

5.26. The received power is normalized and plotted against Ψ_A and Θ_A. Figure 5.26 also shows the Laplacian fit curves to the MEF data.

5.6.3 SIMO and MIMO Results

Figure 5.27 shows the histograms of the measured SIMO capacities for three different antenna configurations at TX. Note that, in the course of the evaluation of capacity values, $R = 2$ and $T = 1$ in the SIMO case. The receiver array is taken as A1x2C for all SIMO and MIMO measurements. The comparison of the mean capacities by MEF and measurements is illustrated in Figure 5.28. Very good agreement is observed between the proposed MEF and the measurement results with less than 6 percent absolute error.

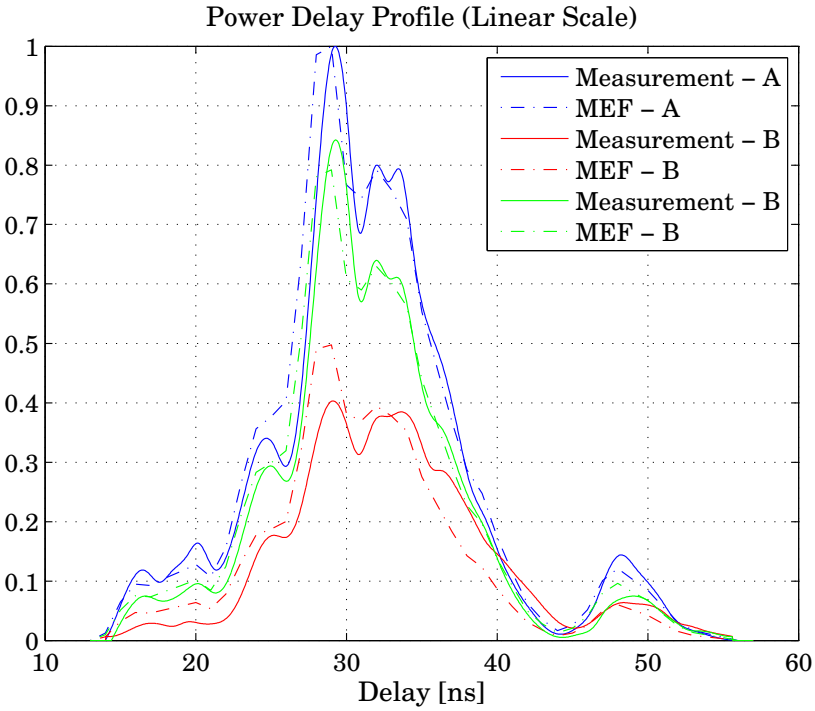

Figure 5.25: The received power delay profile results by MEF and measurements.

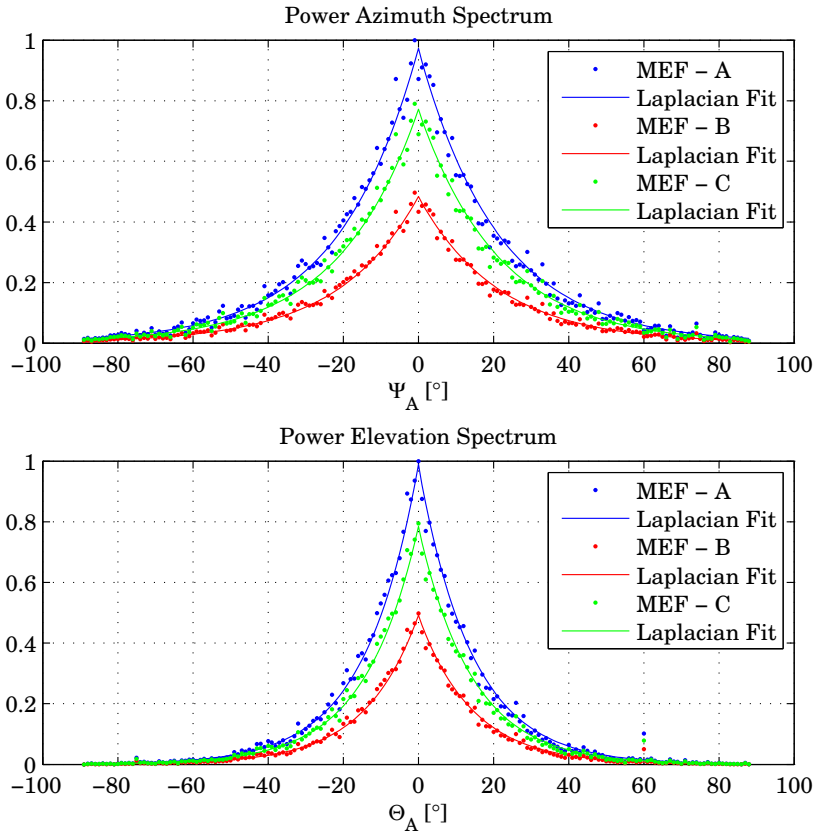

Figure 5.26: The received power azimuth (top) and elevation (bottom) spectra obtained by MEF.

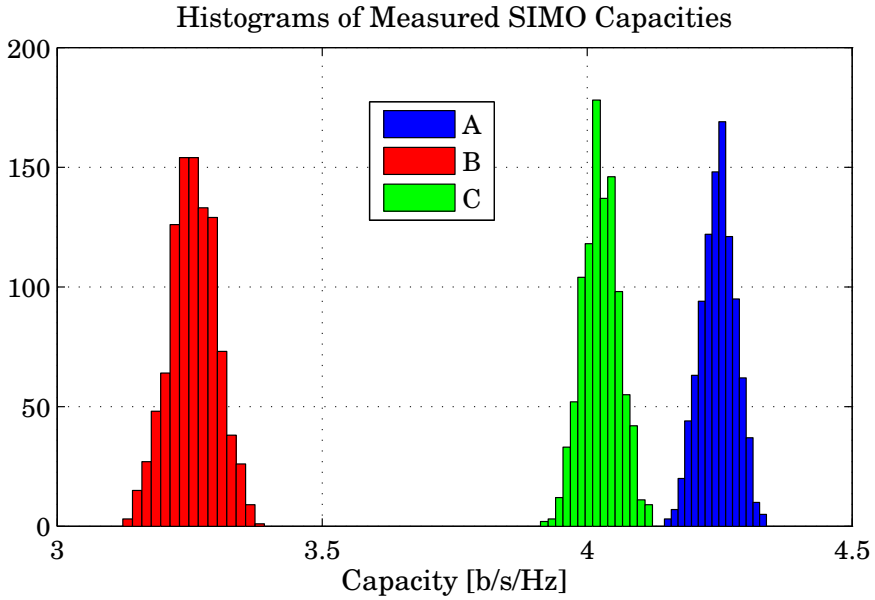

Figure 5.27: Histograms of the SIMO capacities for measurements of three different antenna configurations.

Next, the mean capacities by MEF and measurements are compared for $R = T = 2$ MIMO system. Results are plotted for side-by-side configurations in Figure 5.29, and for collinear agreements in in Figure 5.30. Again, very good agreement is observed between the proposed MEF and the measurement results with less than 9 percent absolute error.

Then, MEF is utilized to investigate the capacity of patch arrays in detail. Let $\delta = \Delta - W$ denote the distance between the closest edges of the patches of an array. For instance, for A1×2C, the distance between the feed points of the patch elements was given as $\Delta = 0.8\lambda$. Then for this array configuration δ becomes $\delta = (0.8 - 0.353)\lambda = 0.447\lambda$. We will use MEF to evaluate the MIMO capacities of printed patch arrays for 20 different δ values from 0.05λ to λ in the following part. However, the graphical results will be plotted against Δ, because it is the electrically meaningful distance.

Figure 5.31 shows the mean MIMO capacity results of 6 different patch array configurations, that is side-by-side and collinear agreement of patch antennas on three different substrates (A, B and C), versus the distance between feed

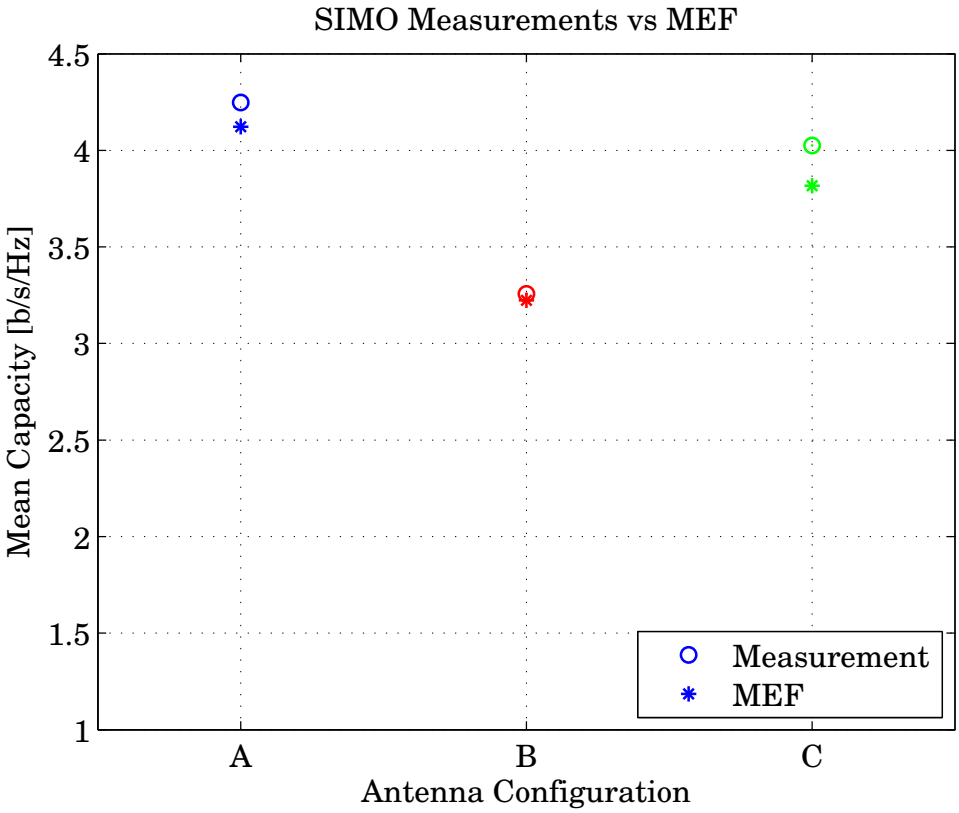

Figure 5.28: The comparison of the mean capacities by MEF and measurements.

points. Recalling the electrical properties of the substrates, it can be said that, A ($\epsilon_r = 3.0, d = 1.524$ mm) and B ($\epsilon_r = 3.2, d = 0.508$ mm) might be compared in terms of the substrate thickness, whereas inspecting A and C ($\epsilon_r = 4.5, d = 1.575$ mm) may indicate the effect of dielectric permittivity.

As concluded in Chapter 3, the thinner the substrate, the less the capacity, since the ground plane is closer to the antenna, and tends to cancel the effects due to the image theory. It is observed that, the maximum improvement by utilizing far apart patch antennas in an array can not exceed 1 b/s/Hz over very closely spaced ones. Therefore, for the design cases in which the physical size is limited, patch antennas can be located nearby.

For any kind of the substrate considered here, it is observed that, the side-by-side configuration performs slightly better (i.e., around 0.1 b/s/Hz) than the collinear one, since the side-by-side configuration cover a slightly large space.

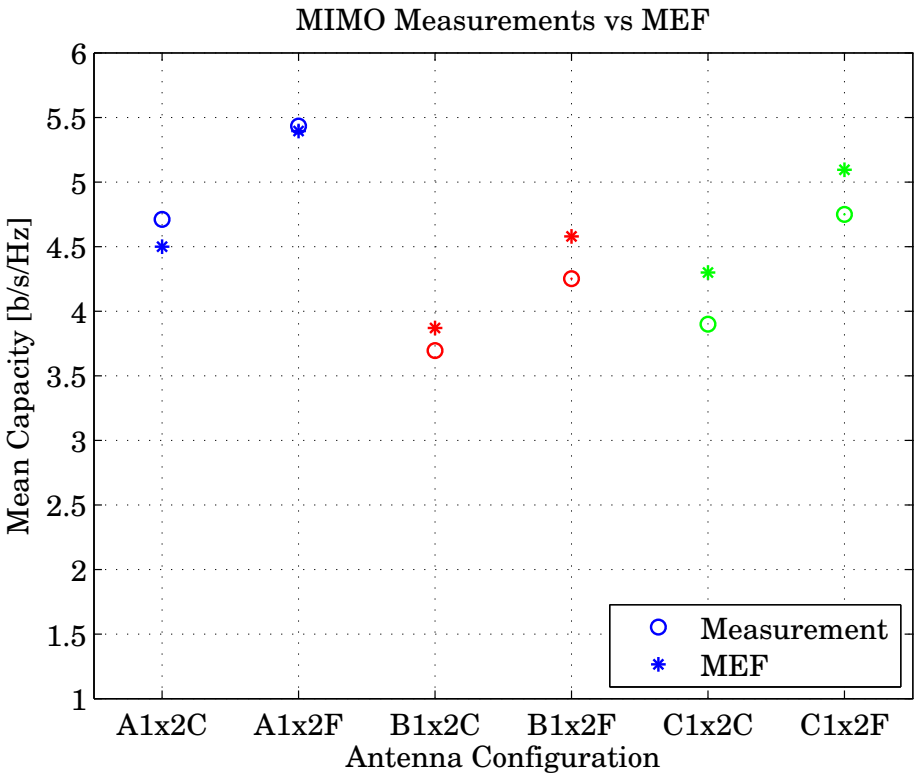

Figure 5.29: The MIMO capacities by MEF and measurements for side-by-side patches at TX.

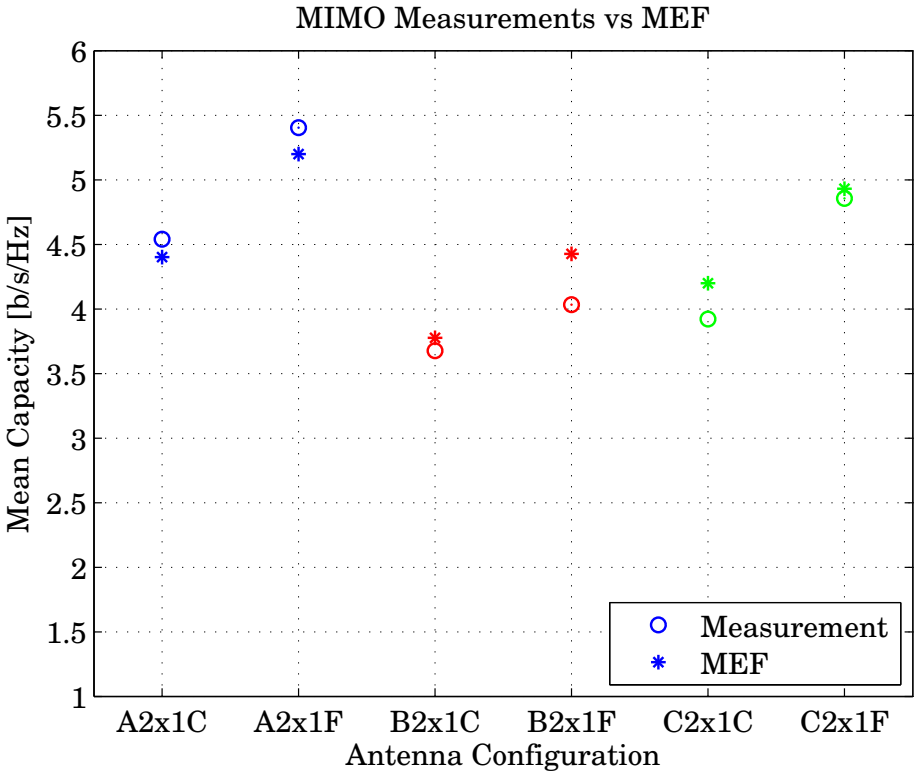

Figure 5.30: The MIMO capacities by MEF and measurements for collinear patches at TX.

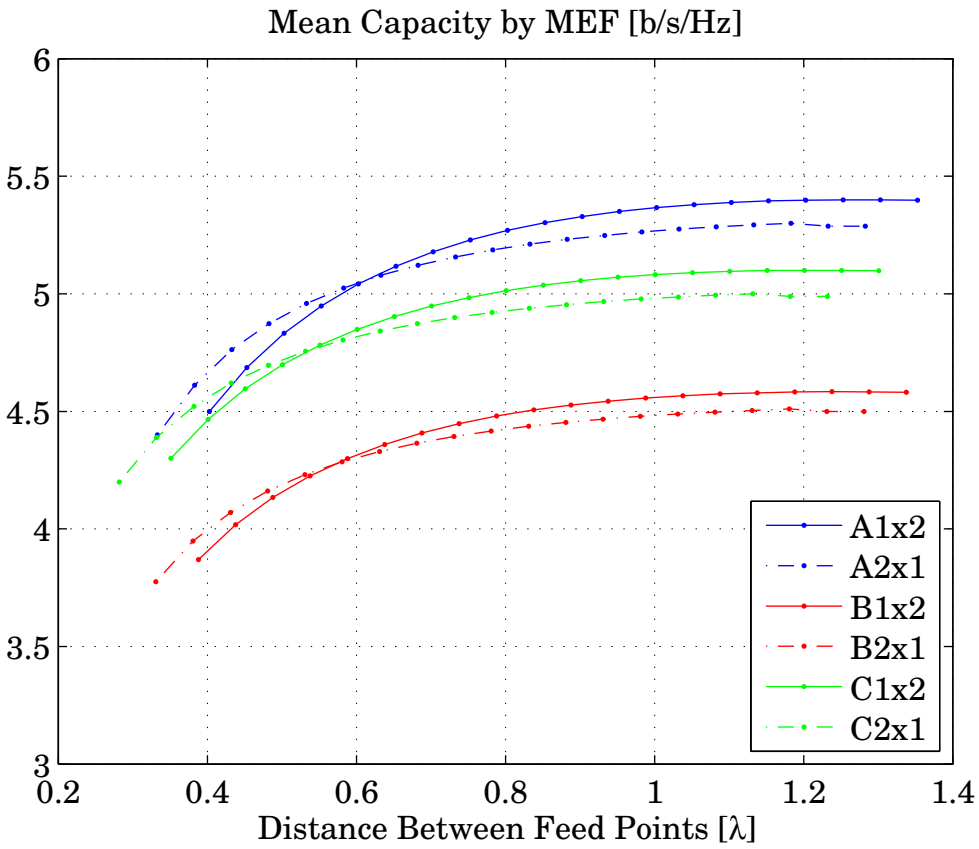

Figure 5.31: The MIMO capacity results of side-by-side and collinear agreement of patch antennas on three different substrates (A, B and C), versus the distance between feed points.

Printed patches here acts contrary to dipoles analyzed before that increasing ϵ_r does not increase the capacity. This may be because both the electrical and physical dimensions of antennas upon substrate B are the smallest ones among the others [96]. However, using smaller antennas can be advantageous. For instance, 3 closely spaced collinear patches on substrate B will occupy less space than 2 side-by-side patch antennas on substrates A and C, but yield better capacity. Note that, microstrip patch antennas are modeled by a cavity model as mentioned before. Since, the width of dipole elements is very small compared to patches, the cavity model is not suitable for microstrip dipoles. [96] also states the reason of the smaller capacity of thinner substrates in the cavity model context. Thinner substrates result in cavity models with higher quality factors, which decrease the radiation efficiency as the stored energy is increased.

5.7 Conclusions

MIMO performance of printed rectangular patch arrays is analyzed using a modified version of the full-wave channel model (MEF) given in Chapter 2. Various array configurations are designed, manufactured, and their MIMO performance is measured in an indoor environment. Very good agreement is achieved between the measurements and simulations by MEF. Effects of the electrical properties of printed patches on the MIMO capacity are explored in terms of the relative permittivity and thickness of the dielectric material.

Chapter 6

Numerical Determination of the MIMO Capacity Achieving Input Covariance

Telatar proved that [1] one should transmit equal powers along each of the transmit antennas to achieve the MIMO channel capacity, when the channel matrix is drawn independent and identically distributed (i.i.d.) from circularly symmetric Gaussian (c.s.g.) random variables. Since then, the capacity expression derived under this channel assumption is utilized frequently in the literature, whether the channel matrices investigated have i.i.d. c.s.g. entries or not.

Considering the fact that the real life channels are correlated, in this chapter, we consider the problem of computing the optimal input covariance matrix that achieves the capacity for three different types of transmitter arrays of isotropic radiators, uncoupled dipoles and coupled ones. We develop a numerical algorithm, based on the particle swarm optimization (PSO) along with our channel model with electric fields (MEF), that allows us to compute the capacity and the corresponding optimal input covariance.

It is shown that, moderate data rate improvement is possible for small antenna spacing values where the correlation is relatively high, mainly utilizing nearly full or full covariance matrices.

6.1 Optimal Transmission Scheme

As Shannon stated in the classical paper [97], the channel capacity in the presence of additive white Gaussian noise (AWGN) is given by

$$\mathcal{C} = \log_2(1+\rho) \tag{6.1}$$

where ρ is the received signal to noise ratio (SNR). Now let us consider a 2×2 MIMO system, in which the communication channels are defined from the transmitted voltages ($\bar{V}^{tx}$) to the received voltages ($\bar{V}^{rx}$) and expressed assuming flat fading by

$$\bar{V}^{rx} = \mathbf{H}\ \bar{V}^{tx} + \bar{n}. \tag{6.2}$$

For an sth random realization of the channel, (6.2) becomes

$$\bar{y} = \mathbf{H}_s\ \bar{x} + \bar{n}_s \tag{6.3}$$

where $\bar{n}_s$ represents the AWGN, $\bar{x}$ and $\bar{y}$ are the random vectors for the transmitted and received signals, respectively. Assuming unit noise variance (i.e., $\sigma_n^2 = 1$), the expected received SNR turns out to be

$$\rho = \mathcal{E}\left[\bar{y}^h \bar{y}\right] = \mathcal{E}\left[|y_1|^2 + |y_2|^2\right] \tag{6.4}$$

where $(.)^h$ and $\mathcal{E}(.)$ denotes the conjugate transpose and expectation operators, respectively. The received SNR by each branch can be written as

$$|y_i|^2 = (h_{ii}x_i + h_{ij}x_j)(h_{ii}^* x_i^* + h_{ij}^* x_j^*) \tag{6.5}$$

for $i = 1, 2$ and $(.)^*$ is conjugate operation. Then, the total SNR can be rewritten as

$$\rho = \mathcal{E}\left[\sum_{i=1}^{2} \left\{|x_i|^2(|h_{ii}|^2 + |h_{ji}|^2) + x_i x_j^*(h_{ii}h_{ij}^* + h_{ji}h_{jj}^*)\right\}\right]. \tag{6.6}$$

The argument of the logarithm in (6.1) then becomes

$$1+\rho=\left|\mathbf{I}_R+\mathbf{H}_s\mathbf{Q}\mathbf{H}_s^h\right| \tag{6.7}$$

where $|.|$ is the matrix determinant, $\mathbf{I}_R$ is the $R\times R$ identity matrix and $\mathbf{Q}$ is the input covariance matrix for sth channel realization, entries of which are given by

$$\mathbf{Q}=\mathcal{E}\left[\begin{array}{cc}|x_1|^2 & x_1x_2^* \\ x_1^*x_2 & |x_2|^2\end{array}\right]=\mathcal{E}\left[\bar{x}\bar{x}^h\right]. \tag{6.8}$$

The maximum amount of the data to be reliably transmitted (i.e., the channel capacity) can be expressed as

$$\mathcal{C}=\max_{\substack{\mathbf{Q}\geq 0\\ \mathrm{Tr}(\mathbf{Q})\leq\rho_T}}\left\{\mathcal{E}\left[\log_2\left(\left|\mathbf{I}_R+\mathbf{H}\mathbf{Q}\mathbf{H}^h\right|\right)\right]\right\} \tag{6.9}$$

where $\rho_{_T}$ denotes the total transmit SNR and Tr(.) is the trace operator.

Note that, $\mathbf{H}$ is the random matrix, the sth independent realization of which corresponds to $\mathbf{H}_s$. Furthermore, there is a power constraint on the input covariance such that $\mathrm{Tr}(\mathbf{Q})=\mathcal{E}[\bar{x}^h\bar{x}]\leq\rho_{_T}$.

Telatar proved in [1] that, the optimal input covariance happens to be

$$\mathbf{Q}_{csg}=\frac{\rho_{_T}}{T}\ \mathbf{I}_T \tag{6.10}$$

when $\mathbf{H}$ is drawn independent and identically distributed (i.i.d.) from circularly symmetric Gaussian (c.s.g.) random variables. In this very case, the capacity is expressed as

$$\mathcal{C}=\mathcal{E}\left[\log_2\left(\left|\mathbf{I}_R+\frac{\rho_{_T}}{T}\ \mathbf{H}\mathbf{H}^h\right|\right)\right]. \tag{6.11}$$

This capacity expression in (6.11) is utilized frequently in the literature, whether the channel matrices investigated have i.i.d. c.s.g. entries or not.

Considering the fact that, the real life channels are correlated, our purpose in this work is to numerically find out the optimal transmission covariance matrices, when TX array is formed by (i) isotropic radiators, (ii) uncoupled dipoles,

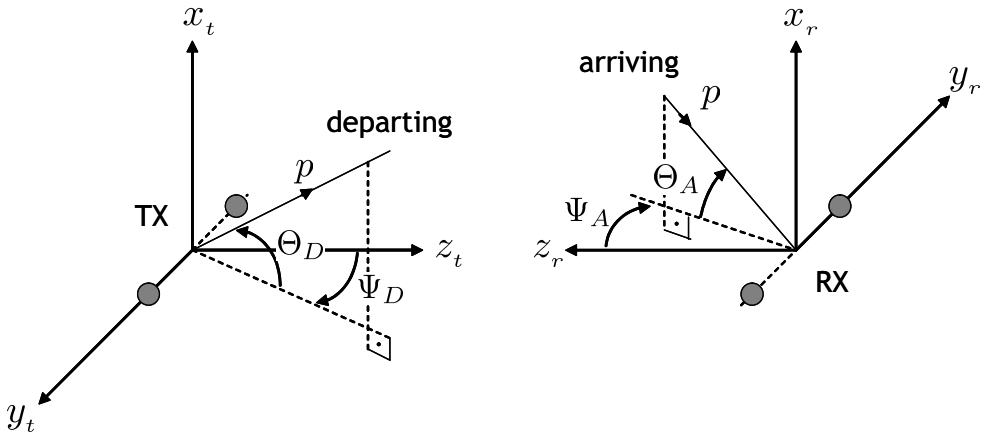

Figure 6.1: Representation of the 3D multipath environment with TX and RX arrays.

and (*iii*) coupled dipoles; for varying interelement spacing. For this aim, a geometrical multipath scenario and our channel model with electric fields (MEF) formulations will be used along with a powerful optimization algorithm, that is the particle swarm optimization (PSO).

6.2 The Multipath Scenario

The multipath environment in this chapter is a 3D geometrical model which includes multi-bounce scattering as shown in Figure 6.1. It is very similar to the one given in Chapter 5. The propagation paths are defined by the angle of departure (AoD), Ω_D, angle of arrival (AoA), Ω_A, the delay component, τ, and 2×2 cross polarized scattering coefficient matrix. All these parameters except the delay components are chosen the same as the ones in Chapter 5.

Over N_R scenario realizations, the delay components are evaluated with an exponential distribution having a delay spread of $\sigma_\tau = 30$ ns as

$$\tau = -\sigma_\tau \ln(\mathcal{U}), \tag{6.12}$$

where $\mathcal{U}$ is drawn from the uniform distribution on the unit interval $(0, 1]$. Since the entries of the cross polarized scattering coefficient matrix are chosen to be

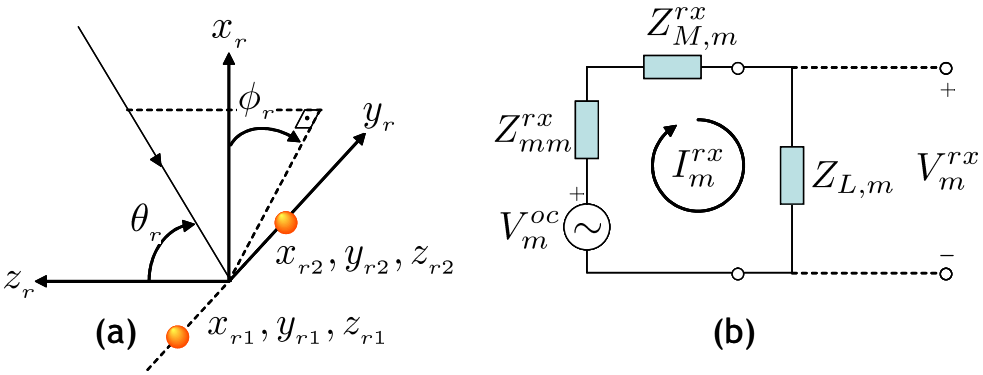

Figure 6.2: RX array (a) geometry (b) circuit model.

independent and identically-distributed (i.i.d.) complex Gaussian random variables of zero mean and unit variance, we will have an exponential delay profile.

6.3 Evaluation of the Channel Matrix

In this section, the formulation for the evaluation of the entries of the $R \times T$ MIMO channel matrix ($\mathbf{H}$) will be given, where R and T are the number of antenna elements in TX and RX arrays, respectively. Assuming flat fading, the received signal vector, $\bar{V}^{rx}$, can be written in terms of the transmitted one, $\bar{V}^{tx}$, and the additive white Gaussian noise vector, $\bar{n}$, i.i.d. elements with zero mean and unit variance as

$$\bar{V}^{rx} = \mathbf{H}\ \bar{V}^{tx} + \bar{n}. \tag{6.13}$$

For the sake of simplicity, and without loss of generality, both R and T are taken as $R = T = 2$ in this work. Now let us have a deeper look at the RX and TX array configurations utilized throughout this study.

6.3.1 The Receiver Array

The receiver array is considered to be formed by two isotropic radiators. The geometry of the array is given in Figure 6.2 (a), and the circuit model for mth

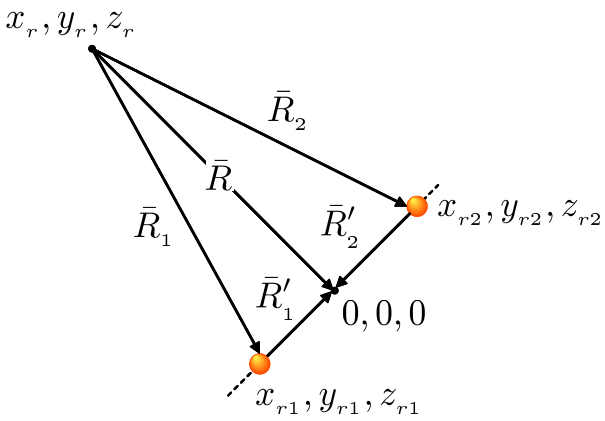

Figure 6.3: RX array geometry in detail.

radiator is assumed as illustrated in Figure 6.2 (b), where $m = 1, 2$. In Figure 6.2, (θ_r, ϕ_r) are the elevation and azimuth angles for the arrival direction in the spherical coordinate system, origin of which coincides with the center of the RX array. For the mth radiator, Z^{rx}_{mm} is the antenna impedance; $Z_{L,m}$ denotes the load impedance, which is taken as 50Ω; $Z^{rx}_{M,m}$ is the matching impedance. Assuming conjugate matching, $Z^{rx}_{M,m}$ is chosen to ensure the following relation:

$$Z_{L,m} = Z^{rx}_{M,m} + Z^{rx}_{mm} = 50\Omega. \tag{6.14}$$

V^{oc}_m is the induced voltage, expression of which is given by

$$V^{oc}_m = \bar{E}^{rx}_m \cdot \bar{l}^e \tag{6.15}$$

recalling the concept of the vector effective length in Chapter 5. In (6.15), $\bar{E}^{rx}_m$ is the incident electric field on the mth RX element, and $\bar{l}^e$ is the vector effective length [79] of it.

Inspecting the RX array geometry in detail, as in Figure 6.3, we can note the following for the received electric fields: Suppose an electric field originated from the point $P(x_r, y_r, z_r)$ is arriving at the origin of the coordinate system, which coincides with the center of the RX array. Let any component of this field can be expressed by

$$E^{rx}_0 = E_0 \frac{e^{-jkR}}{R}, \tag{6.16}$$

where k is the freespace wave number, and R is the magnitude of the position vector $(-\bar{R})$ pointing P, which is in the far zone of the RX array. Then the incident field on the mth RX element can be given by

$$E_m^{rx} = E_0 \frac{e^{-jkR_m}}{R_m} \approx E_0 \frac{e^{-jkR_m}}{R}, \tag{6.17}$$

since $R >> R'_m$, where R'_m is the magnitude of the position vector $(-\bar{R}'_m)$ pointing the mth RX antenna; and, R_m is that of $\bar{R}-\bar{R}'_m$, namely the distance between P and the antenna. For the accurate evaluation of the phase terms, the approximation $(R >> R'_m)$ is not adequate. Instead, the operations in (6.18)-(6.20) are utilized.

$$\begin{aligned} R_m &= \sqrt{(x_r - x_{rm})^2 + (y_r - y_{rm})^2 + (z_r - z_{rm})^2} && (6.18) \\ &= \sqrt{x_r^2 + y_r^2 + z_r^2 + x_{rm}^2 + y_{rm}^2 + z_{rm}^2 - 2x_r x_{rm} - 2y_r y_{rm} - 2z_r z_{rm}} \\ &= R\sqrt{1 + \frac{(R'_m)^2}{R^2} - \frac{2x_r x_{rm}}{R^2} - \frac{2y_r y_{rm}}{R^2} - \frac{2z_r z_{rm}}{R^2}} \\ &\approx R\sqrt{1 - 2\,\frac{x_r x_{rm} + y_r y_{rm} + z_r z_{rm}}{R^2}}, && (6.19) \end{aligned}$$

since $R^2 >> (R'_m)^2$, where (x_{rm}, y_{rm}, z_{rm}) is the coordinates of the mth antenna in the same Cartesian system. The Taylor expansion of the square-root in (6.19) till the second order terms $\left[\left(\frac{R'_m}{R}\right)^q \approx 0,\ \text{for } q \geq 2\right]$ yields,

$$\begin{aligned} R_m &\approx R - x_{rm}\frac{x_r}{R} - y_{rm}\frac{y_r}{R} - z_{rm}\frac{z_r}{R} \\ &= R - x_{rm}\sin\theta_r\cos\phi_r - y_{rm}\sin\theta_r\sin\phi_r - z_{rm}\cos\theta_r. && (6.20) \end{aligned}$$

Then, E_m^{rx} turns out to be

$$E_m^{rx} = E_0^{rx} e^{jk_{rx}x_{rm}} e^{jk_{ry}y_{rm}} e^{jk_{rz}z_{rm}}, \tag{6.21}$$

where $k_{rx} = k\sin\theta_r\cos\phi_r$, $k_{ry} = k\sin\theta_r\sin\phi_r$ and $k_{rz} = k\cos\theta_r$.

The vector effective length of an antenna is defined in [79] as:

$$\bar{l}^e = \frac{\bar{E}_{rad}(1\text{A})}{-j30k\frac{e^{-jkR}}{R}}, \tag{6.22}$$

where $\bar{E}_{rad}(1\text{A})$ is the radiation electric field of the antenna under unit current applied at the antenna port. In this work, the radiated electric field of the isotropic radiator (when unit current applied) is assumed to be

$$\bar{E}_{rad}^{isot}(1\text{A}) = (-\hat{a}_\theta + \hat{a}_\phi)\ j60\frac{e^{-jkR}}{R}, \tag{6.23}$$

in order to be convenient with the dipoles at the TX array to be discussed in detail later. Hence, the vector effective length of the isotropic radiator becomes

$$\bar{l}^{isot} = (-\hat{a}_\theta + \hat{a}_\phi)\ \frac{2}{k}. \tag{6.24}$$

Then, the induced voltage on the mth isotropic radiator can be expressed as

$$\begin{aligned} V_m^{oc} &= E_{m,\theta}^{rx}\ l_\theta^{isot} + E_{m,\phi}^{rx}\ l_\phi^{isot} \\ &= \frac{2}{k}\ e^{j(k_{rx}x_{rm}+k_{ry}y_{rm}+k_{rz}z_{rm})}\left(-E_{0,\theta}^{rx} + E_{0,\phi}^{rx}\right), \end{aligned} \tag{6.25}$$

and the received voltage (i.e., voltage on the mth load impedance) becomes,

$$V_m^{rx} = Z_{L,m}\ \frac{V_m^{oc}}{Z_{L,m} + Z_{M,m}^{rx} + Z_{mm}^{rx}} = \frac{V_m^{oc}}{2}, \tag{6.26}$$

utilizing the circuit model in Figure 6.2 (b) and due to the choice of the load impedances and conjugate matching assumption in this work. Note that, the circuit model for the mth RX element does not include the effect of mutual coupling, since the RX elements are isotropic radiators.

The field components incident on the center of the RX array are given by the superposition of arriving fields from each propagation path as

$$E_{0,\theta,\phi}^{rx} = \sum_{p=1}^{S} E_{p,\theta,\phi}^{scat}\ e^{-jkc\tau_p}, \tag{6.27}$$

where S is the total number of paths in each of the N_R channel realizations, c is the speed of light in freespace, τ_p is the delay component of the pth propagation path, and

$$\begin{bmatrix} E_{p,\theta}^{scat} \\ E_{p,\phi}^{scat} \end{bmatrix} = \begin{bmatrix} \alpha_p^{\theta\theta} & \alpha_p^{\theta\phi} \\ \alpha_p^{\phi\theta} & \alpha_p^{\phi\phi} \end{bmatrix} \begin{bmatrix} E_{p,\theta}^{tx} \\ E_{p,\phi}^{tx} \end{bmatrix}. \tag{6.28}$$

In (6.28), $E_{p,\theta,\phi}^{tx}$ are the field components transmitted from the TX array in the departure direction of pth propagation path. Now, let us examine these fields via the TX array configurations adopted in this study.

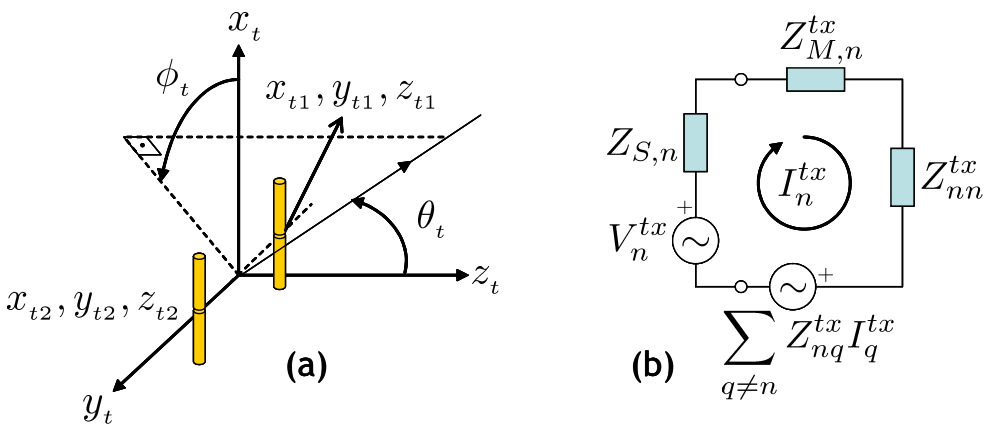

Figure 6.4: TX array (a) geometry (b) circuit model.

6.3.2 The Transmitter Array

Three different TX array configurations, the optimal transmission schemes of which to be investigated, are chosen in this chapter. These are TX arrays of

- coupled dipole elements,
- uncoupled dipole elements,
- isotropic radiators.

TX Array of Coupled Dipole Elements

Equations (6.25)-(6.28) relate the received voltages (V^{rx}_m) with the transmitted field in the direction of AoD for each propagation path. Thus, if we associate the transmitted voltages (V^{tx}_n) with the fields radiated by TX, we can simply evaluate the channel responses. For this purpose, the geometry and circuit model of the nth transmit antenna as illustrated in Figure 6.4 (a) and (b) are considered. In Figure 6.4, (θ_t, ϕ_t) are the elevation and azimuth angles for the departure direction in the spherical coordinate system, origin of which coincides with the center of the TX array; and, (x_{tn}, y_{tn}, z_{tn}) is the coordinate of the nth dipole antenna in its Cartesian equivalent, where $n = 1, 2$. The dipoles in this work are

supposed to be identical with $\lambda/2$ length and $\lambda/200$ radius. For the nth dipole, Z_{nn}^{tx} is the self impedance; $Z_{S,n}$ denotes the source impedance, which is taken as 50Ω; $Z_{M,n}^{tx}$ is the matching impedance. Assuming conjugate matching, $Z_{M,n}^{tx}$ is chosen to ensure the following relation:

$$Z_{S,n} = Z_{M,n}^{tx} + Z_{nn}^{tx} = 50\Omega. \tag{6.29}$$

Note that, the effect of mutual coupling due to other array elements ($q \neq n$) is modeled by the term $\sum_{q \neq n} Z_{nq}^{tx} I_q^{tx}$, where Z_{nq}^{tx} denotes the mutual impedance between the nth and qth dipole elements; and, I_q^{tx} is the magnitude of induced current on the qth dipole antenna.

Following the MEF process, we first evaluate the mutual interactions matrix ($\mathbf{Z}^{tx}$) by using the analytical expressions for self terms (Z_{nn}^{tx}) in [79] and for off-diagonal ones (Z_{nq}^{tx}) in [80]. Then, we activate the first dipole element at TX (i.e., $n = 1$), such that $V_n^{tx} = 1\text{V}$ and $V_q^{tx} = 0\text{V}$. Having $\mathbf{Z}^{tx}$, the current vector ($\bar{I}^{tx}$) containing both the impressed current at the port of the activated dipole (I_n^{tx}) and the induced ones due to mutual coupling (I_p^{tx}) can be found by the following matrix equation:

$$\bar{I}^{tx} = \left[\mathbf{Z}^{tx} + \mathbf{Z}_S + \mathbf{Z}_M^{tx}\right]^{-1} \bar{V}^{tx}, \tag{6.30}$$

where $\mathbf{Z}_S$ and $\mathbf{Z}_M^{tx}$ are the diagonal matrices, entries of which are the source and matching impedances, respectively. It is obvious that, the radiated field by the TX array depends on both the impressed current and induced ones due to coupling, and hence, a superposition is needed. Assuming piecewise sinusoidal currents on dipole elements, the current density can be expressed in terms of $\bar{I}^{tx}$ as,

$$\bar{J} = \hat{a}_x \sum_{\nu=1}^{T} I_\nu^{tx} \sin(k|h_\nu - x'_\nu|)\ \delta(y_{t\nu}, z_{t\nu}), \tag{6.31}$$

where $h_\nu = \lambda/4$ are the half lengths of the dipoles, x'_ν are defined in the intervals $[-h_\nu, h_\nu]$, and $\delta(.)$ is the Dirac delta function. Hence, the radiated electric field

by the TX array in the far zone can be found by the radiation integral below:

$$\bar{E}^{tx} = \frac{-j\omega\mu}{4\pi} \int_V \bar{J} \, \frac{e^{-jkR}}{R} dV'. \tag{6.32}$$

Substituting (6.31) into (6.32), the volume integral reduces to a line integral over dx'_ν and it can be simply evaluated for a single dipole at the origin. For the deviated ones, via similar approximations to (6.17)-(6.20), θ and ϕ components of the mutual coupling included radiated electric field by the TX array in (θ_t, ϕ_t) direction can be written as,

$$E^{tx}_\theta = -j60 \cos\theta_t \cos\phi_t \sum_{\nu=1}^{T} I^{tx}_\nu f_\nu(\theta_t, \phi_t) \; e^{j(k_{tx}x_{t\nu} + k_{ty}y_{t\nu} + k_{tz}z_{t\nu})} \tag{6.33}$$

$$E^{tx}_\phi = j60 \sin\phi_t \sum_{\nu=1}^{T} I^{tx}_\nu f_\nu(\theta_t, \phi_t) \; e^{j(k_{tx}x_{t\nu} + k_{ty}y_{t\nu} + k_{tz}z_{t\nu})} \tag{6.34}$$

where

$$f_\nu(\theta_t, \phi_t) = \frac{\cos(k_{tx}h_\nu) - \cos(kh_\nu)}{1 - \sin^2\theta_t \cos^2\phi_t}, \tag{6.35}$$

and $k_{tx} = k\sin\theta_t\cos\phi_t$, $k_{ty} = k\sin\theta_t\sin\phi_t$ and $k_{tz} = k\cos\theta_t$. Note that, all $1/R$ terms are eliminated from the final expressions, since path loss effects are embedded into the model during the generation of delay components for an exponential power delay profile in (6.12). Similarly, e^{-jkR} are hidden in the $e^{-jkc\tau_p}$ term of (6.27) for each propagation path.

Associating the radiated fields of TX array with equations (6.25)-(6.28), the received voltages (V^{rx}_m) are found for the first TX antenna is active ($V^{tx}_n = 1V$, $V^{tx}_{q\neq n} = 0$, $n = 1$). Hence, the first column of the channel coefficients matrix is evaluated, since

$$h_{mn} = \left.\frac{V^{rx}_m}{V^{tx}_n}\right|_{V^{tx}_{q\neq n}=0}. \tag{6.36}$$

For the evaluation of the other columns, n is increased and the operations in (6.30), (6.33)-(6.34), (6.25)-(6.28) are followed recursively till $n = T$.

TX Array of Uncoupled Dipole Elements

In order to obtain the channel matrix entries for a case that mutual coupling is neglected in the TX array, simply, the off-diagonal terms (Z_{tx}^{nq}) in (6.30) are taken as zero, and the aforementioned procedure is followed. Note that, in this case, the current vector has only one non-zero element that is the impressed current on the activated antenna, and the other elements representing the induced currents due to mutual coupling become zero. Thus the summations in (6.30), (6.33)-(6.34) are reduced to single expressions for the very activated (nth) dipole, therefore, the radiated field expressions turn into

$$E_{\theta}^{tx} = -j60 \cos\theta_t \cos\phi_t I_n^{tx} f_n(\theta_t, \phi_t)\ e^{j(k_{tx}x_{tn}+k_{ty}y_{tn}+k_{tz}z_{tn})} \tag{6.37}$$

$$E_{\phi}^{tx} = j60 \sin\phi_t I_n^{tx} f_n(\theta_t, \phi_t)\ e^{j(k_{tx}x_{tn}+k_{ty}y_{tn}+k_{tz}z_{tn})}. \tag{6.38}$$

TX Array of Isotropic Radiators

The procedure for the evaluation of the channel matrix when TX array is formed by isotropic radiators is very similar to the one in the previous case, since mutual coupling is absent, as well. In addition, the radiated fields by the TX array lose the dependency to the direction, and hence, (6.33)-(6.34) become

$$E_{\theta}^{tx} = -j60 I_n^{tx} e^{j(k_{tx}x_{tn}+k_{ty}y_{tn}+k_{tz}z_{tn})} \tag{6.39}$$

$$E_{\phi}^{tx} = j60 I_n^{tx} e^{j(k_{tx}x_{tn}+k_{ty}y_{tn}+k_{tz}z_{tn})} \tag{6.40}$$

for the activated radiator.

6.4 Numerical Results

In this section, the numerical results on the evaluation of optimal transmission schemes for different array types are presented. First, the validation of PSO will be given. Then, the other findings will be presented.

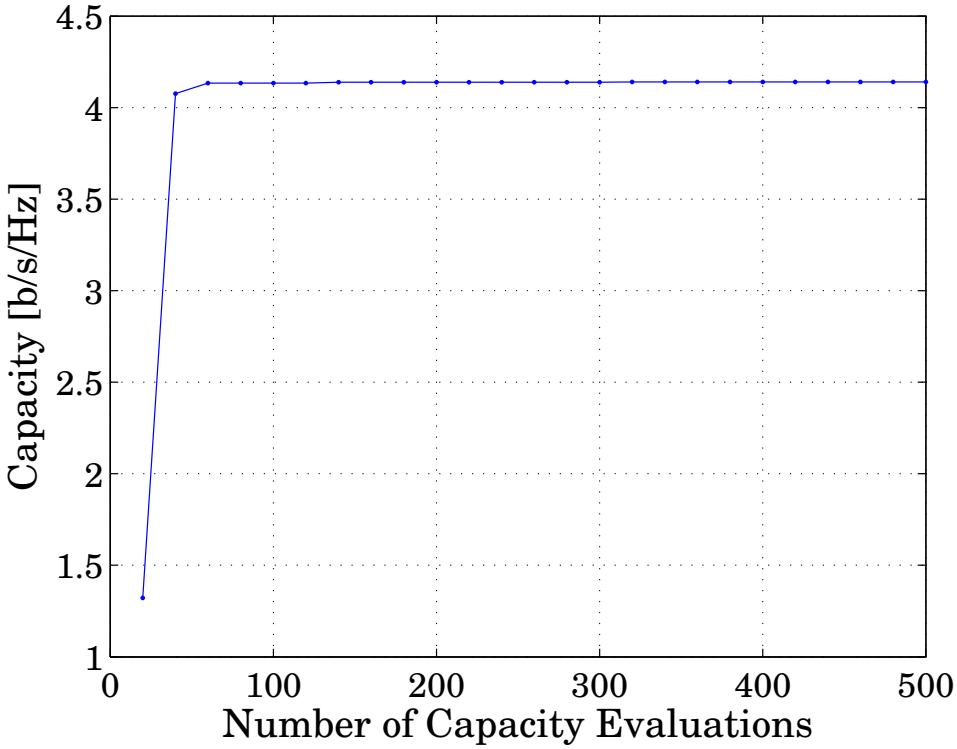

Figure 6.5: Validation of PSO for i.i.d. c.s.g channel. PSO finds the optimum solution of the input covariance (diagonal $\mathbf{Q}_{csg}$) for capacity in less than 500 evaluations.

6.4.1 Validation of PSO

For the assessment of the accuracy of PSO, a 2×2 MIMO system with channel matrices having i.i.d. c.s.g. characteristic is considered. $\mathbf{H}_s$ matrices are generated for 1000 channel realizations and PSO is allowed to find the optimum input covariance matrix by trying to solve the optimization problem given in (6.9). For this purpose, PSO searched a solution space of four unknowns, such that $Q_{11} = \mathcal{E}[|x_1|^2]$, $Q_{22} = \mathcal{E}[|x_2|^2]$, $|Q_{12}| = \mathcal{E}[|x_1 x_2^*|]$ and $\Phi_{12} = \mathcal{E}[\angle(x_1 x_2^*)]$.

Setting the fixed transmit SNR at $\rho_{_T} = 10$ dB and the number of particles in the population as 20, PSO finds the capacity achieving covariance matrix (starting from a random initialization of the population, as shown in Figure 6.5) in less than 500 evaluations as $Q_{11} = 0.5\rho_{_T}$, $Q_{22} = 0.5\rho_{_T}$ and $|Q_{12}| = 0$, which

yields

$$\mathbf{Q}_{opt} = \mathbf{Q}_{csg} = \frac{\rho_T}{T}\,\mathbf{I}_T. \tag{6.41}$$

Occasionally, particles pass beyond the boundaries of given solution space, hence adoption of a boundary policy to the algorithm is essential [89]. In order to enforce particles to search inside the solution space of interest, the invisible wall technique suits our application best and therefore is used in this study. In the invisible wall technique, particles are allowed to fly outside the allowable solution space ($\mathrm{Tr}(\mathbf{Q}) > \rho_T$), but assigned zero fitness values. Eventually, the particles are expected to return to the solution space since fitness values (i.e., the data rate values evaluated for cases represented by each particle) are larger inside the allowed space. Other details on the PSO algorithm can be found in Chapter 4.

As the accuracy of PSO is verified, we can proceed to obtain the optimal input covariance matrices for different types of antenna arrays.

6.4.2 The Optimal Input Covariance for Various Array Configurations

In this section, the transmission schemes to compute the MIMO channel capacity are obtained numerically via PSO for transmitter antenna arrays of isotropic radiators, uncoupled dipoles and coupled ones.

First, 1000 multipath scenarios are generated as described in Section 6.2, and kept in the memory. Then, for a selected interelement spacing, the channel matrix and data rate are obtained in an *evaluation*. PSO manages these evaluations iteratively, in order to find the optimal input covariance matrix for maximized data rate (i.e., the capacity).

Figure 6.6 and 6.7 illustrate the obtained $\mathbf{Q}_{opt}$ matrix entries for 20 different antenna spacing values varying from 0.05λ to λ, where λ is the free space wavelength. The transmit SNR is set to 20 dB and fixed. Inspecting Figure 6.6, it can be observed that, $Q_{11} \approx 1 - Q_{22} \approx 0.5\rho_{_T}$ for the diagonal entries of the optimal covariance matrix for all different antenna spacing values. Figure 6.7 shows the off-diagonal elements. The phase term of Q_{12} is significantly small for all interelement spacings, yielding dominant real off-diagonal entries. The magnitude of Q_{12} is $0.5\rho_{_T}$ for small spacing values in the isotropic radiator and uncoupled dipole cases, resulting in full covariance. For these cases, as the element spacing increases, the covariance matrix tends to take a diagonal form, for which the use of Q_{csg} and hence the expression in (6.11) for the evaluation of the capacity is more valid.

In the coupled dipoles case, the optimal Q_{12} shows a different behavior. Especially for the typical 0.5λ spaced dipoles, almost a full-covariance input scheme is the optimal one for high capacity. Coupled dipoles need less input correlation than the other two types for small dipole spacings, and more correlation at larger distances up to λ.

Achievable rates obtained via the optimum and diagonal (i.e., $\mathbf{Q}_{csg}$) input schemes are compared in Figure 6.8. In Figure 6.8 (a) the rate curves obtained via both $\mathbf{Q}_{opt}$ and $\mathbf{Q}_{csg}$ are plotted for the three types of transmitter arrays. It should be noted that, for antenna distances between 0.4 and 0.9λ, mutual coupling is beneficial to the channel energy because of the directional scattering conditions and the receiver array is oriented orthogonally to the main direction of arrival, as stated by Clerckx *et al.* in [98]. For the deeper investigation of the rate improvement using the optimal input covariance instead of the diagonal one, the differences are plotted in Figure 6.8 (b). It is observed that, data rate improvement up to 1 bit is possible for all types of antennas using the optimal

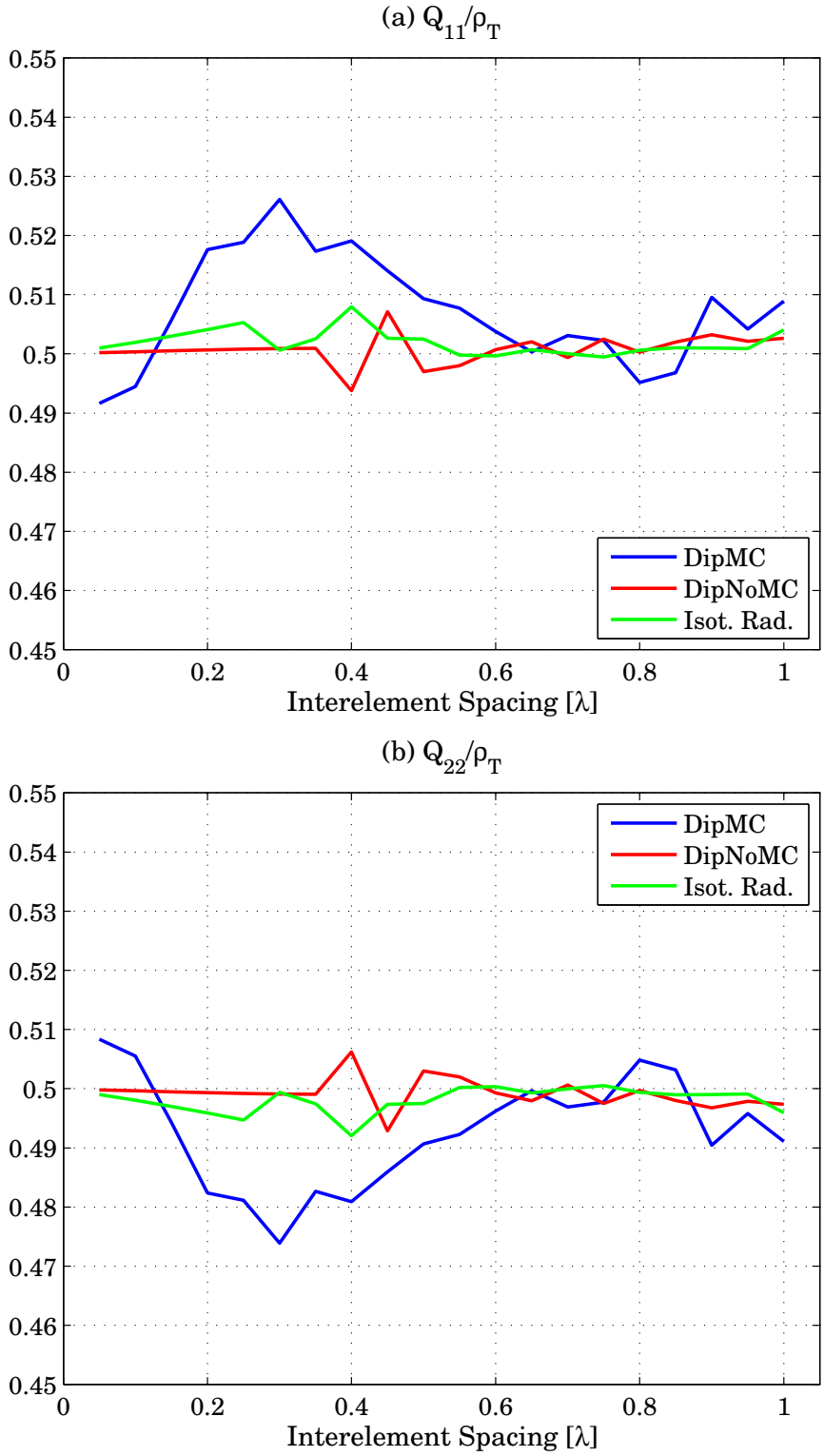

Figure 6.6: Optimal input covariance matrix entries. (a) Q_{11}/ρ_T. (b) Q_{22}/ρ_T. $\rho_T = 20$dB.

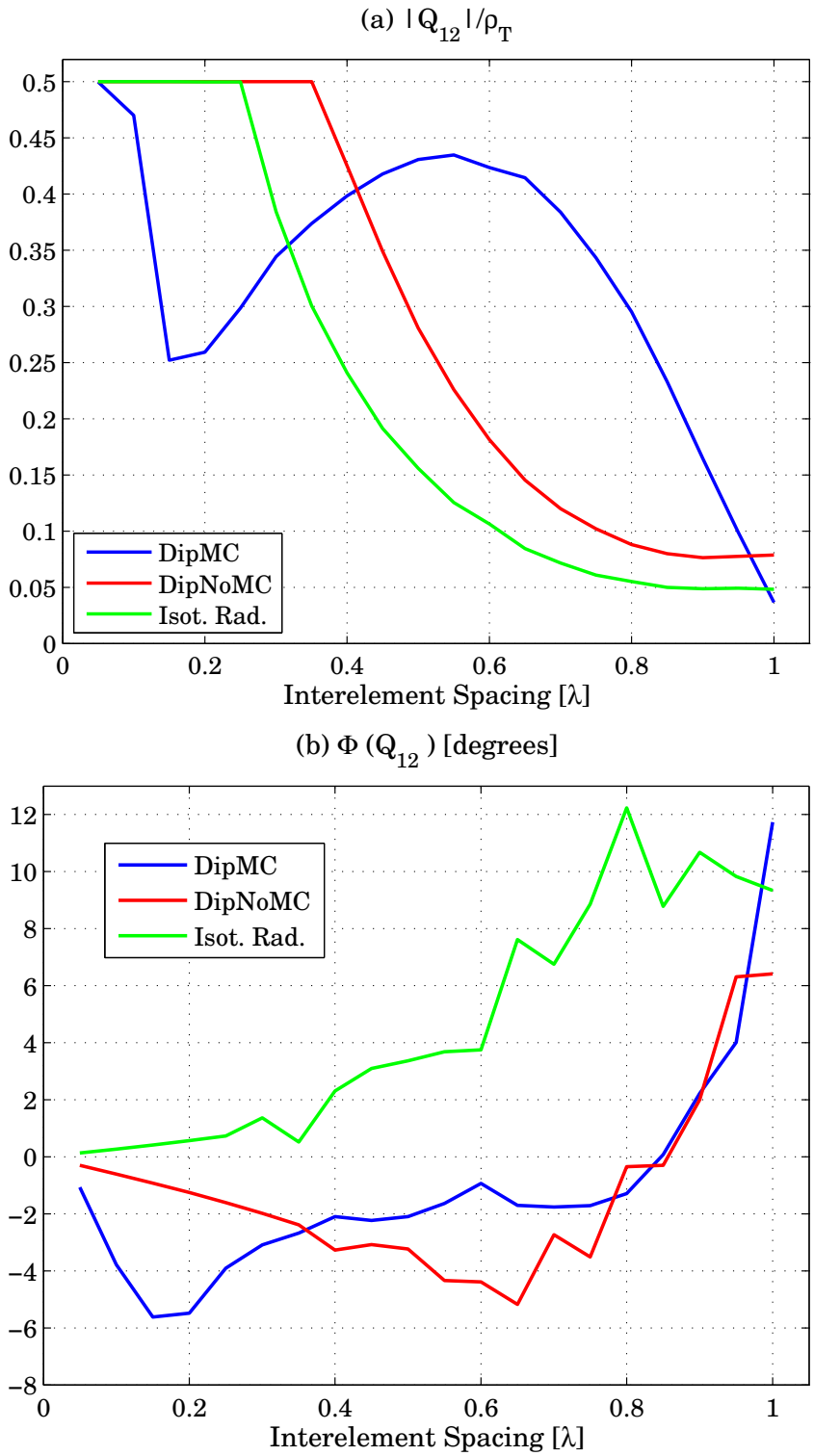

Figure 6.7: Optimal input covariance matrix entries. (a) Magnitude of Q_{12}/ρ_T. (b) Phase of Q_{12}. $\rho_T = 20$dB.

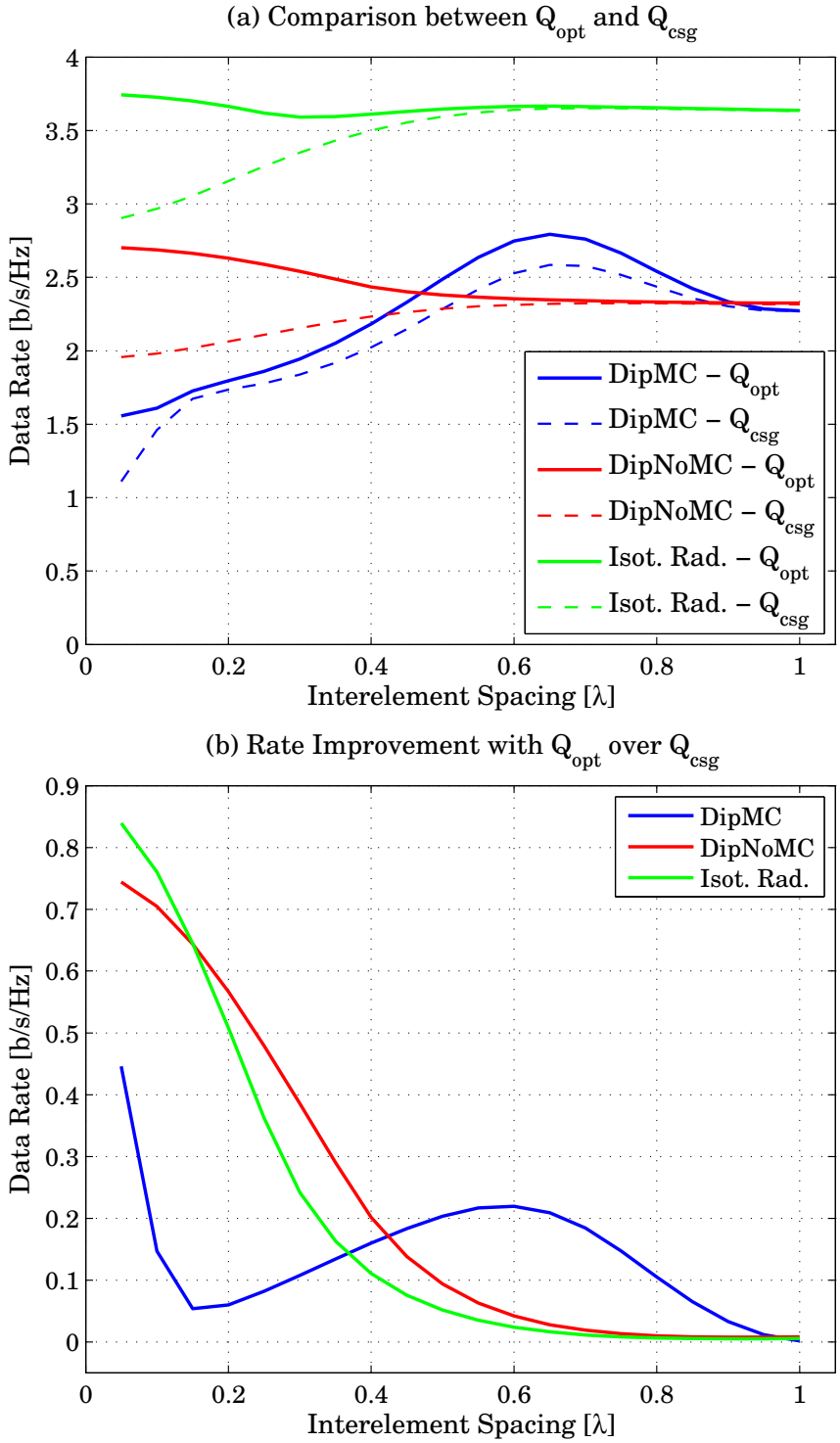

Figure 6.8: (a) Data rate curves obtained via $\mathbf{Q}_{opt}$ and $\mathbf{Q}_{csg}$. (b) Rate improvement with $\mathbf{Q}_{opt}$ over $\mathbf{Q}_{csg}$. $\rho_T = 20$dB.

input schemes. For the coupled dipoles, improvement is available at very small antenna spacings and at the typical 0.5λ distance.

The channel correlation is given by

$$\rho_{_h} = \left| \frac{\mathcal{E}\left[h_{11}h_{12}^{*}\right]}{\sqrt{\mathcal{E}\left[|h_{11}|^2\right]\ \mathcal{E}\left[|h_{22}|^2\right]}} \right| \tag{6.42}$$

and plotted versus interelement spacing values for the isotropic radiators, uncoupled and coupled dipoles in Figure 6.9 (a). The slight difference of uncoupled dipoles from isotropic radiators is due to the anisotropic behavior in the elevation plane.

Another correlation coefficient for the optimal transmission scheme is defined as

$$\rho_{_{12}} = \left| \frac{Q_{12}}{\sqrt{Q_{11}Q_{22}}} \right|. \tag{6.43}$$

Results versus interelement spacing is illustrated in Figure 6.9 (b), in the cases $\rho_{_T} = 20$ dB and 27 dB. It is observed again that, for achieving the channel capacity, highly correlated input schemes should be used, when the channel correlation is relatively large.

For the coupled dipoles, correlation curves are very similar to the ones in [98], and also, they resemble the curves in the improvement graph [Figure 6.8 (b)]. Namely, it is possible to improve rates beyond that obtained with uncorrelated inputs with equal power allocation by using the optimal covariance, when the channel correlation is relatively large.

PSO is let to find the optimal input covariance for increased transmit SNR, $\rho_{_T} = 27$ dB, as well. The data rate comparison and improvement via the use of $\mathbf{Q}_{opt}$ are given in Figure 6.10. Results for the entries of the covariance matrix are given in Figure 6.11. The curves are similar in shape to the ones for $\rho_{_T} = 10$ dB case, though the decay towards the elements of the diagonal covariance is more rapid. It is observed that, under increased SNR, the optimal transmission

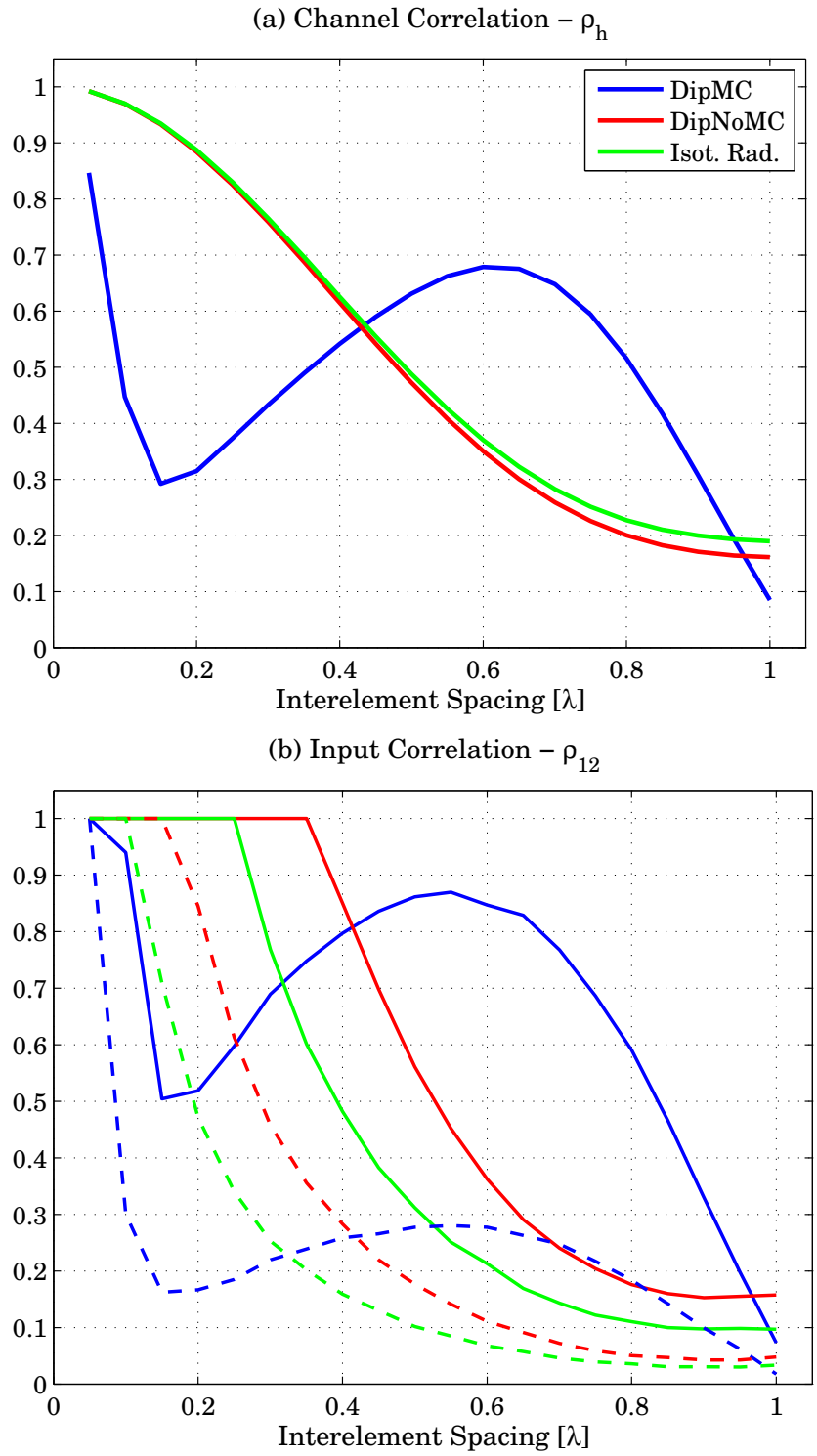

Figure 6.9: Correlation coefficients. (a) Channel correlation, ρ_h given by (6.42). (b) Input correlation, ρ_{12} given by (6.43). Solid lines represent $\rho_T = 20$ dB, dashed ones for $\rho_T = 27$ dB.

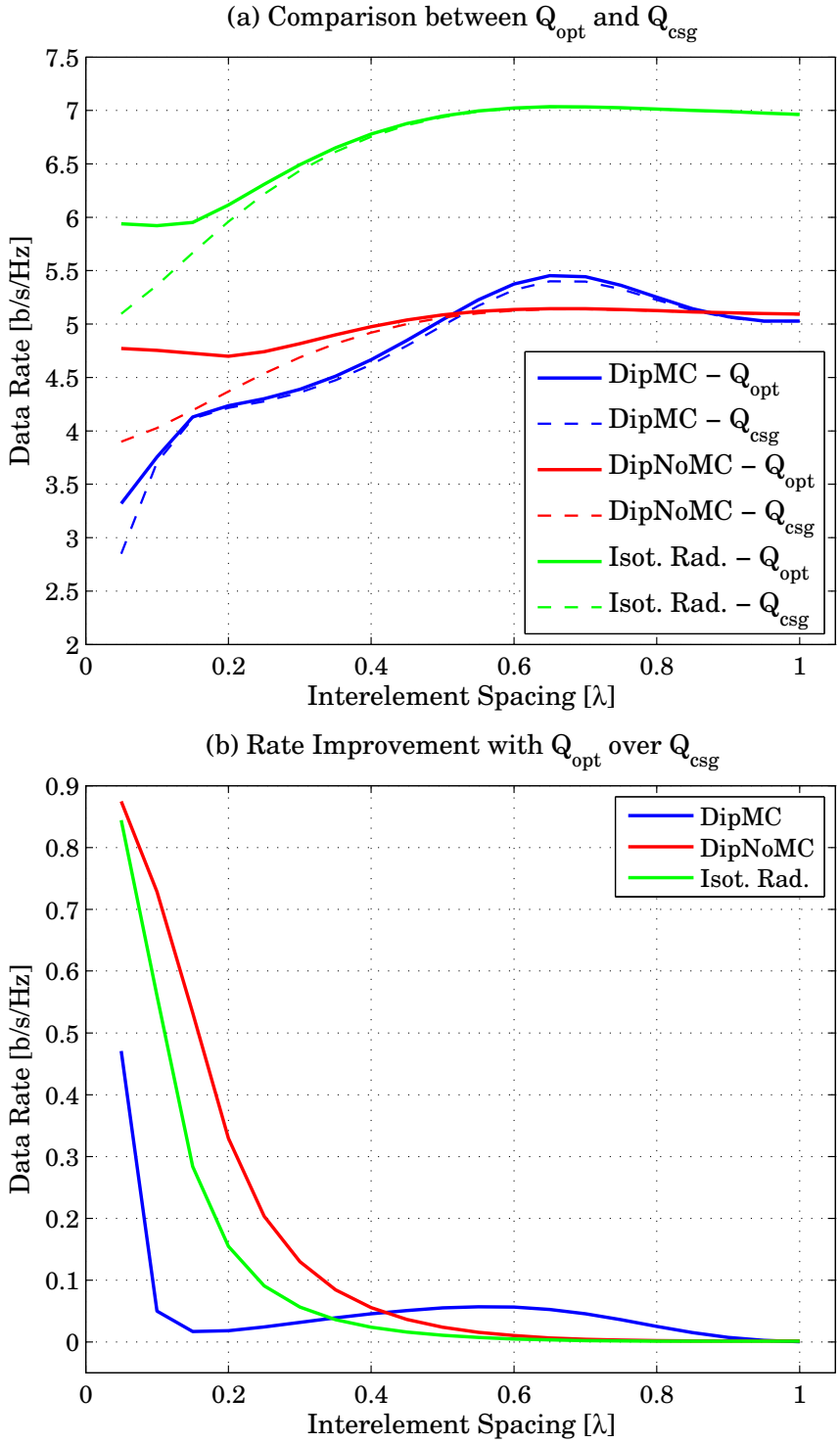

Figure 6.10: (a) Data rate curves obtained via $\mathbf{Q}_{opt}$ and $\mathbf{Q}_{csg}$. (b) Rate improvement with $\mathbf{Q}_{opt}$ over $\mathbf{Q}_{csg}$. $\rho_T = 27$dB.

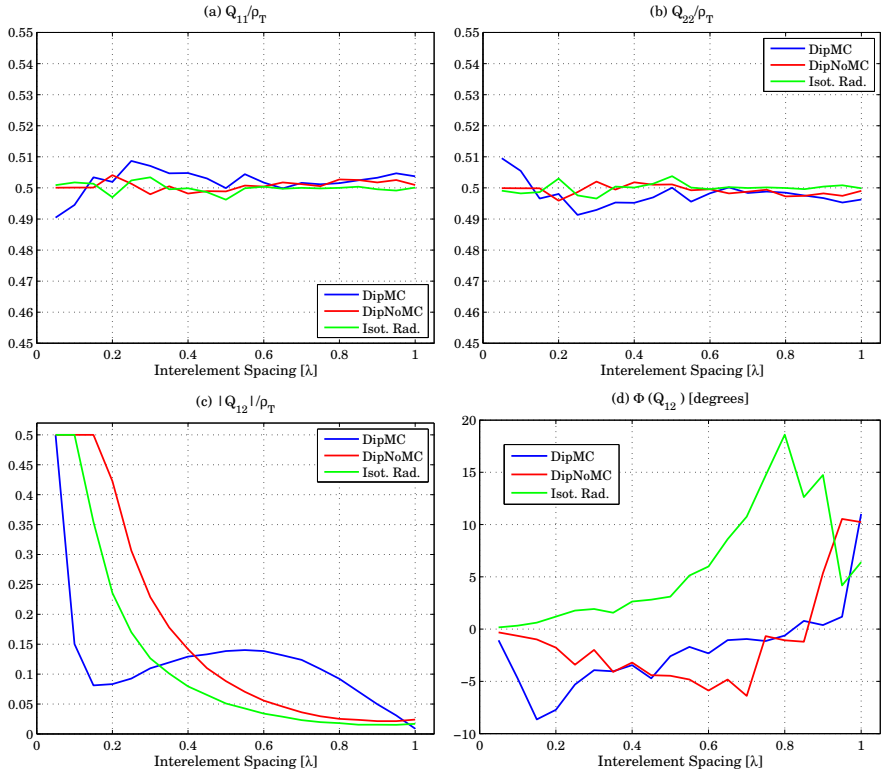

Figure 6.11: Optimal input covariance matrix entries. (a) Q_{11}/ρ_T. (b) Q_{22}/ρ_T. (c) Magnitude of Q_{12}/ρ_T. (d) Phase of Q_{12}. $\rho_T = 27$dB.

scheme results in significant improvement only for small antenna spacing values. Otherwise, the use of the diagonal input covariance is suitable.

6.5 Conclusions

In this work, the optimal input covariance matrices for three different types of transmitter arrays −of isotropic radiators, uncoupled dipoles and coupled ones− are obtained numerically using the particle swarm optimization technique in conjunction with a double directional multipath scenario for a 2×2 MIMO system.

It is observed that, moderate data rate improvement is possible for small antenna spacing values where the correlation is relatively high, mainly utilizing

nearly full or full covariance matrices. Otherwise, the selection of the diagonal covariance matrix is almost the optimal solution.

The numerical technique utilized here may help in finding the optimal transmission schemes for

- real life measurement campaigns and/or different channel models,
- different multipath scenarios; AoA, AoD, delay distributions;
- different array types (e.g., printed dipole/patch antennas);
- different/random array orientations.

Chapter 7

Conclusions

In this thesis, the MIMO channel is investigated from an electromagnetics perspective. The antenna dependency of the wireless channel is clearly shown. A full-wave channel model (MEF) based on the method of moments solution of the electric field integral equation is developed and used in order to evaluate the MIMO channel matrix accurately. MEF calculates the exact fields via the radiation integrals, and hence, it is rigorous except the scatterer scenario. The accuracy of the model is further verified by the measurement results. Thus, it is concluded that MEF achieves the accuracy over other approaches which are incapable of analyzing antenna effects in detail.

Making use of the presented technique MIMO performance of printed dipole arrays is analyzed. The capacity comparisons of printed dipole arrays with free-standing (FS) ones are given. It is observed that, printed dipoles are less sensitive to the mutual coupling than FS ones in terms of MIMO capacity. Furthermore, coupling between printed dipoles through surface waves is shown to have no significant effect on the channel capacity.

Effects of the electrical properties of printed dipoles on the MIMO capacity are explored in terms of the relative permittivity and thickness of the dielectric material. Appropriate dielectric slab configurations yielding high capacity printed dipole arrays are presented.

It should be mentioned that, efficiency of the proposed MEF algorithm is governed by the evaluation of the interactions, in particular in the case of printed arrays, and the inversion time of the MoM impedance matrix. However, considering the fact that typical MIMO systems do not contain thousands of antennas at the transmitter and receiver sides, inversion time of the MoM matrix is fast and the efficiency of MEF strongly depends on the calculation of self and mutual interactions (especially the case for printed arrays). Because we use different Green's function representations for printed arrays in the MoM procedure in a computationally optimized manner (based on the distance between antenna elements), the proposed MEF yields accurate results within seconds.

The numerical efficiency of the technique allows analyzing MIMO performance of arrays with large number of antennas, and high performance array design in conjunction with well-known optimization tools. Thus, MEF is combined with particle swarm optimization to design MIMO arrays of dipole elements for superior capacity. Validation of both the channel model and PSO is done by comparing the results with measurements and GA simulations. Freestanding and printed dipole arrays are analyzed and optimized.

FS dipole arrays are designed for high MIMO performance by optimizing the number of antenna elements, their individual locations and lengths, in a physically limited volume. It is shown that, the use of uniform circular arrays (UCA) is a reasonable choice for high capacity, even though results for other array configurations outperforming UCA are given as well.

The adaptive performance of printed dipole arrays in the MIMO channel is investigated by altering the termination impedances of the array elements using microelectromechanical switches. Adaptive printed dipoles are shown to be good alternatives to FS ones, due to less mutual coupling; though their reduced radiated power under fixed transmit SNR leads to slightly decreased MIMO capacity.

MIMO performance of printed rectangular patch arrays is analyzed using a modified version of the full-wave channel model (MEF). Various array configurations are designed, manufactured, and their MIMO performance is measured in an indoor environment. The channel properties, such as the power delay profile, mean excess delay and delay spread, are obtained via measurements and compared with MEF results. Very good agreement is achieved between the measurements and simulations by MEF. Microstrip patch arrays are found to be very stable against mutual coupling in terms of MIMO capacity. Effects of the electrical properties of printed patches on the MIMO capacity are explored in terms of the relative permittivity and thickness of the dielectric material. It is concluded that, the thinner the substrate, the less the capacity.

The optimal input covariance matrices for three different types of transmitter arrays −of isotropic radiators, uncoupled dipoles and coupled ones− are obtained numerically using the particle swarm optimization technique in conjunction with MEF in a double directional multipath scenario for a 2×2 MIMO system.

It is observed that, moderate data rate improvement is possible for small antenna spacing values where the correlation is relatively high, mainly utilizing nearly full or full covariance matrices. Otherwise, the selection of the diagonal covariance is almost the optimal solution.

Bibliography

[1] I. E. Telatar, "Capacity of multi-antenna Gaussian channels," *European Transactions on Telecommunications*, vol. 10, pp. 585–595, Nov. 1999.

[2] G. J. Foschini and M. J. Gans, "On limits of wireless communications in a fading environment when using multiple antennas," *Wireless Personal Communications*, vol. 6, pp. 311–335, Mar. 1998.

[3] J. Luo, J. Zeidler, and S. McLaughlin, "Performance analysis of compact antenna arrays with MRC in correlated nakagami fading channels," *IEEE Transactions on Vehicular Technology*, vol. 50, no. 1, pp. 267–277, Jan 2001.

[4] T. Svantesson and A. Ranheim, "Mutual coupling effects on the capacity of multielement antenna systems," *Proc. 2001 IEEE International Conference on Acoustics, Speech, and Signal Processing, 2001 (ICASSP '01).*, vol. 4, pp. 2485–2488 vol.4, 2001.

[5] J. Wallace and M. Jensen, "The capacity of MIMO wireless systems with mutual coupling," *Proc. 2002 IEEE 56th Vehicular Technology Conference, 2002, VTC 2002-Fall*, vol. 2, pp. 696–700 vol.2, 2002.

[6] ——, "Mutual coupling in MIMO wireless systems: A rigorous network theory analysis," *IEEE Transactions on Wireless Communications*, vol. 3, no. 4, pp. 1317–1325, July 2004.

[7] C. Waldschmidt, S. Schulteis, and W. Wiesbeck, "Complete RF system model for analysis of compact MIMO arrays," *IEEE Transactions on Vehicular Technology*, vol. 53, no. 3, pp. 579–586, May 2004.

[8] A. Derneryd and G. Kristensson, "Signal correlation including antenna coupling," *Electronics Letters*, vol. 40, no. 3, pp. 157–159, 5 Feb. 2004.

[9] J. Andersen and B. Lau, "On closely coupled dipoles in a random field," *IEEE Antennas and Wireless Propagation Letters*, vol. 5, no. 1, pp. 73–75, Dec. 2006.

[10] K. Rosengren, J. Carlsson, and P.-S. Kildal, "Maximizing the effective diversity gain of two parallel dipoles by optimizing the source impedances," *Microwave and Optical Technology Letters*, vol. 48, no. 3, pp. 532–535, 2006.

[11] B. K. Lau, J. B. Andersen, G. Kristensson, and A. F. Molisch, "Impact of matching network on bandwidth of compact antenna arrays," *IEEE Transactions on Antennas and Propagation*, vol. 54, no. 11, pp. 3225–3238, Nov. 2006.

[12] J. Wallace and M. Jensen, "Termination-dependent diversity performance of coupled antennas: Network theory analysis," *IEEE Transactions on Antennas and Propagation*, vol. 52, no. 1, pp. 98–105, Jan. 2004.

[13] M. Morris and M. Jensen, "Network model for MIMO systems with coupled antennas and noisy amplifiers," *IEEE Transactions on Antennas and Propagation*, vol. 53, no. 1, pp. 545–552, Jan. 2005.

[14] ——, "Impact of receive amplifier signal coupling on MIMO system performance," *IEEE Transactions on Vehicular Technology*, vol. 54, no. 5, pp. 1678–1683, Sept. 2005.

[15] A. Forenza and J. Heath, R.W., "Benefit of pattern diversity via two-element array of circular patch antennas in indoor clustered MIMO channels," *IEEE Transactions on Communications*, vol. 54, no. 5, pp. 943–954, May 2006.

[16] K. Warnick and M. Jensen, "Optimal noise matching for mutually coupled arrays," *IEEE Transactions on Antennas and Propagation*, vol. 55, no. 6, pp. 1726–1731, June 2007.

[17] F. Li and Q. T. Zhang, "Transmission strategy for MIMO correlated Rayleigh fading channels with mutual coupling," *Proc. IEEE International Conference on Communications, 2007, ICC '07*, pp. 1030–1035, 24-28 June 2007.

[18] R. Janaswamy, "Effect of element mutual coupling on the capacity of fixed length linear arrays," *IEEE Antennas and Wireless Propagation Letters*, vol. 1, pp. 157–160, 2002.

[19] B. Clerckx, D. Vanhoenacker-Janvier, C. Oestges, and L. Vandendorpe, "Mutual coupling effects on the channel capacity and the space-time processing of MIMO communication systems," *Proc. IEEE International Conference on Communications, 2003, ICC '03*, vol. 4, pp. 2638–2642 vol.4, 11-15 May 2003.

[20] S. Durrani and M. Bialkowski, "Effect of mutual coupling on the interference rejection capabilities of linear and circular arrays in CDMA systems," *IEEE Transactions on Antennas and Propagation*, vol. 52, no. 4, pp. 1130–1134, April 2004.

[21] S. Krusevac, P. Rapajic, and R. Kennedy, "The method for MIMO channel capacity estimation in the presence of spatially correlated noise," *Proc. 2004 IEEE Eighth International Symposium on Spread Spectrum Techniques and Applications*, pp. 511–514, 30 Aug.-2 Sept. 2004.

[22] X. Li and Z.-P. Nie, "Mutual coupling effects on the performance of MIMO wireless channels," *IEEE Antennas and Wireless Propagation Letters*, vol. 3, pp. 344–347, 2004.

[23] H. Mbonjo, J. Hansen, and V. Hansen, "MIMO capacity and antenna array design," *Proc. IEEE Global Telecommunications Conference, 2004, GLOBECOM '04*, vol. 5, pp. 3155–3159 Vol.5, 29 Nov.-3 Dec. 2004.

[24] C. A. Tunc, D. Aktas, and A. Altintas, "On arrays of dipole antennas with mutual coupling in MIMO wireless channels," *Proc. The 15th IST Mobile & Wireless Communication Summit*, June 4-8, 2006.

[25] ——, "Performance analysis of uniform circular arrays with mutual coupling in MIMO channels," *Proc. 2006 IEEE International Symposium on Antennas and Propagation and USNC/URSI National Radio Science Meeting*, July 9-14, 2006.

[26] J. Yu and Y.-D. Yao, "Evaluation of reverse link performance of a CDMA system with imperfect beamforming," *Proc. 2004 IEEE 59th Vehicular Technology Conference, 2004, VTC 2004-Spring*, vol. 1, pp. 137–141 Vol.1, 17-19 May 2004.

[27] J. Yu, Y.-D. Yao, A. Molisch, and J. Zhang, "Performance evaluation of CDMA reverse links with imperfect beamforming in a multicell environment using a simplified beamforming model," *IEEE Transactions on Vehicular Technology*, vol. 55, no. 3, pp. 1019–1031, May 2006.

[28] S. Ganesan, R. Mesleh, H. Ho, C. W. Ahn, and S. Yun, "On the performance of spatial modulation OFDM," *Proc. Fortieth Asilomar Conference on Signals, Systems and Computers, 2006, ACSSC '06*, pp. 1825–1829, Oct.-Nov. 2006.

[29] B. Getu and R. Janaswamy, "The effect of mutual coupling on the capacity of the MIMO cube," *IEEE Antennas and Wireless Propagation Letters*, vol. 4, pp. 240–244, 2005.

[30] M. E. Bialkowski, P. Uthansakul, K. Bialkowski, and S. Durrani, "Investigating the performance of MIMO systems from an electromagnetic perspective," *Microwave and Optical Technology Letters*, vol. 48, no. 7, pp. 1233–1238, 2006.

[31] Z. Xu, S. Sfar, and R. Blum, "On the importance of modeling the mutual coupling for antenna selection for closely-spaced arrays," *Proc. 2006 40th Annual Conference on Information Sciences and Systems*, pp. 1351–1355, 22-24 March 2006.

[32] B. Clerckx, C. Craeye, D. Vanhoenacker-Janvier, and C. Oestges, "Impact of antenna coupling on 2 × 2 MIMO communications," *IEEE Transactions on Vehicular Technology*, vol. 56, no. 3, pp. 1009–1018, May 2007.

[33] N. Maleki, E. Karami, and M. Shiva, "Optimization of antenna array structures in mobile handsets," *IEEE Transactions on Vehicular Technology*, vol. 54, no. 4, pp. 1346–1351, July 2005.

[34] ——, "Effects of mutual coupling on the diversity order of EGT systems," *Proc. 41st Annual Conference on Information Sciences and Systems, 2007, CISS '07*, pp. 505–510, 14-16 March 2007.

[35] M. Hefnawi, J. Gai, and R. A. Elasoued, "Mutual coupling effects on MIMO-adaptive beamforming systems," in *Proc. the Third International Conference on Networking and Services*, 2007, p. 106.

[36] Z. Huang, C. A. Balanis, and C. R. Birtcher, "Mutual coupling compensation in UCAs: Simulations and experiment," *IEEE Transactions on Antennas and Propagation*, vol. 54, no. 11, pp. 3082–3086, Nov. 2006.

[37] A. Wyglinski and S. Blostein, "On uplink CDMA cell capacity: mutual coupling and scattering effects on beamforming," *IEEE Transactions on Vehicular Technology*, vol. 52, no. 2, pp. 289–304, March 2003.

[38] V. Jungnickel, V. Pohl, and C. von Helmolt, "Capacity of MIMO systems with closely spaced antennas," *IEEE Communications Letters*, vol. 7, no. 8, pp. 361–363, Aug. 2003.

[39] M. Karaboikis, C. Soras, G. Tsachtsiris, and V. Makios, "Compact dual-printed inverted-f antenna diversity systems for portable wireless devices," *IEEE Antennas and Wireless Propagation Letters*, vol. 3, pp. 9–14, 2004.

[40] M. Ozdemir, H. Arslan, and E. Arvas, "On the correlation analysis of antennas in adaptive MIMO systems with 3-d multipath scattering," *Proc. IEEE Wireless Communications and Networking Conference, WCNC 2004*, vol. 1, pp. 295–299 Vol.1, 21-25 March 2004.

[41] S. Hwang, A. Medouri, and T. Sarkar, "Signal enhancement in a near-field MIMO environment through adaptivity on transmit," *IEEE Transactions on Antennas and Propagation*, vol. 53, no. 2, pp. 685–693, Feb. 2005.

[42] N. Kirsch and K. Dandekar, "Modeling effects of mutual coupling considered at both ends of a MIMO channel using computational electromagnetics," *Proc. 2004 IEEE 60th Vehicular Technology Conference, VTC2004-Fall*, vol. 6, pp. 4352–4355 Vol. 6, 26-29 Sept. 2004.

[43] K. Rosengren and P.-S. Kildal, "Radiation efficiency, correlation, diversity gain and capacity of a six-monopole antenna array for a MIMO system: theory, simulation and measurement in reverberation chamber," *IEE Proceedings - Microwaves, Antennas and Propagation*, vol. 152, no. 1, pp. 7–16, 19 Feb. 2005.

[44] M. Morris, M. Jensen, and J. Wallace, "Superdirectivity in MIMO systems," *IEEE Transactions on Antennas and Propagation*, vol. 53, no. 9, pp. 2850–2857, Sept. 2005.

[45] N. Bikhazi and M. Jensen, "The relationship between antenna loss and superdirectivity in MIMO systems," *IEEE Transactions on Wireless Communications*, vol. 6, no. 5, pp. 1796–1802, May 2007.

[46] I. Salonen, C. Icheln, and P. Vainikainen, "The dependency of pattern correlation on mutual coupling and losses in antenna arrays," *Microwave and Optical Technology Letters*, vol. 47, no. 2, pp. 145–147, 2005.

[47] O. Klemp and H. Eul, "Analytical approach for MIMO performance and electromagnetic coupling in linear dipole arrays," *Proc. The 2nd International Symposium on Wireless Communication Systems, 2005*, pp. 586–590, 5-7 Sept. 2005.

[48] J. Thaysen and K. B. Jakobsen, "Design considerations for low antenna correlation and mutual coupling reduction in multi antenna terminals," *European Transactions on Telecommunications*, vol. 18, no. 3, pp. 319–326, 2007.

[49] D. W. Browne, M. Manteghi, M. P. Fitz, and Y. Rahmat-Samii, "Experiments with compact antenna arrays for MIMO radio communications," *IEEE Transactions on Antennas and Propagation*, vol. 54, no. 11, pp. 3239–3250, Nov. 2006.

[50] C. A. Tunc, E. Irci, O. Bakir, D. Aktas, V. B. Erturk, and A. Altintas, "Investigation of Planar and Conformal Printed Arrays for MIMO Performance Analysis," *Proc. The European Conference on Antennas and Propagation: EuCAP 2006*, Nov. 2006.

[51] ——, "A model with electric fields for the inclusion of mutual coupling effects in the MIMO channel," *Proc. 2007 IEEE Antennas and Propagation International Symposium*, pp. 2977–2980, 9-15 June 2007.

[52] U. Olgun, C. A. Tunc, D. Aktas, V. B. Erturk, and A. Altintas, "Optimization of linear wire antenna arrays to increase MIMO capacity using

swarm intelligence," *Proc. The Second European Conference on Antennas and Propagation, EuCAP 2007*, pp. 1–6, 11-16 Nov. 2007.

[53] H. Rogier, "Mutual coupling compensation in uniform circular arrays with center element using a coupling matrix based on phase modes," *Proc. 2006 IEEE Antennas and Propagation Society International Symposium*, pp. 1133–1136, 9-14 July 2006.

[54] A. Diallo, C. Luxey, P. Le Thuc, R. Staraj, and G. Kossiavas, "Study and reduction of the mutual coupling between two mobile phone PIFAs operating in the DCS1800 and UMTS bands," *IEEE Transactions on Antennas and Propagation*, vol. 54, no. 11, pp. 3063–3074, Nov. 2006.

[55] M. Bialkowski, P. Uthansakul, and K. Bialkowski, "Investigations into the effect of los signal blocking on capacity of an indoor MIMO system," *Proc. International Conference on Microwaves, Radar & Wireless Communications, 2006*, pp. 406–409, 22-24 May 2006.

[56] M. Jensen and J. Wallace, "Capacity of the continuous-space electromagnetic channel," *IEEE Transactions on Antennas and Propagation*, vol. 56, no. 2, pp. 524–531, Feb. 2008.

[57] C.-C. Lin, L.-C. Kuo, and H.-R. Chuang, "A horizontally polarized omnidirectional printed antenna for WLAN applications," *IEEE Transactions on Antennas and Propagation*, vol. 54, no. 11, pp. 3551–3556, Nov. 2006.

[58] J. Guterman, A. Moreira, and C. Peixeiro, "Integration of omnidirectional wrapped microstrip antennas into laptops," *IEEE Antennas and Wireless Propagation Letters*, vol. 5, no. 1, pp. 141–144, Dec. 2006.

[59] D. Piazza and K. Dandekar, "Reconfigurable antenna solution for MIMO-OFDM systems," *Electronics Letters*, vol. 42, no. 8, pp. 446–447, 13 April 2006.

[60] A. Sayeed and V. Raghavan, "Maximizing MIMO capacity in sparse multipath with reconfigurable antenna arrays," *IEEE Journal of Selected Topics in Signal Processing*, vol. 1, no. 1, pp. 156–166, June 2007.

[61] K. Boyle and P. Steeneken, "A five-band reconfigurable PIFA for mobile phones," *IEEE Transactions on Antennas and Propagation*, vol. 55, no. 11, pp. 3300–3309, Nov. 2007.

[62] J. Boerman and J. Bernhard, "Performance study of pattern reconfigurable antennas in MIMO communication systems," *IEEE Transactions on Antennas and Propagation*, vol. 56, no. 1, pp. 231–236, Jan. 2008.

[63] B. Poussot, J.-M. Laheurte, L. Cirio, O. Picon, D. Delcroix, and L. Dussopt, "Diversity measurements of a reconfigurable antenna with switched polarizations and patterns," *IEEE Transactions on Antennas and Propagation*, vol. 56, no. 1, pp. 31–38, Jan. 2008.

[64] D. Piazza, N. J. Kirsch, A. Forenza, R. W. Heath, and K. R. Dandekar, "Design and evaluation of a reconfigurable antenna array for MIMO systems," *IEEE Transactions on Antennas and Propagation*, vol. 56, no. 3, pp. 869–881, March 2008.

[65] H. Carrasco, R. Feick, and H. D. Hristov, "Experimental evaluation of indoor MIMO channel capacity for compact arrays of planar inverted-f antennas," *Microwave and Optical Technology Letters*, vol. 49, no. 7, pp. 1754–1756, 2007.

[66] Y. Gao, X. Chen, Z. Ying, and C. Parini, "Design and performance investigation of a dual-element PIFA array at 2.5 GHz for MIMO terminal," *IEEE Transactions on Antennas and Propagation*, vol. 55, no. 12, pp. 3433–3441, Dec. 2007.

[67] B. Lindmark and L. Garcia-Garcia, "Compact antenna array for MIMO applications at 1800 and 2450 MHz," *Microwave and Optical Technology Letters*, vol. 48, no. 10, pp. 2034–2037, 2006.

[68] M. Manteghi and Y. Rahmat-Samii, "A novel miniaturized triband PIFA for MIMO applications," *Microwave and Optical Technology Letters*, vol. 49, no. 3, pp. 724–731, 2007.

[69] A. Konanur, K. Gosalia, S. Krishnamurthy, B. Hughes, and G. Lazzi, "Increasing wireless channel capacity through MIMO systems employing co-located antennas," *IEEE Transactions on Microwave Theory and Techniques*, vol. 53, no. 6, pp. 1837–1844, June 2005.

[70] A. Rajagopalan, G. Gupta, A. Konanur, B. Hughes, and G. Lazzi, "Increasing channel capacity of an ultrawideband MIMO system using vector antennas," *IEEE Transactions on Antennas and Propagation*, vol. 55, no. 10, pp. 2880–2887, Oct. 2007.

[71] R. Ramirez and F. De Flaviis, "A mutual coupling study of linear and circular polarized microstrip antennas for diversity wireless systems," *IEEE Transactions on Antennas and Propagation*, vol. 51, no. 2, pp. 238–248, Feb 2003.

[72] M. D. Migliore, D. Pinchera, and F. Schettino, "Improving channel capacity using adaptive MIMO antennas," *IEEE Transactions on Antennas and Propagation*, vol. 54, no. 11, pp. 3481–3489, Nov. 2006.

[73] A. Mukherjee and H. Kwon, "Compact multi-user wideband MIMO system using multiple-mode microstrip antennas," *Proc. IEEE 65th Vehicular Technology Conference, 2007, VTC2007-Spring*, pp. 584–588, 22-25 April 2007.

[74] W.-S. Chen, Y.-C. Chang, H.-T. Chen, F.-S. Chang, and H.-C. Su, "Novel design of printed monopole antenna for WLAN/WiMAX applications,"

Proc. 2007 IEEE Antennas and Propagation International Symposium, pp. 3281–3284, 9-15 June 2007.

[75] E. Avila-Navarro, J. A. Carrasco, and C. Reig, "Design of Yagi-like printed antennas for WLAN applications," *Microwave and Optical Technology Letters*, vol. 49, no. 9, pp. 2174–2178, 2007.

[76] K.-L. Wong, C.-H. Chang, and Y.-C. Lin, "Printed PIFA EM compatible with nearby conducting elements," *IEEE Transactions on Antennas and Propagation*, vol. 55, no. 10, pp. 2919–2922, Oct. 2007.

[77] D. Landon and C. Furse, "Recovering handset diversity and MIMO capacity with polarization-agile antennas," *IEEE Transactions on Antennas and Propagation*, vol. 55, no. 11, pp. 3333–3340, Nov. 2007.

[78] D. Pinchera, J. W. Wallace, M. D. Migliore, and M. A. Jensen, "Experimental analysis of a wideband adaptive-MIMO antenna," *IEEE Transactions on Antennas and Propagation*, vol. 56, no. 3, pp. 908–913, March 2008.

[79] C. A. Balanis, *Antenna Theory: Analysis and Design*, 3rd ed. John Wiley & Sons, 2005.

[80] H. King, "Mutual impedance of unequal length antennas in echelon," *IRE Transactions on Antennas and Propagation*, vol. 5, no. 3, pp. 306–313, July 1957.

[81] J. Robinson and Y. Rahmat-Samii, "Particle swarm optimization in electromagnetics," *IEEE Transactions on Antennas and Propagation*, vol. 52, no. 2, pp. 397–407, Feb. 2004.

[82] D. Pozar, "Analysis of finite phased arrays of printed dipoles," *IEEE Transactions on Antennas and Propagation*, vol. 33, no. 10, pp. 1045–1053, Oct 1985.

[83] ——, "Input impedance and mutual coupling of rectangular microstrip antennas," *IEEE Transactions on Antennas and Propagation*, vol. 30, no. 6, pp. 1191–1196, Nov 1982.

[84] O. Bakir, "Investigation of finite phased arrays of printed antennas on planar and cylindrical grounded dielectric slabs," Master's thesis, Bilkent University, Ankara, Turkey, 2006. [Online]. Available: http://www.thesis.bilkent.edu.tr/0003095.pdf

[85] O. Bakir, O. Civi, V. Erturk, and H.-T. Chou, "Efficient analysis of phased arrays of microstrip patches using a hybrid generalized forward backward method/Green's function technique with a DFT based acceleration algorithm," *IEEE Transactions on Antennas and Propagation*, vol. 56, no. 6, pp. 1669–1678, June 2008.

[86] M. Marin, S. Barkeshli, and P. Pathak, "Efficient analysis of planar microstrip geometries using a closed-form asymptotic representation of the grounded dielectric slab Green's function," *IEEE Transactions on Microwave Theory and Techniques*, vol. 37, no. 4, pp. 669–679, Apr 1989.

[87] H. Nakano, K. Hirose, T. Suzuki, S. Kerner, and N. Alexopoulos, "Numerical analyses of printed line antennas," *IEE Proceedings H Microwaves, Antennas and Propagation*, vol. 136, no. 2, pp. 98–104, Apr 1989.

[88] P. Katehi and N. Alexopoulos, "On the effect of substrate thickness and permittivity on printed circuit dipole properties," *Proc. IEEE Antennas and Propagation Society International Symposium, 1982*, vol. 20, pp. 70–73, May 1982.

[89] S. Xu and Y. Rahmat-Samii, "Boundary conditions in particle swarm optimization revisited," *IEEE Transactions on Antennas and Propagation*, vol. 55, no. 3, pp. 760–765, March 2007.

[90] A. Street, L. Lukama, and D. Edwards, "Use of VNAs for wideband propagation measurements," *IEE Proceedings-Communications*, vol. 148, no. 6, pp. 411–415, Dec 2001.

[91] F. Abboud, J. Damiano, and A. Papiernik, "Simple model for the input impedance of coax-fed rectangular microstrip patch antenna for CAD," *IEE Proceedings H Microwaves, Antennas and Propagation*, vol. 135, no. 5, pp. 323–326, Oct 1988.

[92] *www.ansoft.com/hfworkshop02/Ensemble_Essentials.pdf*. Ansoft Ensemble, 2002.

[93] R. Vaughan and J. B. Andersen, *Channels, Propagation and Antennas for Mobile Communications*. The IEE Press, 2003.

[94] T. S. Rappaport, *Wireless Communications: Principles & Practice*. Prentice Hall, 1996.

[95] W. C. Chew, *Waves And Fields In Inhomogeneous Media*. IEEE Press, 1995.

[96] Y. T. Lo and S. W. Lee, *Antenna Handbook: Theory, Applications, and Design*. Springer, 1988.

[97] C. Shannon, "Communication in the presence of noise," *Proceedings of the IRE*, vol. 37, no. 1, pp. 10–21, Jan. 1949.

[98] B. Clerckx, C. Craeye, D. Vanhoenacker-Janvier, and C. Oestges, "Impact of antenna coupling on 2×2 MIMO communications," *IEEE Transactions on Vehicular Technology*, vol. 56, no. 3, pp. 1009–1018, May 2007.